J. Mech. Phys. Solids 201 (2025) 106157

Contents lists available at ScienceDirect

Journal of the Mechanics and Physics of Solids

journal homepage: www.elsevier.com/locate/jmps

Thermal fluctuations effects on crack nucleation and propagation

Claudia Binetti [a,b], Giuseppe Florio [b,c], Nicola M. Pugno [d,e,*], Stefano Giordano [a,*], Giuseppe Puglisi [b,*]

[a] University of Lille, CNRS, Centrale Lille, Univ. Polytechnique Hauts-de-France, UMR 8520 - IEMN - Institut d'Électronique, de Microélectronique et de Nanotechnologie, Lille, F-59000, France
[b] Department of Civil Environmental Land Building Engineering and Chemistry, DICATECh, Politecnico di Bari, Via Orabona 4, Bari, 70125, Italy
[c] INFN, Section of Bari, I-70126, Italy
[d] Laboratory for Bioinspired, Bionic, Nano, Meta Materials & Mechanics, University of Trento, Via Mesiano 77, Trento, 38123, Italy
[e] School of Engineering and Materials Science, Queen Mary University of London, Mile End Road, London, E1, UK

ARTICLE INFO

Keywords:
Fracture mechanics
Griffith's criterion
Temperature effects
Statistical mechanics
Phase transitions
Spin variables approach

ABSTRACT

This paper investigates the impact of thermal effects on fracture propagation, a subject that poses significant theoretical and experimental challenges across multiple scales. While previous experimental and numerical studies have explored the relationship between temperature fluctuations and mechanical behavior, a comprehensive theoretical framework in fracture mechanics that rigorously incorporates temperature effects is still absent. Building upon the Griffith energetic approach and equilibrium statistical mechanics, we incorporate entropic effects into the overall energy balance of the system and replace the total mechanical energy with free energies. Indeed, our model captures the energetic interplay between elastic deformation, external loads, fracture energy, and entropic contributions. We propose a simplified approach in which both discrete and continuum representations are formulated concurrently, reflecting a multiscale paradigm. The discrete model leverages statistical mechanics to account for temperature effects, while the continuum model provides a mesoscopic description of the fracture process. This framework provides (temperature dependent) analytical expressions for key mechanical parameters, such as the stress and displacement fracture thresholds, the energy release rate, the fracture surface energy, and the J-integral. Notably, we identify a critical temperature at which the system undergoes a phase transition from an intact to a fractured state in the absence of mechanical loading. We believe that this approach lays the foundation for a new theoretical framework, enabling a rigorous multiscale understanding of thermal fluctuations in fracture mechanics. We finally propose a comparison with numerical data concerning the fracture of graphene as a function of temperature exhibiting the efficiency of the model in describing thermal effects in fracture behavior.

1. Introduction

The study of thermal effects on fracture propagation is a highly engaging yet complex field of research. It is engaging because it presents theoretical and experimental challenges that span multiple scales, from molecular architecture to macroscopic nonlinear behavior and the history of fracture mechanics reveals the involvement of numerous intricate physical phenomena. The importance

* Corresponding authors.
E-mail addresses: nicola.pugno@unitn.it (N.M. Pugno), stefano.giordano@univ-lille.fr (S. Giordano), giuseppe.puglisi@poliba.it (G. Puglisi).

https://doi.org/10.1016/j.jmps.2025.106157
Received 6 November 2024; Received in revised form 4 March 2025; Accepted 14 April 2025
Available online 30 April 2025

Nomenclature

n	Number of total units	Ω	Prescribed overall extension
m	Number of broken units	$\tilde{\Omega}$	Non-dim. prescribed overall extension
ξ	Broken fraction of the system m/n	$\tilde{\Omega}_{cr}$	Griffith-Helmholtz critical extension
ζ	Crack extension ξL	U_i	Potential energy breakable springs
a	Fractured area	V_i	Potential energy shear springs
L	Total system length	T_i	Potential energy device springs
h	Equilibrium system height	g	Mechanical energy (Gibbs ensemble)
b	System depth	$\tilde{g}$	Non-dimensional Gibbs energy
Y_M	Displacement threshold	$\tilde{g}_e$	Equilibrium non-dimensional Gibbs energy
x	Abscissa		
$\tilde{x}$	Non-dimensional abscissa x/L	$\mathcal{G}$	Gibbs free energy $H - TS$
ϵ	Extensional strain	$\tilde{\mathcal{G}}$	Non-dimensional Gibbs free energy
ϵ_d	Extensional device strain	ϕ	Mechanical energy (Helmholtz ensemble)
γ	Shear strain		
k_t	Elastic constant breakable springs	$\tilde{\phi}$	Non-dimensional Helmholtz energy
k_e	Elastic constant shear springs	$\tilde{\phi}_e$	Equilibrium non-dim. Helmholtz energy
k_d	Elastic constant device springs	$\mathcal{F}$	Helmholtz free energy $U - TS$
v_i	Displacements	$\tilde{\mathcal{F}}$	Non-dimensional Helmholtz free energy
$\tilde{v}_i$	Non-dimensional displacements	Π	Total potential energy
$\tilde{\boldsymbol{v}}$	Non-dimensional displacement vector	$\tilde{\Pi}$	Non-dimensional potential energy
$\tilde{\boldsymbol{v}}_e^{\mathcal{G}}$	Equilibrium non-dim. Gibbs displ. vector	π	Potential energy density
		Γ	Fracture energy
$\tilde{\boldsymbol{v}}_e^{\mathcal{H}}$	Equilibrium non-dim. Helmholtz displ. vector	$\tilde{\Gamma}$	Non-dimensional fracture energy
		γ_s	Fracture energy per unit surface
$\tilde{v}_{av}^{\mathcal{G}}$	Average Gibbs displacement vector	G	Energy release rate
$\tilde{v}_{av}^{\mathcal{H}}$	Average Helmholtz displacement vector	G_c	Critical energy release rate
E	Young modulus	$\tilde{G}$	Non-dimensional energy release rate
E_d	Device Young modulus	K	Stress intensity factor
μ	Shear modulus	κ	Gibbs Lagrangian density
ν^2	Elastic ratio $\mu h^2/(EL^2)$	ς	Helmholtz Lagrangian density
ρ^2	Stiffness ratio $hE_d/(dE)$	T	Temperature
χ_i	Spin variable	$T_c^{\mathcal{G}}$	Gibbs critical temperature
$\boldsymbol{\chi}$	Spin variable vector	$T_c^{\mathcal{H}}$	Helmholtz critical temperature
$\boldsymbol{B}$	Tridiagonal Gibbs matrix	$T_{c,\delta}^{\mathcal{H}}$	Helmholtz critical temperature ($\delta \neq 0$)
$\boldsymbol{Q}$	Tridiagonal Helmholtz matrix	k_B	Boltzmann constant
$\mathbf{1}$	Vectors with n ones	$\tilde{\beta}$	Non-dimensional thermodynamic beta $\frac{ELbY_M^2}{hk_BT}$
f	Force on each unit		
F_t	Total force nf	$\tilde{\beta}_c^{\mathcal{G}}$	Gibbs critical beta
F	Configurational force	$\tilde{\beta}_c^{\mathcal{H}}$	Helmholtz critical beta
S_f	Shear force	U	Internal energy
σ	Applied tensile stress	H	Enthalpy
λ	Non-dimensional applied tensile stress	S	Entropy
$\lambda_{cr}^{\mathcal{G}}$	Griffith–Gibbs critical load	$\mathcal{Z}^{\mathcal{G}}$	Gibbs partition function
$\lambda_{cr}^{\mathcal{H}}$	Griffith–Helmholtz critical load	$\mathcal{Z}^{\mathcal{H}}$	Helmholtz partition function

of this topic is underscored by its relevance across various domains, ranging from classical mechanical sciences to emerging fields such as advanced materials (Low and Mai, 1989; Miracle and Senkov, 2017; Gali and George, 2013; Rabbi and Chalivendra, 2021), nanotechnology (Mastrangelo, 1997; Kang and Cai, 2010; Wang et al., 2007; Wu et al., 2012), and biological systems (Yan et al., 2007; Creton and Ciccotti, 2016).

Numerous experimental studies (Slootman et al., 2022; Gent and Petrich, 1969; Slootman et al., 2020) and numerical simulations (Zhao and Aluru, 2010; Pereira Junior et al., 2020; Blumberg Selinger et al., 1991) have explored the interplay between thermal fluctuations and mechanical properties, demonstrating that thermal effects play a critical role in fracture processes,

particularly in nanoscale systems and soft materials with significant entropic contributions, such as rubber-like materials and biomaterials (De Tommasi et al., 2013; Manca et al., 2013; Prados et al., 2013; Bonilla et al., 2015; Dudko, 2016; Buche and Silberstein, 2020; Bleha and Cifra, 2022). However, despite the extensive research in this area, no rigorous theoretical approach in fracture mechanics currently integrates temperature effects from the first principles of statistical mechanics. Classical models in Linear Elastic Fracture Mechanics (LEFM), still prevalent in both theoretical and numerical studies, primarily address the mechanical properties of materials. Thermal effects are typically considered only in a phenomenological manner and are not systematically incorporated.

One of the most influential contributions in fracture mechanics is the work of Griffith (1921), which laid the foundation of LEFM by introducing an energy-based approach into fracture studies. Before Griffith's theory, material failure was generally considered to occur when the maximum stress or strain exceeded a critical value. Researchers had already recognized that material failure was associated with the presence of cracks and flaws, which lead to localized stress and strain intensification. This insight motivated several studies on stress fields in materials with cracks of various sizes and shapes, such as those involving circular (Kirsch, 1898) or elliptical holes (Inglis, 1913). However, failure criteria based solely on stress concentration were found to be inconsistent with experimental observations.

Griffith addressed this issue by developing a model based on energy balance. His key innovation was to consider not only the elastic strain energy but also the energy required to create new fracture surfaces. Using this approach, Griffith derived an expression for the stress required to fracture a material with a pre-existing crack. His analysis began with an infinite plane subjected to tensile loading and containing an elliptical crack, which he then simplified to a slit crack based on Inglis (1913) results. While this model has been validated by numerous experiments (Lawn, 1993; Öchsner, 2016), it has a significant limitation: as the crack length approaches zero, the predicted stress required for fracture becomes infinite, making it unsuitable for predicting crack nucleation.

Although Griffith's theory correctly predicts the relationship between flaw size and fracture strength in brittle materials, it fails to account for plastic deformation, which is crucial for ductile materials such as metals. Extensions to the Griffith model by Irwin (1948) and Orowan (1948) incorporated plastic phenomena, leading to models that can describe ductile fracture behavior. Moving beyond the LEFM theory, Irwin (1961) included a new term into the energy balance, accounting for the plastic zone correction. This idea paved the way for the development of cohesive fracture models. Unlike Griffith's approach in which the fracture energy density is a constant, in cohesive models the fracture energy density is assigned as a continuous function of the crack opening. Interestingly, cohesive models avoid the nonphysical stress singularity at the crack tip, a typical drawback of LEFM models. An approach that yields similar results but based on different concepts was previously developed by Elliott (1947). His idea was to examine matter from an atomic perspective, extending Griffith's criterion with interatomic forces that prevent the crack opening. In this case, crack propagation occurs when interatomic bonds break, that is when adjacent atoms are pulled apart, exceeding a critical distance.

On this basis, Barenblatt (1959, 1962) developed his model by considering the forces that prevent the crack from opening, applied between the opposite sides of the fracture. To implement this concept, he introduced a "modulus of cohesion", the continuous counterpart of the atomic interaction force of Elliott (1947), characterizing each material. Successively, this model became known as the "cohesive zone model", and several researchers followed this paradigm. For instance, Dugdale (1960) employed a cohesive model to investigate yielding at the crack tip and the size of the plastic zone. It can be shown that cohesive and Griffith models are in agreement when the cohesive zone is much smaller than the crack size (Willis, 1967; Marigo and Truskinovsky, 2004). The theory of the cohesive zone has been further extended to different geometries and physical responses (Wells, 1961; Hillerborg et al., 1976; Hui et al., 2011; Kramer, 2005; Tijssens et al., 2000; Estevez et al., 2000; Del Piero and Truskinovsky, 2001).

Later, Rice (1968) introduced the J-integral, characterizing the material behavior ahead of a crack, and generalizing the energy release rate to nonlinear materials. The effectiveness of this approach has been proved by Shih and Hutchinson (1976), who defined an explicit relationship between the J-integral, the stress and the defect size. Alongside the J-integral, Wells (1961) introduced a parameter known as Crack Tip Opening Displacement (CTOD), which resulted in an alternative fracture criterion. This provided a new perspective in understanding fracture behavior in situations characterized by large plastic deformations anticipating material failure. Further developments are represented by the CTOD design curve (Burdekin and Dawes, 1971), and by the comparison between J-integral and CTOD methods (Shih, 1981).

While previous approaches are mostly based on the analysis of driving forces in continuum media with preassigned crack (they are not able to describe crack nucleation), a new recent paradigm has been developed through variational approaches for free discontinuities problems (Mumford and Shah, 1989; De Giorgi et al., 1989). Specifically, the variational models made it possible to predict crack nucleation, and to describe fracture propagation along a non-prescribed path (Francfort and Marigo, 1998). The fundamental idea behind this model is to determine the elastic fields of the fractured solids by minimizing the total energy (elastic and fracture contributions). The works of Bourdin et al. (2000) and Bourdin (2007) provided a numerical implementation of this complex mathematical theory useful to deal with realistic situations. Further investigations with several forms of cohesive energy have been performed using different variational techniques, in particular focusing on the important role of meta-stable solutions (Del Piero, 2013).

Homogenization methods have also been introduced for studying fracture in heterogeneous and microstructured systems, with both continuous and discrete models (Dormieux and Kondo, 2016; Sahimi, 2003a,b; Kachanov, 1992, 1993; Giordano and Colombo, 2007a,b, 2008; Markov and Kanaun, 2017; Markov et al., 2019).

A parallel line of research concerns numerical discrete approaches for understanding fracture phenomena at the molecular scale. The idea of considering fracture from a discrete perspective is credited to Novozhilov (1969a,b), and follows from the observation that crack propagation can be viewed as a discrete succession of atomic bond breaks (Marder, 1996). The same idea is behind molecular dynamics simulations, where Newton's law is numerically solved for an assembly of atoms described by a given interaction

potential energy. Thomson et al. (1971) applied this approach to fracture in order to calculate the force required to open a straight crack in a regular lattice. Other results were obtained by Sinclair and Lawn (1972) for diamond lattices, using complex angle-dependent potentials. Moreover, molecular dynamics simulations were essential in discovering the lattice trapping phenomenon, identifying a stress range where cracks neither propagate nor heal, as observed by Esterling and Swaroop (1979) and Paskin et al. (1981). The world of atomistic simulations for fracture mechanics is vast and full of important results, which we do not have the space here to discuss in detail (Gumbsch et al., 1997; Rountree et al., 2002; Bitzek et al., 2015; Frenkel and Smit, 2023). Recently, the Griffith criterion for brittle materials has been validated by atomistic simulations in ideal monocrystalline systems by Mattoni et al. (2005) and Giordano et al. (2010).

While molecular dynamics simulations represent a very accurate method for the description of fracture propagation, the so-called lattice models have been introduced to reduce the computational cost. Indeed, in this case each mass point only interacts with a predefined set of neighboring points, as opposed to molecular dynamics in which any atom can move and interact with any other atom. Moreover, unlike in molecular dynamics simulations, in lattice models rupture typically does not appear spontaneously, but must be introduced as an additional feature. Analytical solutions for the dynamic behavior of cracks in a one-dimensional lattice were first obtained by Slepyan (1981), with further extensions to the 2D case by Kulakhmetova et al. (1984), Ryvkin and Slepyan (2010), and Mishuris et al. (2009). Another approach that addresses fracture as a discrete process is the Quantized Fracture Mechanics by Pugno and Ruoff (2004). This method eliminates the stress singularity at the crack tip and derives a finite stress to break the material even in the absence of fractures, thus solving the main problems of LEFM.

Despite the substantial volume of research conducted on fracture phenomena, achieving a comprehensive and analytically rigorous approach to describe the effects of temperature on fracture propagation has proven elusive. Nevertheless, the examination of thermal effects holds crucial importance for several systems, including nano-materials, rubber-like and biological materials, bio-inspired materials, and innovative artificial materials designed to withstand high temperatures. Hence, the present work aims at exploring how temperature induced fluctuations affect failure through a new theoretical framework. One of the challenges in this analysis is to bridge the nano-scale with the meso-scale through a multiscale approach. Here, this paradigm is employed by concurrently introducing a discrete and a continuum model of the mode I fracture.

As we demonstrate, this approach ensures that both the local and global minimizers of the discrete model converge to the equilibria of the mesoscopic model in the continuum limit, thereby preserving all the essential physical information of the discrete lattice. The discrete model let us incorporate temperature effects through statistical mechanics, measuring fluctuations at molecular- or nano-scales, whereas the continuous model enables the description of elasticity and energy release rate at mesoscale. It is important to note that, while the considered model is quite simple, it allows us both to capture all main qualitative features of the fracture phenomenology and to integrate temperature effects. Moreover, all results are deduced in closed analytical form, allowing for deeper description of the fundamental underlying physical phenomena.

From a methodological point of view, we employ tools from equilibrium statistical mechanics (Gibbs, 1902; Weiner, 1983). This implies that the results are valid in a quasi-static regime, in which the system is able to re-equilibrate on timescales smaller than those of applied loading. It is noteworthy to underline that the phenomenon of fracture in solids has been previously analyzed through statistical approaches (Truskinovsky, 1996; Zapperi et al., 1997; Moreno et al., 2000; Alava et al., 2006; Kawamura et al., 2012; Cannizzo and Giordano, 2023; Buche and Grutzik, 2024). In particular, fracture phenomena in disorder materials have been largely investigated (Herrmann and Roux, 1990; Charmet et al., 1990; Ponson and Pindra, 2017; Parisi et al., 2017; Lebihain et al., 2021; Borja da Rocha and Truskinovsky, 2022). In addition, some works directly investigated thermal effects on fracture propagation (Peyrard and Bishop, 1989; Peyrard, 2004; Santucci et al., 2003; Guarino et al., 2006; Guarino and Ciliberto, 2011; Vincent-Dospital et al., 2020a,b, 2021). At the discrete level, we base our analysis on spin type models describing the debonding of links associated with fracture propagation. This type of approach has shown to be successful in the analysis of several instability, stick–slip, decohesion, and unzipping phenomena at the molecular scale for different biological and artificial systems (Caruel and Truskinovsky, 2016, 2018; Giordano, 2017; Benedito and Giordano, 2018a,b; Bellino et al., 2019; Florio and Puglisi, 2019; Florio et al., 2020; Cannizzo et al., 2021; Bellino et al., 2020; Cannizzo et al., 2022; Florio and Puglisi, 2023; Giordano, 2022, 2023). It has been recently extended also to the numerical analysis of two dimensional systems by Nitecki and Givli (2021) and Shuminov and Givli (2024). We remark that, as in classical statistical mechanics approaches, these models are typically based on a *global* minimization of the total energy. In our development, we extend the classical Griffith criterion for crack propagation, by replacing the total mechanical energies with Gibbs or Helmholtz free energies. This concept is consistent with the observation that fracture processes are typically irreversible and thus associated with entropy increase (Eftis and Liebowitz, 1976; Stevens and Guiu, 1991). Furthermore, out-of-equilibrium thermodynamics states that the evolution of a system, *e.g.* from an intact configuration to a broken one, results in the decrease of a suitable free energy (Blumberg Selinger et al., 1991). Hence, we analyze the *local* minima of the wiggly energy landscape, where the wells correspond to different fracture configurations, and, according with the Griffith approach, we assume that the fracture propagates when the total Helmholtz or Gibbs free energy decreases. The essential role of local energy minimizers, as opposed to the classical variational approaches for fracture that are based on global energy minimization, has been fully exploited by Del Piero (2013).

The approach that we here propose allows us to analytically obtain different results. From one side, we can predict a finite stress required for fracture propagation, even when the limit of zero-length crack is considered (crack nucleation). This is coherent with the experimental behavior. We recall that this possibility is attained by introducing discrete effects also in the so called Quantized Fracture Mechanics approach developed by Pugno and Ruoff (2004). In addition, our model predicts a finite stress in correspondence with the crack tip, thus overcoming the classical difficulties of LEFM theory.

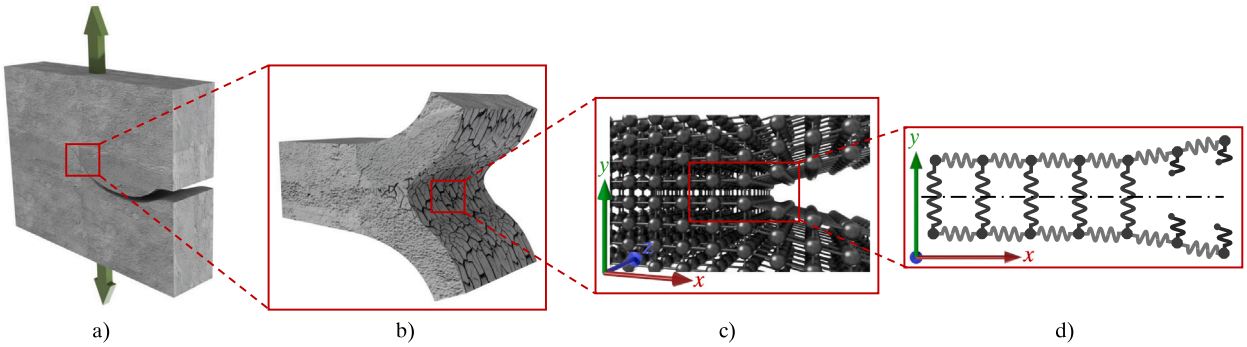

Fig. 1. Multiscale approach for modeling a crack propagating in a solid under the action of a tensile stress: (a) macroscopic phenomenon; (b) process zone with microcracking formation at the crack tip; (c) crystal lattice representation of the crack near the process zone; (d) microscopic model developed in the (x, y) plane. We plotted a symmetry line in this scheme, which further allows us to simplify the mathematical treatment of the problem.

The second important step is that we are able to investigate the thermo-mechanical response of the system under two distinct boundary conditions. In the first scenario, the stress is imposed to open the crack (isotensional conditions, generated by a soft device). In the second scenario, the displacement is prescribed to the system (isomeric conditions, induced by a hard device). These two boundary conditions correspond to the Gibbs and Helmholtz ensembles of statistical mechanics, respectively. The equivalence or non-equivalence of these statistical ensembles in the thermodynamic limit is the subject of numerous studies, with applications ranging from macromolecules behavior to mechanical phenomena, adhesion and fracture in particular (Dimitrov et al., 2009; Winkler, 2010; Manca et al., 2012, 2014; Dutta and Benetatos, 2018, 2019). We underline that the isometric condition is rarely investigated in fracture mechanics since in two- and three-dimensional geometries the domain is typically considered unbounded allowing only for the definition of an asymptotic applied stress. Here, we can study both isotensional and isometric conditions so as to make an accurate comparison.

We are thus able to determine the threshold load for crack propagation, which depends on the type of boundary condition considered and on the temperature. Specifically, we observe a classical critical behavior, with the critical load decreasing according to the law $\sqrt{1 - T/T_c}$, as the temperature T increases. As a consequence of the temperature effects on fracture propagation, we prove that in correspondence to the critical temperature T_c, the system undergoes a phase transition, corresponding to the complete rupture even in the absence of mechanical actions. We find the analytical expression for this critical temperature, which depends on both mechanical parameters and state of fracture advancement. It is noteworthy that despite the extreme simplicity of the proposed model, we provide a rigorous conceptual link between fracture phenomena and phase transitions, enabling the study of failure processes in variable temperature systems. This is also interesting because such type of thermal induced phase transition in continuous model represents by itself a theoretical important result. Moreover, we underline that phase transitions in rupture or decohesion phenomena are well known and experimentally demonstrated in several biophysical contexts (Florio and Puglisi, 2023; Blom and Godec, 2021).

The paper is structured as follows. In Section 2, we introduce the discrete model that describes fracture propagation, and we introduce the rupture strategies. In Section 3, we study the system's response within the soft device configuration (isotensional Gibbs ensemble), and in Section 4, we calculate the energy release rate (by also introducing the stress intensity factor, the fracture surface energy, and the J-integral). Then, in Section 5, we explore the system's response under hard device boundary conditions (isometric Helmholtz ensemble). In both soft and hard device configurations, we firstly examine the purely mechanical behavior of the fracture process and then we introduce the statistical mechanics to study the corresponding phase transitions. An explicit comparison between the behaviors of the two ensembles is then performed. A first analysis of the feasibility of the model is developed in Section 6, where we draw a comparison with molecular dynamics simulation for fracture in graphene. The theoretical thermal dependence of the fracture surface energy is also compared with experimental data exhibiting a linear decreasing with temperature in accordance with our theoretical results. Conclusions and a mathematical Appendix close the article.

2. The model

To introduce the model developed to study the propagation of a crack in a solid, we begin as in the classical Griffith approach, by considering an elastic body containing a crack and subjected to a tensile stress, as shown in Fig. 1(a). As anticipated in the Introduction, our goal is to determine the critical load which induces the fracture propagation, and how this load is influenced by thermal fluctuations.

To attain analytical results, we choose to develop a simple model describing the phenomenon of crack propagation. Applying a downscaling, as shown in Fig. 1(b) and (c), we first consider a discrete model composed of repetitions of identical units at the small scale, as in Fig. 1(d), and we study the continuum limit that gives us insights into the mesoscopic phenomena.

We may think to this model as a paradigmatic system mimicking the fracture process zone, where classical fracture phenomena occur (Hillerborg et al., 1976; Hillerborg, 1983; Moore and Lockner, 1995). The process zone represents the bridging element between the already opened crack and the intact portion of the solid, whether the material is ductile or brittle. In the first case, a

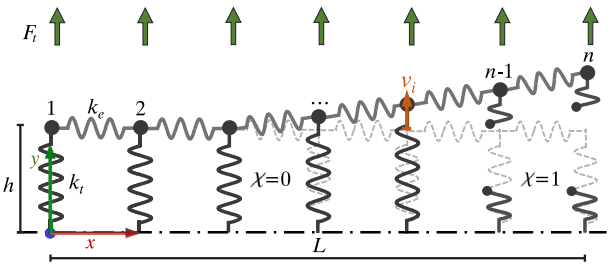

Fig. 2. Schematic representation of the model considered: $n-1$ nonbreakable horizontal elastic springs of stiffness k_e mimic the elastic properties of the solid, and the progressive rupture of the n breakable vertical units of stiffness k_t describe the crack propagation. The state of these breakable springs is described by the spin variable χ. The quantity L is the length of the system, and h is its height. We study the response of the system when is subjected to a total tensile force F, uniformly applied to all units (isotensional condition). In the following Sections, we also analyze the isometric condition, which prescribe the overall displacement.

sort of plastic and damage phenomena (dislocations and voids nucleation) are observed around the crack tip (Hilton and Hutchinson, 1971; Levy et al., 1971), as in the case of metals. On the other hand, failure in brittle materials is triggered by the development of microcracks around the crack tip, as in Fig. 1(b), originated by the concentration of stresses in this region, and coalescing to form a meso-scale discontinuity representing the fracture surfaces (Bazant and Kazemi, 1990; Dutler et al., 2018; Hoagland et al., 1973). It is therefore interesting to pursue a multi-scale study to understand how these local microscopic events (microcrack formation) in the process zone influence the global system response.

In more detail, the discrete system is modeled limiting the attention to a subsystem of the lattice represented in Fig. 1(c): two elastic chains accounting for the elastic properties of the material are connected by breakable bonds, describing the crack propagation, see Fig. 1(d). To further simplify the mathematical treatment of the problem, we identify an horizontal symmetry line in Fig. 1(d), and we consider the final model shown in Fig. 2, where the geometrical parameters considered are the length L along the x axis, the height h along the y axis, and the depth b along (out of plane) z axis. This model is composed of n vertical breakable units of stiffness k_t, and $n-1$ horizontal elastic springs of stiffness k_e. The position of the n contact points between horizontal and vertical springs is described by the displacement v_i $(i = 1, \dots, n)$, along the y direction. Hence, the breakable links are characterized by a strain $\varepsilon_i = v_i/h$. The horizontal elastic springs connecting the breakable units operate in shear (Maddalena et al., 2009; Puglisi and Truskinovsky, 2013), being the shear strain related to the ith unit given by $\gamma_i = (v_{i+1} - v_i)/h$. Of course, more general deformations could be considered at the expenses of analytical clarity.

To model the fracture, we assume that the vertical units are breakable and that they may be modeled as two-state elements. The intact state is linearly elastic whereas the broken state is characterized by a constant energy (equal to the fracture energy) and zero force. We observe that we can give a twofold interpretation of our model. In the first case, depicted in the first row of Fig. 3, we can interpret the proposed system as a very schematic model of the whole body, representing the competition between the elastic (and subsequently entropic) energy and the fracture dissipation. In this situation, the elastic energy of the unbroken zone coincides with the energy of the vertical and horizontal elastic links, which compete with the fracture energy. In the second case, the model describes the behavior of the process zone at a lower scale. Therefore, we consider the breaking phenomena induced by the elastic state of the system, as shown in the second row of Fig. 3. In fact, following a Barenblatt-like cohesive criterion, we assume that the energy of breakable units is characterized by the piecewise function in Fig. 3(b), describing the transition between intact and broken states. This local behavior can be introduced, e.g. through numerical approaches, in two- or three-dimensional elastic structures representing the overall body.

To be more precise, we describe in detail the differences of the two strategies in the following. Specifically, in Fig. 3(a) we observe that the state of breakable springs is defined *a priori*, and thus each spring is characterized by either a quadratic energy response (intact state) or a constant energy response (broken state). This energy constant represents the fracture energy of one breakable spring. Following the approach used in Florio et al. (2020), we introduce an internal "spin" variable χ_i $(i = 1, \dots, n)$ that assumes value $\chi_i = 0$ if the link is intact, and $\chi_i = 1$ if the link is broken, so that we can write the energy of one spring as

$$U_i(v_i) = \frac{1}{2} k_t v_i^2 \quad \text{if} \quad \chi_i = 0, \qquad U_i(v_i) = \frac{1}{2} k_t Y_M^2 \quad \text{if} \quad \chi_i = 1. \tag{1}$$

Here the constant $\frac{1}{2} k_t Y_M^2$ represents the fracture energy of one breakable spring. It means that in this first strategy, the spins are imposed *a priori*, and this approach coincides with the application of Griffith's idea, which is based on the exploration of local minima. There is no evolution of the spin state during the analysis of the system, but the model is studied for all possible spins combinations. Therefore, we can compare the energy pertaining to different spins combinations, and we can predict the evolution of the system. Let us develop this analysis later, and we anticipate here that the corresponding results will be represented by red points in the graphs.

On the other side, in Fig. 3(b), we define another fracture strategy. In this case, the broken state is attained when the displacement v_i overcomes a critical threshold Y_M. Thus the energy function of each breakable spring is defined by a piecewise function, represented by a quadratic form for small extensions and a constant for large extensions. These units thus describe the residual cohesive forces present in the process zone preceding the definitive crack opening. Unlike cohesive fracture models (e.g., Barenblatt),

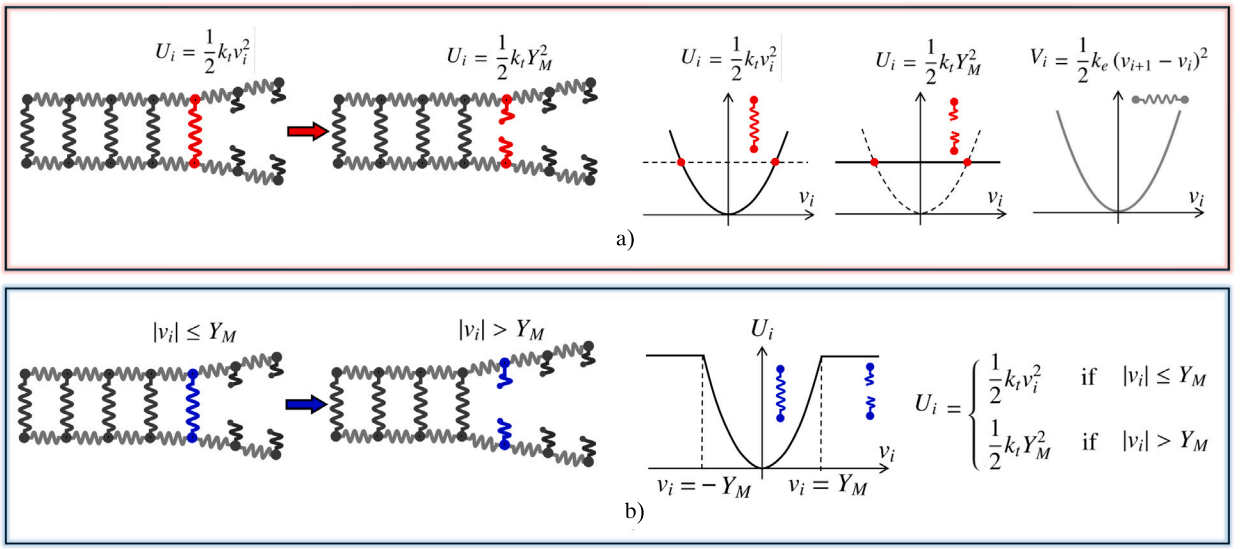

Fig. 3. Two different strategy adopted to define the braking process. In (a), we see that the state of each breakable spring is imposed *a priori*: when the vertical unit is intact ($\chi_i = 0$), the behavior is linearly elastic with the stiffness k_t, and when it is broken ($\chi_i = 0$), the energy is constant and the force drops to zero. The system is studied with all spin fixed, and Griffith's approach is applied by exploring all local energy minima. In (b), the state of each vertical unit depends on its extension, following the represented piecewise energy function. In this case, the system evolution can be studied by following the global energy minima. In both cases, the horizontal nonbreakable spring are always linear elastic with stiffness k_e (see the rightmost plot in the first row of the figure).

in which the stress in the process zone is considered to be decreasing with distance from the crack tip, the units considered in this model are simply linearly elastic (with stiffness k_t) when unbroken, with the force dropping to zero when broken. Anyway, the elastic energy of the ith breakable unit can be written as

$$U_i(v_i) = \begin{cases} \frac{1}{2}k_t v_i^2 & \text{if} \quad |v_i| \le Y_M, \\ \frac{1}{2}k_t Y_M^2 & \text{if} \quad |v_i| > Y_M. \end{cases} \tag{2}$$

In this second approach, one can consider the spins as variables in the phase space of the system, and therefore their evolution is derived from the application of statistical mechanics. This has been applied in other earlier investigations, and corresponds to the study of the global minima of the system (Florio et al., 2020; Cannizzo et al., 2022). In this work, we mostly adopt the first methodology, in Fig. 3(a), in order to generalize the Griffith criterion with the effects of the temperature. However, some applications of the second strategy will be discussed, and the corresponding results will be represented by blue points in the graphs.

With both strategies, by introducing the "spin" variables χ_i $(i = 1, \dots, n)$, we can write the internal energy (strain energy + fracture energy) of each breakable spring as

$$U_i\left(v_i, \chi_i\right) = \frac{1}{2}k_t\left[\left(1 - \chi_i\right)v_i^2 + \chi_i Y_M^2\right]. \tag{3}$$

It should be further emphasized that although this equation is the same for the two strategies introduced, conceptually the two lines of thought are completely different. On the other side, the potential energy of each horizontal nonbreakable elastic spring always reads

$$V_i(v_i) = \frac{1}{2}k_e\left(v_{i+1} - v_i\right)^2. \tag{4}$$

In the following, we study the behavior of this system under different boundary conditions. Specifically, we consider the case of an assigned stress acting on the system (by means of a soft device), and the case when a displacement is prescribed (through a rigid device). In both cases, we first study the system in the purely mechanical setting, when thermal fluctuations are absent, and then we extend the analysis to the case with thermal effects.

3. Soft device (statistical Gibbs ensemble)

We first study the mechanical response of the system subjected to a tensile stress σ, acting on the whole surface Lb. Therefore, the total potential energy for a system of n units includes the strain energy, the fracture energy and the potential energy of the external forces

$$g\left(\{v_i\}, \{\chi_i\}\right) = \frac{1}{2}k_t\sum_{i=1}^{n}\left[\left(1 - \chi_i\right)v_i^2 + \chi_i Y_M^2\right] + \frac{1}{2}k_e\sum_{i=1}^{n-1}\left(v_{i+1} - v_i\right)^2 - \sum_{i=1}^{n} f v_i, \tag{5}$$

where $f = F_t/n$ is the force applied to each unit, F_t is the total force, and the applied tensile stress is given by

$$\sigma = \frac{F_t}{bL}. \tag{6}$$

The Young and shear moduli can be introduced as follows

$$E = \frac{nk_t h}{bL}, \qquad \mu = \frac{Lk_e}{nhb}. \tag{7}$$

These expressions represent a rescaling corresponding to the continuum limit of the system. It means that the energy density is convergent to a finite value in the limit of n approaching infinity keeping the total length L fixed. It is now useful to write the total energy in non-dimensional form. For this purpose, let us introduce the non-dimensional parameters $\tilde{v}_i$ (breakable units elongation), λ (applied load), $\tilde{g}$ (energy), ν^2 (elastic ratio between Young and shear moduli) defined as follows

$$\tilde{v}_i = \frac{v_i}{Y_M}, \qquad \lambda = \frac{\sigma h}{EY_M} \qquad \tilde{g} = \frac{gh}{ELbY_M^2}, \qquad \nu^2 = \frac{\mu h^2}{EL^2}. \tag{8}$$

So doing, Eq. (5) assumes the form

$$n\tilde{g}\left(\{\tilde{v}_i\},\{\chi_i\}\right) = \frac{1}{2}\sum_{i=1}^{n}\left[\left(1-\chi_i\right)\tilde{v}_i^2 + \chi_i\right] + \frac{1}{2}n^2\nu^2\sum_{i=1}^{n-1}\left(\tilde{v}_{i+1}-\tilde{v}_i\right)^2 - \sum_{i=1}^{n}\lambda\tilde{v}_i. \tag{9}$$

In particular, since the fracture energy is proportional to $k_t Y_M^2$, we notice that $\tilde{g}$ represents the energy normalized with respect to the fracture energy, and ν^2 gives a measure of the competition between the elastic energy and the fracture energy. In order to simplify the notation, we may rewrite Eq. (9) in the compact form

$$n\tilde{g}\left(\tilde{\boldsymbol{v}},\chi\right) = \frac{1}{2}\mathbf{B}\tilde{\boldsymbol{v}}\cdot\tilde{\boldsymbol{v}} + \frac{1}{2}\chi\cdot\mathbf{1} - \lambda\tilde{\boldsymbol{v}}\cdot\mathbf{1}, \tag{10}$$

where we have introduced the tridiagonal matrix $\mathbf{B}$, and the vectors $\tilde{\boldsymbol{v}}$, χ, $\mathbf{1}$, as follows

$$\mathbf{B} = n^2\nu^2\begin{bmatrix} \mathcal{B}_1 & -1 & 0 & \dots & 0 \\ -1 & \mathcal{B}_2 & -1 & \ddots & \vdots \\ 0 & \ddots & \ddots & \ddots & 0 \\ \vdots & \ddots & -1 & \mathcal{B}_{n-1} & -1 \\ 0 & \dots & 0 & -1 & \mathcal{B}_n \end{bmatrix}, \tag{11}$$

$$\tilde{\boldsymbol{v}} = \begin{Bmatrix} \tilde{v}_1 \\ \tilde{v}_2 \\ \tilde{v}_3 \\ \dots \\ \tilde{v}_n \end{Bmatrix}, \qquad \chi = \begin{Bmatrix} \chi_1 \\ \chi_2 \\ \chi_3 \\ \dots \\ \chi_n \end{Bmatrix}, \qquad \mathbf{1} = \begin{Bmatrix} 1 \\ 1 \\ 1 \\ \dots \\ 1 \end{Bmatrix}. \tag{12}$$

Here, we defined $\mathcal{B}_i = \left(1-\chi_i\right)/\left(n^2\nu^2\right)+2$, for $i = 2,\dots n-1$, and the first and last coefficients as it follows: $\mathcal{B}_1 = \left(1-\chi_1\right)/\left(n^2\nu^2\right)+1$, and $\mathcal{B}_n = \left(1-\chi_n\right)/\left(n^2\nu^2\right)+1$.

3.1. Equilibrium configurations

Concerning the purely mechanical system, to determine the equilibrium configurations, we consider the stationary states at fixed broken configuration defined by χ, namely

$$\frac{\partial}{\partial\tilde{\boldsymbol{v}}}\left(n\tilde{g}\left(\tilde{\boldsymbol{v}},\chi\right)\right) = \mathbf{B}\tilde{\boldsymbol{v}} - \lambda\mathbf{1} = \mathbf{0}. \tag{13}$$

The equilibrium configurations are then given by

$$\tilde{\boldsymbol{v}}_e^{\mathcal{G}} = \lambda\mathbf{B}^{-1}\mathbf{1}. \tag{14}$$

Due to the local convexity of the energy, these stationary solutions are also local energy minimizers when they are defined, and they are characterized by an equilibrium energy

$$n\tilde{g}\left(\tilde{\boldsymbol{v}}_e^{\mathcal{G}},\chi\right) =: n\tilde{g}_e\left(\chi\right) = -\frac{1}{2}\lambda^2\mathbf{B}^{-1}\mathbf{1}\cdot\mathbf{1} + \frac{1}{2}\chi\cdot\mathbf{1}. \tag{15}$$

Here and in the following, we adopt the superscript $\mathcal{G}$ for the soft device (Gibbs) equilibrium solutions, whereas we will adopt the superscript $\mathcal{H}$ for the hard device (Helmholtz) case. The expression in Eq. (15) defines the non-dimensional energy of the system at assigned applied load λ, and assigned fracture configuration χ. For the moment, the vector χ is completely arbitrary. Thus, we might consider an arbitrary number of interacting cracks in a finite domain. However, for the sake of simplicity, and in accordance with the classical Griffith approach, we restrict the attention to the *single domain wall* fracture configuration. In other words we

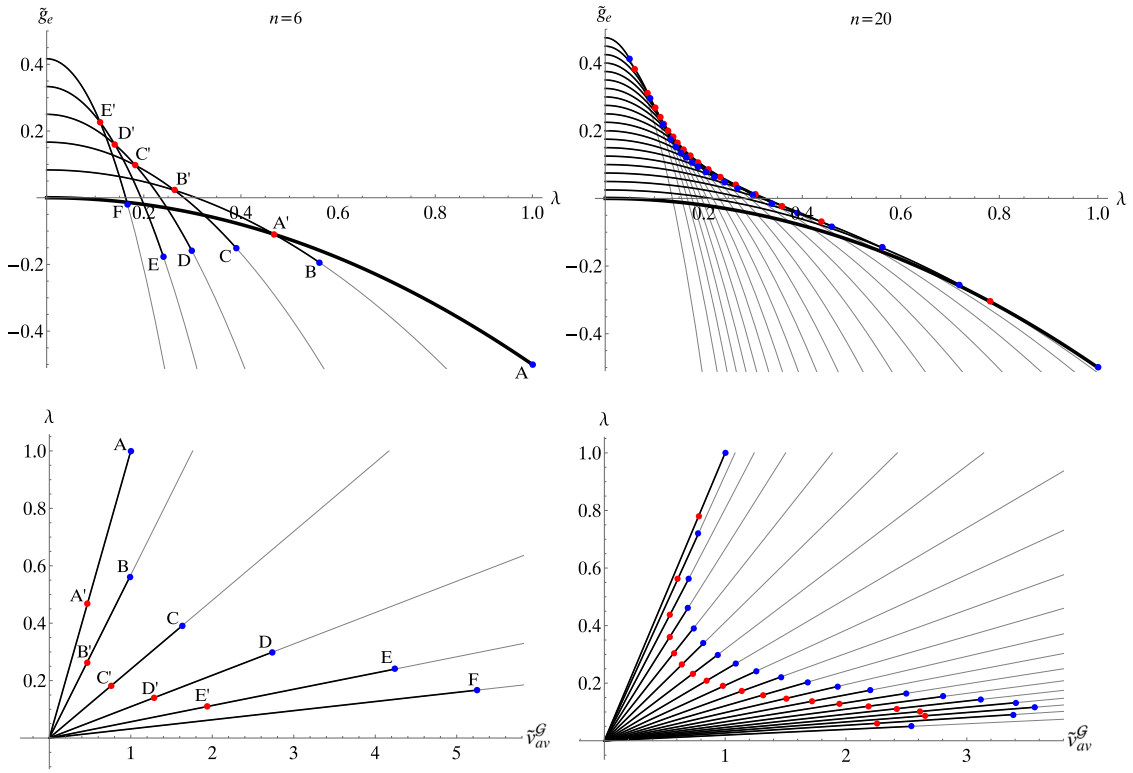

Fig. 4. Equilibrium configurations for the Gibbs discrete system. Top panels: minimized energy $\tilde{g}_e$ as function of the stress λ for different values of m. Bottom panels: force–displacement curves for different values of m (here, $\tilde{v}^{\mathcal{G}}_{av} = \tilde{\boldsymbol{v}} \cdot \mathbf{1}/n$ is the average non-dimensional displacement). The left panels show the results for a system with $n = 6$, while the right panels show the results for a system with $n = 20$. In each panel gray curves describe the system response with a fixed number of broken units m. Moreover, in the energy diagrams, the intact configuration is represented by the thick curve at the bottom, while each upper curve illustrates a configuration with an additional broken unit. The blue points indicate the critical threshold represented by the condition $\tilde{v}_{n-m} = 1$. The red points describe the situation where the energy of the system with m broken units equals the energy of the system with $m+1$ broken units. The parameter used in this diagram is $\nu^2 = 0.1$.

consider fracture configurations where the system is decomposed into a segment of m broken links on the right, and a segment of $n-m$ intact links on the left. We then study the (energetic) conditions for the propagation of such a fracture configuration. Observe that when all the links are broken, **B** is singular. For an arbitrary configuration, to prove the invertibility of the tridiagonal matrix **B** is not trivial, being this matrix not strictly diagonally dominant (Meurant, 1992). On the other hand, in the case of large systems and single domain wall solutions, we will obtain explicit expressions of the determinant, so that we are able to prove the invertibility (see Eq. (40) and Appendix).

In Fig. 4 (top panels), we show the energy curves corresponding to a system with a variable number m of broken units: the thickest curve corresponds to the fully intact system ($m = 0$), while the other curves are characterized by an increasing value of m. We can anticipate some considerations, which will be taken up later in the discussion. We first observe that it is possible to prove that each single wall equilibrium configuration is monotonic, which means that the displacements $\tilde{v}_i$ are increasing with i (going from the left intact domain to the right broken domain). As a result, each equilibrium energy curve is defined for a stress value lower than a given threshold stress, corresponding to the last intact element attaining the limit condition $\tilde{v}_{n-m} = 1$ (blue points A, B, ..., F in the figure), see Fig. 4 (top panel). Thus the system follows the equilibrium branch up to these points, if we assume that it remains in a given equilibrium branch until it becomes unstable. This represents the so called *maximum delay convention* in multistable systems and reproduces the limit case of systems that are not able to overcome any energy barrier (Puglisi and Truskinovsky, 2000). This strategy, represented in Fig. 3(b), can be related to the Barenblatt model, where the pull forces between the fracture faces try to prevent its propagation until the moment of rupture. Conversely, the red points A′, B′, ..., E′ represent the positions where the energy of the system with m broken units equals the energy of the system with $m+1$ broken units. Hence, the red points represent the energy thresholds obtained through a *discrete version* of the Griffith's energy crack propagation criterion. This analysis corresponds to the rupture strategy defined in Fig. 3(a). By applying the Griffith's approach, the intersection points between adjacent energy curves were considered, but the curves could be plotted for any value of applied stress, so the blue points are not relevant in this case. Interestingly, we observe that while in a system with few units (left panels), the difference between the blue and red points is evident, in a system with a higher number of units (anticipating the rigorous continuum limit studied in the following), the blue points converge to the red points (right panels). This implies that in the continuum limit, the Griffith's

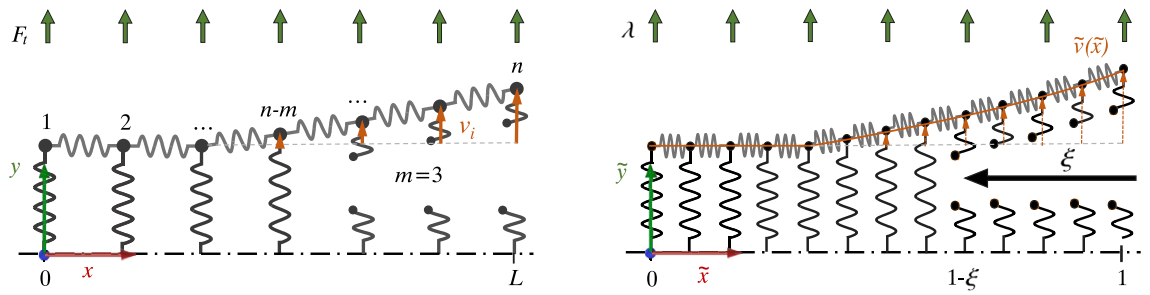

Fig. 5. Scheme of the continuum limit defined by $n \to \infty$. As n increases, the system represents a continuous medium of finite length with well-defined elastic properties and energy.

threshold (see scheme in Fig. 3a) coincides with the existence condition of a local energy minimum (see scheme in Fig. 3b). This gives an interesting energetic interpretation of Griffith's criterion in relation to local stability. This will be analytically demonstrated in the next Sections, for both Gibbs and Helmholtz ensembles in the continuum limit. We also remark that our model, differently from the classical Griffith approach, also allows for the determination of the nucleation crack force. Although many of the results that follow can be established in the discrete case, which are important for systems in which discrete effects are not negligible, we will analyze all the details directly in the case with large n, which gives a much clearer analytical example.

In Fig. 4 (bottom panels), we plot the equilibrium force as a function of the average displacement $\tilde{v}_{av}^{\mathcal{C}} = \tilde{\boldsymbol{v}} \cdot \mathbf{1}/n$. In these plots, each straight line corresponds to a different value of m and the blue and red point are exactly defined as before. As expected, the system becomes softer as the number m of broken elements increases. Also the equilibrium force of red limit points converges to the one of blue points for increasing values of n.

3.2. Continuum limit

Starting from the minimized energy, obtained in Eq. (15), we consider now the continuum limit attained with $n \to \infty$ (see Fig. 5). It means that the total length L remains fixed so that the shear horizontal spring length $\ell = L/n$ approaches zero. We then introduce $\xi = m/n$, representing the broken fraction of the system. The quantity ξ, in the continuum limit, can be considered as a continuum variable that varies from 0 (intact system) to 1 (completely broken system). It identifies the position of the propagating fracture front, assuming that the crack nucleates on the right and widens toward the left. The development of the analytic expressions for the discrete system, and for the related continuum limit, requires the explicit calculus of the inverses of tridiagonal matrices. To this end, we performed extensive calculations using Usmani (1994) theorems concerning tridiagonal matrix inversion (details are reported in Appendix). Eventually, the energy in the continuum limit reads

$$\tilde{g}_e(\xi) = -\frac{1}{2}\lambda^2 - \frac{1}{2}\frac{\lambda^2}{\nu^2}\xi\left[\nu^2 + \nu\xi\coth\left(\frac{1-\xi}{\nu}\right) + \frac{\xi^2}{3}\right] + \frac{\xi}{2}. \tag{16}$$

We remark that the term $\xi/2$ represents the (non dimensional) fracture energy, increasing as fracture propagates.

Interestingly, we now prove that it is possible to deduce the same result for the total energy of the system at equilibrium through a variational approach, starting from a continuous model. In passing, we can also observe that the continuous system is similar to a shear elastic beam placed on a Winkler foundation consisting of a breakable extensional layer (Dillard et al., 2018).

Defined $x \in [0, L]$, we introduce the displacement of the system along y as a continuous function $v = v(x)$. In order to describe the fracture propagation, we also introduce a state function χ. This variable assumes the value 1 in the intact region and the value 0 in the broken region. This is a simple choice, coherent with the energy described for the previous discrete model in Fig. 3. However, alternative more complicated (continuously varying) profiles of χ can be implemented as is done for example in phase field models (Ren et al., 2019; Miehe et al., 2010).

Considering the discrete version of the energy in Eq. (5), and the rescaled elastic constants defined in Eq. (7), the continuum limit of total energy can be obtained by the functional

$$g(v, v') = \int_0^L \left[\frac{1}{2}E\left(\frac{v^2(x)}{h^2}(1-\chi(x)) + \chi(x)\frac{Y_M^2}{h^2}\right)bh + \frac{1}{2}\mu v'^2(x)bh - \sigma\frac{v(x)}{h}bh\right]dx. \tag{17}$$

For this continuum system, the extensional and shear strains can be defined respectively as

$$\epsilon(x) = \frac{v(x)}{h}, \quad \gamma(x) = \frac{dv(x)}{dx} =: v'(x), \tag{18}$$

and the shear force is given by

$$S_f(x) = \mu\frac{dv(x)}{dx}. \tag{19}$$

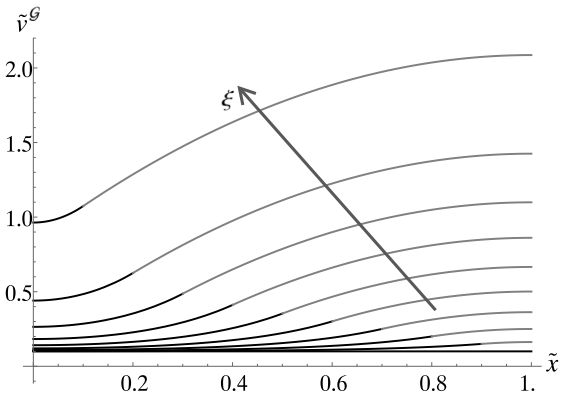

Fig. 6. Displacement function for the equilibrium configurations of the continuous system. Each curve represents a different value of ξ. Black lines describe the displacement $\tilde{v}_I^{\mathcal{G}}$ in the intact region, and gray lines represent $\tilde{v}_B^{\mathcal{G}}$ in the broken region. The parameters used to obtain these curves are $\nu = 0.2$ and $\lambda = 0.1$.

By rescaling x with $\tilde{x} = x/L$, where $\tilde{x} \in [0, 1]$, and v with $\tilde{v} = v/Y_M$, we can rewrite the total energy in the following non-dimensional form

$$\tilde{g}(\tilde{v}, \tilde{v}') = \int_0^1 \left[\frac{1}{2}(1 - \chi(\tilde{x}))\,\tilde{v}^2(\tilde{x}) + \frac{1}{2}\chi(\tilde{x}) + \frac{1}{2}\nu^2\tilde{v}'^2(\tilde{x}) - \lambda\tilde{v}(\tilde{x})\right] d\tilde{x}, \tag{20}$$

where we used the non dimensional quantities defined in Eq. (8). Hence, in order to find the equilibrium configurations, we look for the extremals of $\tilde{g}$, obtained by the classical Euler–Lagrange equation

$$\frac{d}{d\tilde{x}}\frac{\partial}{\partial\tilde{v}'}\kappa(\tilde{v}, \tilde{v}') - \frac{\partial}{\partial\tilde{v}}\kappa(\tilde{v}, \tilde{v}') = 0, \tag{21}$$

where κ represents the Lagrangian density

$$\kappa(\tilde{v}, \tilde{v}') = \frac{1}{2}(1 - \chi(\tilde{x}))\,\tilde{v}^2(\tilde{x}) + \frac{1}{2}\chi(\tilde{x}) + \frac{1}{2}\nu^2\tilde{v}'^2(\tilde{x}) - \lambda\tilde{v}(\tilde{x}). \tag{22}$$

We obtain the classical equation

$$\nu^2\tilde{v}''(\tilde{x}) - (1 - \chi(\tilde{x}))\,\tilde{v}(\tilde{x}) = -\lambda, \tag{23}$$

which can be easily solved as follows. In the broken domains ($\chi = 1$), the solution is

$$\tilde{v}_B^{\mathcal{G}}(\tilde{x}) = -\frac{\lambda}{2\nu^2}\tilde{x}^2 + A\tilde{x} + B, \tag{24}$$

whereas, in the intact domains ($\chi = 0$), the displacement is given by

$$\tilde{v}_I^{\mathcal{G}}(\tilde{x}) = Ce^{\tilde{x}/\nu} + De^{-\tilde{x}/\nu} + \lambda. \tag{25}$$

Here, the subscript B means broken, and the subscript I means intact. As before, we address the case concerning a single domain wall separating the intact region $\tilde{x} \in (0, 1 - \xi)$ from the broken region $\tilde{x} \in (1 - \xi, 1)$. The coefficients can be obtained by imposing zero shear forces at the extremities, and shear and displacement continuity at the interface (propagation front)

$$\begin{cases} \tilde{v}_I'^{\mathcal{G}}(0) = 0, \\ \tilde{v}_B'^{\mathcal{G}}(1) = 0, \\ \tilde{v}_I^{\mathcal{G}}(1 - \xi) = \tilde{v}_B^{\mathcal{G}}(1 - \xi), \\ \tilde{v}_I'^{\mathcal{G}}(1 - \xi) = \tilde{v}_B'^{\mathcal{G}}(1 - \xi). \end{cases} \tag{26}$$

We then obtain

$$\begin{aligned} \tilde{v}_I^{\mathcal{G}}(\tilde{x}) &= \frac{\lambda\xi}{\nu\sinh\left(\frac{1-\xi}{\nu}\right)}\cosh\left(\frac{\tilde{x}}{\nu}\right) + \lambda && \tilde{x} \in (0, 1 - \xi), \\ \tilde{v}_B^{\mathcal{G}}(\tilde{x}) &= -\frac{1}{2}\frac{\lambda}{\nu^2}\left[\tilde{x}^2 - (1 - \xi)^2\right] + \frac{\lambda}{\nu^2}(\tilde{x} - 1 + \xi) + \frac{\lambda\xi}{\nu}\coth\left(\frac{1-\xi}{\nu}\right) + \lambda && \tilde{x} \in (1 - \xi, 1). \end{aligned} \tag{27}$$

In Fig. 6, it is possible to observe the graphical representation of an example of displacement given in Eq. (27). We remark the monotonic behavior of the displacement, as mentioned above.

Importantly, we observe that if we substitute the functions $\tilde{v}_I^{\mathcal{G}}$ and $\tilde{v}_B^{\mathcal{G}}$ in the total energy defined in Eq. (20), we obtain the same expression for the minimized energy $\tilde{g}_e$ given in Eq. (16). Thus, as in the classical Γ-convergence theory, the minima of the discrete system converge, for $n \to \infty$, to the minima of the continuous model (Braides, 2002; Dal Maso, 2012).

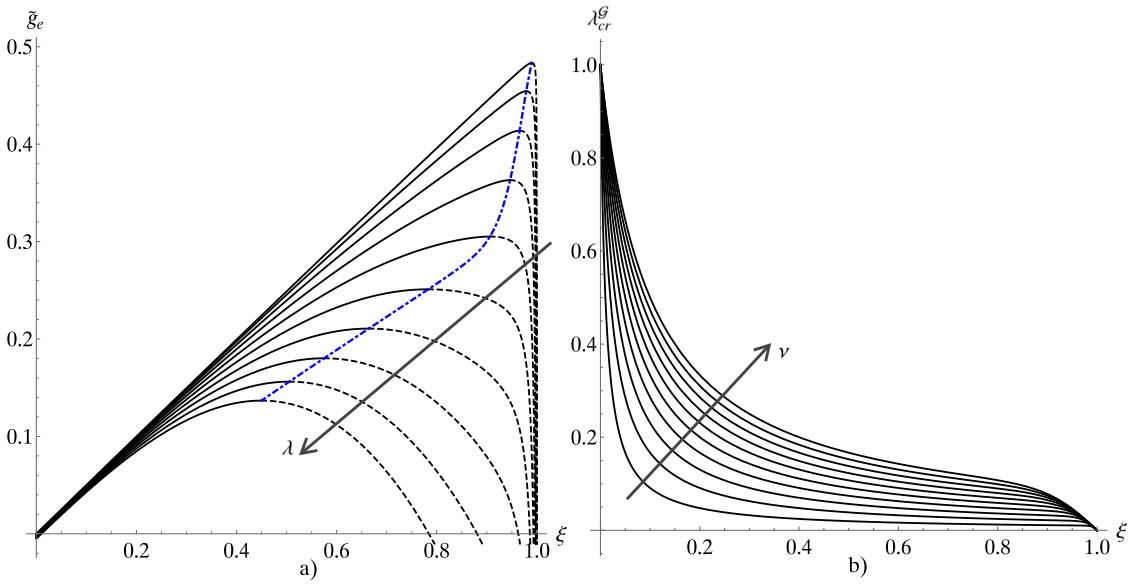

Fig. 7. Analysis of the equilibrium configurations for the Gibbs continuous system. Panel (a): minimized energy versus detached extension ξ, for different values of λ. The blue dashed curve passes through the points of maximum energy. For this diagrams the values $\nu = 0.05$ and $\lambda \in [0.01, 0.1]$ are used. Panel (b): critical load (versus ξ) required for fracture propagation according to the Griffith energy criterion: $\lambda_{cr}^{\mathcal{G}}$ decreases as the system progressively breaks. The different curves correspond to the values of $\nu \in [0.01, 0.1]$.

3.3. Griffith energy criterion for fracture propagation

After determining the equilibrium configurations for a system describing an elastic solid weakened by a flaw, our attention shifts to examining fracture propagation through the lens of Griffith's classical energy criterion. This criterion affirms that crack widening occurs when the available energy for crack growth exceeds the so called material's resistance. To apply this approach to our system, let us revisit the total energy in Eq. (16): the first two terms denote the potential energy $\tilde{\Pi}$, including the energy associated with the external load and the strain energy, while the third term represents the fracture energy $\tilde{\Gamma}$. Considering non-dimensional quantities, we study the propagation of a fracture with extension ξ, starting at the right end of the system, and moving to the left. The rate of change of the potential energy, $\partial\tilde{\Pi}/\partial\xi$, corresponds to the crack driving force ($\tilde{G} = -\partial\tilde{\Pi}/\partial\xi$ is the energy release rate, see the next Section), and the rate of change of the fracture energy $\partial\tilde{\Gamma}/\partial\xi$ represents the material resistance to overcome. It follows that, according to Griffith criterion, we must have

$$\frac{\partial\tilde{\Pi}}{\partial\xi} + \frac{\partial\tilde{\Gamma}}{\partial\xi} = \frac{\partial\tilde{g}_e(\xi)}{\partial\xi} < 0, \tag{28}$$

in order for the crack to propagate. The derivative of the energy in Eq. (16) with respect to the crack length is

$$\frac{\partial\tilde{g}_e(\xi)}{\partial\xi} = \frac{1}{2} - \frac{1}{2}\lambda^2 - \lambda^2\frac{\xi}{\nu}\coth\left(\frac{1-\xi}{\nu}\right) - \frac{\lambda^2\xi^2}{2\nu^2}\coth^2\left(\frac{1-\xi}{\nu}\right) \tag{29}$$

and therefore we obtain the following condition for the crack propagation

$$\lambda > \lambda_{cr}^{\mathcal{G}} := \frac{1}{1 + \frac{\xi}{\nu}\coth\left(\frac{1-\xi}{\nu}\right)}. \tag{30}$$

In Fig. 7(a), we show the equilibrium total energy $\tilde{g}_e$ versus ξ, for different values of the applied load λ. Note that when higher forces are applied, fracture propagation is attained in correspondence of a smaller broken region, consistently with the classical Griffith criterion. In Fig. 7(b), we plot the critical stress, inducing crack propagation, versus the damage state ξ, for different values of the stiffness ratio coefficient ν. Observe that the critical stress decreases with ξ, confirming that the critical load decreases as the crack extension ξ increases.

Interestingly, the displacement $\tilde{v}_{cr}^{\mathcal{G}}$ corresponding to $\lambda_{cr}^{\mathcal{G}}$, and evaluated at the fracture propagation front $\tilde{x} = 1 - \xi$, is exactly the critical threshold 1 (or Y_M with dimensional quantities). Indeed, if we evaluate Eq. (27) for $\tilde{x} = 1 - \xi$ and $\lambda = \lambda_{cr}^{\mathcal{G}}$, we get

$$\tilde{v}_B^{\mathcal{G}}(1-\xi) = \lambda_{cr}^{\mathcal{G}}\left[\frac{\xi}{\nu}\coth\left(\frac{1-\xi}{\nu}\right) + 1\right]. \tag{31}$$

Then, by substituting the critical load $\lambda_{cr}^{\mathcal{G}}$ from Eq. (30), we obtain $\tilde{v}_B^{\mathcal{G}}(1-\xi) = 1$, when $\lambda = \lambda_{cr}$. This result is consistent with previous observation on the convergence for $n \to \infty$ of the two energetic and Griffith fracture strategies, described by the red points and the

blue points in Fig. 4. This means that Griffith's stress threshold exactly corresponds to the existence threshold of any equilibrium solution at ξ fixed. We stress that this result gives a new energetic interpretation of the Griffith's approach, being consistent with the scheme based on breakable springs described by the piece-wise energy function shown in Fig. 3(b).

3.4. Temperature effects within the Gibbs ensemble

In this Section, we focus on the main aim of this paper, i.e. the analysis of temperature effects on the fracture behavior. The main theoretical novelty is based on the extension of the Griffith criterion stated in Eq. (28) for the purely mechanical system, by substituting the total mechanical energy with the Gibbs free energy

$$\mathcal{G} = H - TS, \tag{32}$$

where T is the temperature, H is the enthalpy of the system, and S is its entropy.

To take care of thermal fluctuations, in the classical framework of equilibrium statistical mechanics, we consider again the discrete system and in particular we start from the energy g, defined in Eq. (5). Assuming that the system is at thermodynamic equilibrium with a thermal bath at temperature T, we can evaluate the Gibbs partition function associated with the canonical distribution of the statistical mechanics (Gibbs, 1902; Weiner, 1983). We have

$$\mathcal{Z}^{\mathcal{G}}(\chi, T) = \int_{\mathbf{R}^n} \exp\left[-\frac{g(\boldsymbol{v}, \chi)}{k_B T}\right] d\boldsymbol{v}, \tag{33}$$

where $\boldsymbol{v} = \{v_1, v_2 \dots v_n\}$, $\chi = \{\chi_1, \chi_2, \dots \chi_n\}$, and k_B is the Boltzmann constant. Substituting g with its non-dimensional counterpart $\tilde{g}$ introduced in Eq. (10), and $\boldsymbol{v}$ by $\tilde{\boldsymbol{v}} = \boldsymbol{v}/Y_M$, we have

$$\mathcal{Z}^{\mathcal{G}}(\chi, T) = (Y_M)^n \int_{\mathbf{R}^n} \exp\left[-\tilde{\beta}\tilde{g}(\tilde{\boldsymbol{v}}, \chi)\right] d\tilde{\boldsymbol{v}}, \tag{34}$$

where we have defined the non-dimensional parameter $\tilde{\beta}$ as

$$\tilde{\beta} = \frac{E L b Y_M^2}{h k_B T}. \tag{35}$$

Observe that this parameter can be considered as a measure of the ratio between fracture and thermal energy. By using Eqs. (10) and (34), we obtain

$$\begin{aligned} \mathcal{Z}^{\mathcal{G}}(\chi, T) &= (Y_M)^n \int_{\mathbf{R}^n} \exp\left[-\frac{\tilde{\beta}}{n}\left(\frac{1}{2}\mathbf{B}\tilde{\boldsymbol{v}}\cdot\tilde{\boldsymbol{v}} + \frac{1}{2}\chi\cdot\mathbf{1} - \lambda\tilde{\boldsymbol{v}}\cdot\mathbf{1}\right)\right] d\tilde{\boldsymbol{v}} \\ &= (Y_M)^n \exp\left[-\frac{\tilde{\beta}}{2n}\chi\cdot\mathbf{1}\right] \int_{\mathbf{R}^n} \exp\left[-\frac{\tilde{\beta}}{2n}\mathbf{B}\tilde{\boldsymbol{v}}\cdot\tilde{\boldsymbol{v}} + \frac{\tilde{\beta}}{n}\lambda\tilde{\boldsymbol{v}}\cdot\mathbf{1}\right] d\tilde{\boldsymbol{v}}. \end{aligned} \tag{36}$$

The integration can be performed through the classical Gaussian integral

$$\int_{\mathbf{R}^n} \exp\left[-\mathbf{M}\mathbf{y}\cdot\mathbf{y} - \mathbf{a}\cdot\mathbf{y}\right] d\mathbf{y} = \sqrt{\frac{\pi^n}{\det\mathbf{M}}} \exp\left[\frac{1}{4}\mathbf{M}^{-1}\mathbf{a}\cdot\mathbf{a}\right], \tag{37}$$

which is valid for a positive definite symmetric matrix $\mathbf{M}$, and for any vector $\mathbf{a}$. We obtain

$$\mathcal{Z}^{\mathcal{G}}(\chi, T) = (Y_M)^n \sqrt{\frac{(2\pi n)^n}{\tilde{\beta}^n \det\mathbf{B}}} \exp\left[-\frac{\tilde{\beta}}{n}\left(\frac{1}{2}\chi\cdot\mathbf{1} - \frac{1}{2}\lambda^2\mathbf{B}^{-1}\mathbf{1}\cdot\mathbf{1}\right)\right], \tag{38}$$

which, recalling the expression obtained in Eq. (15), can be rewritten in terms of the minimized mechanical energy

$$\mathcal{Z}^{\mathcal{G}}(\chi, T) = (Y_M)^n \sqrt{\frac{(2\pi n)^n}{\tilde{\beta}^n \det\mathbf{B}}} \exp\left[-\tilde{\beta}\tilde{g}_e(\chi)\right]. \tag{39}$$

While this expression can be studied numerically, to get insight in the results, we consider here the case of large systems under the hypothesis of single domain wall fractured configurations, assigned by the parameter $\xi \in [0, 1[$. In the limit for $n \to \infty$, the quantity $\tilde{g}_e(\chi)$ in Eq. (39) can be substituted with the explicit expression $\tilde{g}_e(\xi)$ obtained in Eq. (16). In Appendix, we also prove that the asymptotic value of $\det\mathbf{B}$, for $n \to \infty$, is given by

$$\det\mathbf{B} \underset{n\to\infty}{\sim} \left(n^2\nu^2\right)^n \frac{\sinh\left(\frac{1-\xi}{\nu}\right)}{n\nu}. \tag{40}$$

Therefore, the partition function in the Gibbs ensemble reads

$$\mathcal{Z}^{\mathcal{G}}(\xi, T) = (Y_M)^n \sqrt{\frac{(2\pi n)^n n\nu}{\tilde{\beta}^n \left(n^2\nu^2\right)^n \sinh\left(\frac{1-\xi}{\nu}\right)}} \exp\left[-\tilde{\beta}\tilde{g}_e(\xi)\right]. \tag{41}$$

It is worth noticing that, consistently with the Griffith approach, we have evaluated the partition function at assigned ξ, so that we will obtain the Gibbs free energy at fixed ξ. Different approaches have been proposed in the analysis of the thermal effects in

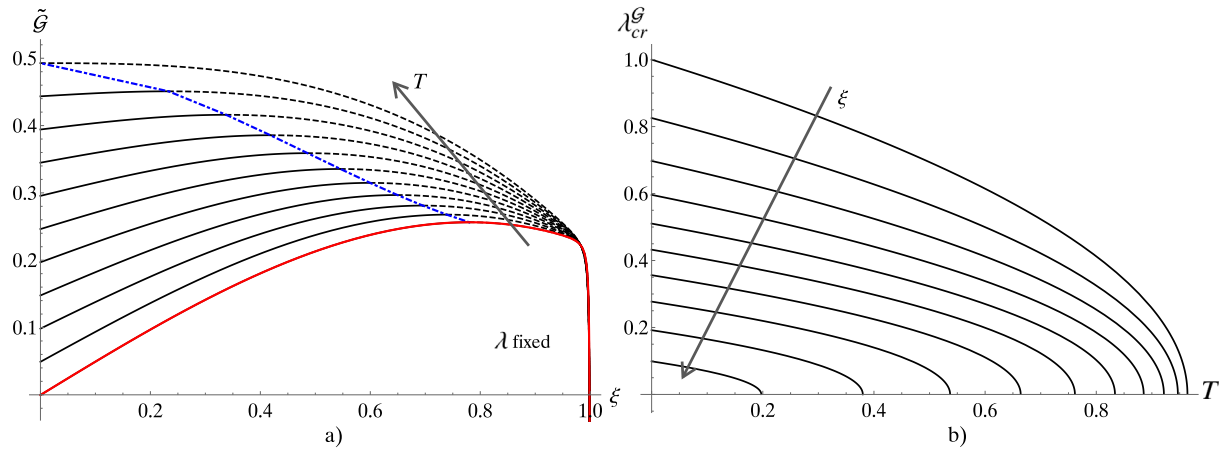

Fig. 8. Temperature effects on the system within the Gibbs ensemble. In panel (a), the non-dimensional Gibbs free energy $\tilde{\mathcal{G}}$ is plotted versus the detached extension ξ: the curves describe the behavior at different temperatures T such that $1/\tilde{\beta} \in [0, 0.02]$. The blue dashed curve passes through the energy maximum points. The red curve represent the purely mechanical system at $T = 0$. For this diagram the values $\nu = 0.02$ and $\lambda = 0.025$ have been used. In panel (b), we show the influence of the temperature on the critical stress required for fracture propagation: the different curves correspond to different values of ξ. These curves are obtained with $\nu = 0.5$. We also assumed $ELbY_M^2/(hk_B) = 1$ so that $T = 1/\tilde{\beta}$.

unzipping and decohesion phenomena of discrete systems in Florio et al. (2020), where the energy was minimized also with respect to the fraction of broken system ξ. We can now, following the Griffith approach, develop the new temperature dependent stability criterion. Indeed, we can evaluate the Gibbs free energy at fixed ξ, which is defined as (Manca et al., 2012; Gibbs, 1902; Weiner, 1983)

$$\mathcal{G}(\xi, T) = -k_B T \ln\left(\mathcal{Z}^{\mathcal{G}}(\xi, T)\right). \tag{42}$$

Its non-dimensional version is

$$\tilde{\mathcal{G}}(\xi, T) = \frac{h}{ELbY_M^2}\mathcal{G}(\xi, T) = -\frac{hk_B T}{ELbY_M^2}\ln \mathcal{Z}^{\mathcal{G}}(\xi, T) = -\frac{1}{\tilde{\beta}}\ln \mathcal{Z}^{\mathcal{G}}(\xi, T). \tag{43}$$

In order to evaluate $\ln \mathcal{Z}^{\mathcal{G}}$, we introduce the constant c defined as

$$c = \left(Y_M\right)^n \sqrt{\frac{(2\pi n)^n n\nu}{\tilde{\beta}^n \left(n^2\nu^2\right)^n}}, \tag{44}$$

and we obtain

$$\ln \mathcal{Z}^{\mathcal{G}}(\xi, T) = \ln c - \frac{1}{2}\ln\left[\sinh\left(\frac{1-\xi}{\nu}\right)\right] - \tilde{\beta}\tilde{g}_e(\xi). \tag{45}$$

Eventually, we can write the non-dimensional Gibbs free energy in the form

$$\tilde{\mathcal{G}}(\xi, T) = \tilde{\mathcal{G}}_0(T) + \frac{1}{2\tilde{\beta}}\ln\left[\sinh\left(\frac{1-\xi}{\nu}\right)\right] + \tilde{g}_e(\xi), \tag{46}$$

where the first term $\tilde{\mathcal{G}}_0 = -\ln c/\tilde{\beta}$ takes into account the non-influential multiplicative constant in the partition function $\mathcal{Z}^{\mathcal{G}}$ (this term depends on the temperature, but not on ξ), the second term accounts for the entropic contribution with temperature effects, and the last term represents the enthalpic part, identical to the system energy when thermal effects are neglected, as defined in Eq. (16), thus including the elastic (internal) energy and the fracture energy term $\xi/2$.

By following the same approach of the Griffith criterion for the purely mechanical case, in the presence of temperature we have to consider the Gibbs or Helmholtz free energies, depending on the boundary condition adopted. In the case here considered of assigned force, we thus extend the Griffith approach by requiring that the derivative of $\tilde{\mathcal{G}}(\xi, T)$ with respect to the extension of the fracture must be negative in order to have propagation

$$\frac{\partial \tilde{\mathcal{G}}(\xi, T)}{\partial \xi} < 0. \tag{47}$$

In this way the fracture propagation is possible when the gain in free energy overcomes the energy dissipation due to fracture. This is consistent with the principle of non-equilibrium thermodynamics, which states that free energies must always decrease during the natural evolution of a physical system.

In this case as expected the stability criterion becomes temperature-dependent. The calculation of the derivative of Eq. (46) yields the generalized Griffith criterion here proposed:

$$\frac{\partial \tilde{\mathcal{G}}(\xi, T)}{\partial \xi} = -\frac{1}{2\nu\tilde{\beta}}\coth\left(\frac{1-\xi}{\nu}\right) + \frac{1}{2} - \frac{\lambda^2}{2} - \frac{\lambda^2}{\nu}\xi\coth\left(\frac{1-\xi}{\nu}\right) - \frac{\xi^2\lambda^2}{2\nu^2}\coth^2\left(\frac{1-\xi}{\nu}\right) < 0. \tag{48}$$

After straightforward calculations, we obtain

$$\lambda^2\left[1+\frac{\xi}{\nu}\coth\left(\frac{1-\xi}{\nu}\right)\right]^2 > 1-\frac{1}{\tilde{\beta}\nu}\coth\left(\frac{1-\xi}{\nu}\right), \tag{49}$$

which leads to the necessary condition for fracture propagation

$$\lambda > \frac{\sqrt{1-\frac{\tilde{\beta}_c^{\mathcal{G}}}{\tilde{\beta}}}}{1+\xi\tilde{\beta}_c^{\mathcal{G}}}, \tag{50}$$

where $\tilde{\beta}_c^{\mathcal{G}}$ is defined as follows

$$\tilde{\beta}_c^{\mathcal{G}} = \frac{1}{\nu}\coth\left(\frac{1-\xi}{\nu}\right). \tag{51}$$

We can also introduce the critical temperature $T_c^{\mathcal{G}}$ of the system by means of the relation

$$\frac{\tilde{\beta}_c^{\mathcal{G}}}{\tilde{\beta}} = \frac{T}{T_c^{\mathcal{G}}}. \tag{52}$$

We observe that $T_c^{\mathcal{G}}$ depends on the crack extension ξ and assumes the following explicit expression

$$T_c^{\mathcal{G}} = \frac{\nu E L b Y_M^2}{h k_B \coth\left(\frac{1-\xi}{\nu}\right)} = \frac{\sqrt{\mu E} b Y_M^2}{k_B \coth\left(\frac{L-\zeta}{h}\sqrt{\frac{E}{\mu}}\right)}, \tag{53}$$

where we have introduced $\zeta = \xi L$, which is the crack extension, defined with its real physical dimensions. Based on this definition, we can write an alternative form of Eq. (50), which describes explicitly the temperature dependent propagation criterion

$$\lambda > \frac{\sqrt{1-\frac{T}{T_c^{\mathcal{G}}}}}{1+\frac{\xi}{\nu}\coth\left(\frac{1-\xi}{\nu}\right)} = \lambda_{cr}^{\mathcal{G}}(0)\sqrt{1-\frac{T}{T_c^{\mathcal{G}}}} =: \lambda_{cr}^{\mathcal{G}}(T), \tag{54}$$

where $\lambda_{cr}^{\mathcal{G}}(0)$ is the critical load defined for the purely mechanical system in Eq. (30).

The obtained results have been summarized in Fig. 8. In particular in Fig. 8(a) we show how the energy is influenced by thermal fluctuations. All the curves are obtained with the same value of the applied stress λ. We observe that for increasing temperature, the maximum of the energy function, assigning the Griffith propagation threshold, shifts toward lower values of ξ. Therefore, as the temperature is increased, a smaller broken region is sufficient to generate a Griffith instability. In other words *thermal fluctuations promote fracture propagation*.

In Fig. 8(b) we further describe this effect by plotting how the stress required for fracture propagation is influenced by thermal fluctuations. Observe that for the assigned initial crack length ξ the Griffith propagation threshold decreases as temperature increases. In particular, when $T \to 0$ we obtain that Eq. (54) converges to Eq. (30). It is important to underline that we observe the emergence of a critical behavior, which is characterized by a phase transition, describing the spontaneous breaking of the system at a critical temperature $T = T_c^{\mathcal{G}}$. In other words, for supercritical temperatures, the system is fully broken even without the application of external loads, only due to the thermal fluctuations acting on the system. When the temperature reaches its critical value $T_c^{\mathcal{G}}$ the stress required for fracture propagation is zero, evidencing again the existence of the phase transition.

To conclude, in Fig. 9 we show the force–extension behavior of the system with varying temperature. The different straight lines correspond to different values of the crack extension ξ. The colors represent different temperatures of the system, and the endpoints of the straight lines represent the Griffith stability threshold, which we have already determined analytically. It is clearly seen that critical stress decreases with temperature as described above. We underline that the average displacement $\tilde{v}_{av}^{\mathcal{G}}$ is calculated from the expectation value of the displacement conjugated to the applied stress λ in the Gibbs ensemble. Specifically, recalling Eqs. (39) and (42) we have

$$\begin{aligned}\langle\tilde{v}\rangle^{\mathcal{G}} &= -\frac{\partial\tilde{\mathcal{G}}(\xi,T)}{\partial\lambda} = \frac{1}{\tilde{\beta}\mathcal{Z}^{\mathcal{G}}(\xi,T)}\frac{\partial\mathcal{Z}^{\mathcal{G}}(\xi,T)}{\partial\lambda} = \frac{1}{\tilde{\beta}\mathcal{Z}^{\mathcal{G}}(\xi,T)}\mathcal{Z}^{\mathcal{G}}(\xi,T)\left(-\tilde{\beta}\right)\frac{\partial\tilde{g}_e(\xi,T)}{\partial\lambda}\\ &= \lambda + \frac{\lambda\xi}{\nu^2}\left[\nu^2+\nu\xi\coth\left(\frac{1-\xi}{\nu}\right)+\frac{\xi^2}{3}\right] = \tilde{v}_{av}^{\mathcal{G}}(T) = \tilde{v}_{av}^{\mathcal{G}}(0),\end{aligned} \tag{55}$$

where $\tilde{v}_{av}^{\mathcal{G}}(0)$ is the purely mechanical averaged displacement. Hence, we obtain that the expression for this quantity is not influenced by thermal fluctuations.

4. Energy release rate in the soft device configuration

In this Section, with the aim of comparing our theory with the classical fracture approaches when thermal effects are neglected, we determine the temperature dependent expression of the "energy release rate", of the system. We next also introduce the concepts of stress intensity factor and J-integral for our system.

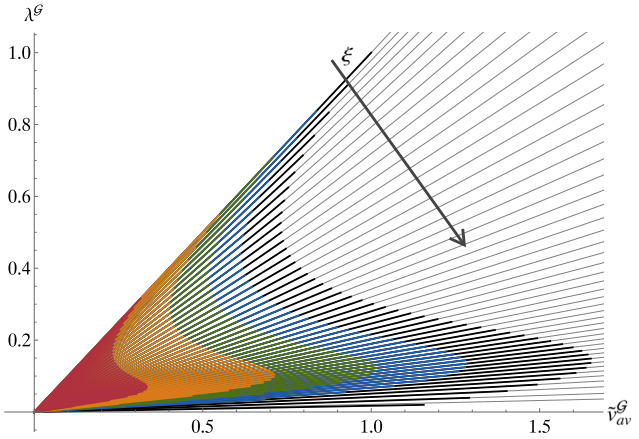

Fig. 9. Temperature effects on force–displacement relation within the Gibbs ensemble. We remember that $\tilde{v}^{\mathcal{G}}_{av}$ is the average displacement. The different straight lines correspond to different values of ξ, and the endpoint of each line coincides with the temperature dependent Griffith threshold. The different colors represent different temperature values (the black lines correspond to the zero temperature case, and the red ones to the larger temperature). The parameter used for this diagram is $\nu = 0.4$.

Let us again begin with the purely mechanical system when thermal effects are neglected. The energy release rate is related to the variation of the potential energy Π (sum of the strain energy and the potential energy of the external load) with respect to the crack extension (Griffith, 1921). Let us recall Eq. (16), which represents the total energy of the system, minimized with respect to the displacement $\tilde{v}(\tilde{x})$. We observe that the last term of Eq. (16) represents the non-dimensional fracture energy

$$\tilde{\Gamma} = \frac{\xi}{2}, \tag{56}$$

while the first two terms represent the non-dimensional potential energy, namely

$$\tilde{\Pi} = -\frac{1}{2}\lambda^2 - \frac{1}{2}\frac{\lambda^2}{\nu^2}\xi\left[\nu^2 + \nu\xi\coth\left(\frac{1-\xi}{\nu}\right) + \frac{\xi^2}{3}\right]. \tag{57}$$

Then, being ξ the non-dimensional counterpart of the crack area, defined as $\xi = a/(Lb)$, where a is the actual fractured area, we evaluate the (non-dimensional) energy release rate $\tilde{G}$ as

$$\tilde{G} = -\frac{\partial\tilde{\Pi}}{\partial\xi} = \frac{\lambda^2}{2} + \frac{\lambda^2\xi}{\nu}\coth\left(\frac{1-\xi}{\nu}\right) + \frac{\lambda^2\xi^2}{2\nu^2}\coth^2\left(\frac{1-\xi}{\nu}\right) = \frac{\lambda^2}{2}\left[1 + \frac{\xi}{\nu}\coth\left(\frac{1-\xi}{\nu}\right)\right]^2. \tag{58}$$

Recalling that the critical stress $\lambda^{\mathcal{G}}_{cr}$, obtained through the Griffith energy criterion, is given by Eq. (30), we can write $\tilde{G}$ as

$$\tilde{G} = \frac{1}{2}\left(\frac{\lambda}{\lambda^{\mathcal{G}}_{cr}}\right)^2. \tag{59}$$

We can come back to quantities with real physical units through the relation $\xi = a/(Lb)$ and Eq. (8), and we obtain the energy release rate

$$G = -\frac{\partial\Pi}{\partial a} = -\frac{EY_M^2}{h}\frac{\partial\tilde{\Pi}}{\partial\xi} = \frac{EY_M^2}{h}\tilde{G} = \frac{EY_M^2}{2h}\frac{\sigma^2}{\sigma_{cr}^2}, \tag{60}$$

where $\sigma = EY_M\lambda/h$ and $\sigma_{cr} = EY_M\lambda_{cr}/h$. Similarly, we can deduce the fracture energy as

$$\Gamma = \frac{EY_M^2}{2h}a = \gamma_s(0)a \tag{61}$$

where we have introduced the fracture energy per unit surface for the purely mechanical system ($T = 0$)

$$\gamma_s(0) = \frac{EY_M^2}{2h}. \tag{62}$$

We can then reformulate Eq. (60) as

$$G = \gamma_s(0)\frac{\sigma^2}{\sigma_{cr}^2}. \tag{63}$$

We note that typically $\gamma_s(0)$ is linked with the "critical energy release rate" G_c through the relation $G_c = 2\gamma_s(0)$, where the multiplicative factor 2 is associated to the two free surfaces created by the propagating crack (top and bottom faces) so that the total fracture energy is multiplied by two. Since we are considering half of the system in our analysis (due to the symmetry of the

process we are describing, see Fig. 1d), the considered fracture energy density is two times the energy of the single face. Therefore, we obtain the relation $G_c = \gamma_s(0)$, and from Eq. (63) we get

$$\frac{G}{G_c} = \frac{\sigma^2}{\sigma_{cr}^2}. \tag{64}$$

We observe that this relation is consistent with classical results obtained by Griffith. In fact, the Griffith criterion predicts that $G = \pi\sigma^2 a/E$, and $G_c = \pi\sigma_{cr}^2 a/E$, and thus the relation $G/G_c = \sigma^2/\sigma_{cr}^2$ is proved. It is interesting to point out that in our model this relationship is valid as well. This shows that despite the geometric simplifications of our dissipative model the system is keeping the correct ratio between the involved (elastic and fracture) energies.

We can now apply the same reasoning for the full thermo-mechanical system, when thermal effects are considered. It should be noted that in this case, by using the Gibbs free energy in Eq. (46), the total energy (except for the fracture energy) is the sum of the potential energy in the mechanical limit given in Eq. (57) and the entropic term, eventually resulting in the following expression

$$\tilde{\Pi}^T = \tilde{\mathcal{G}}_0 + \frac{1}{2\tilde{\beta}} \ln\left[\sinh\left(\frac{1-\xi}{\nu}\right)\right] + \tilde{\Pi}. \tag{65}$$

Thus, recalling that the term $\tilde{\mathcal{G}}_0$ does not depend on ξ, and by using the result obtained in Eq. (59), the (non-dimensional, Gibbs) energy release rate in the thermo-mechanical system reads

$$\tilde{G}^T = -\frac{\partial\tilde{\Pi}^T}{\partial\xi} = \frac{\coth\left(\frac{1-\xi}{\nu}\right)}{2\nu\tilde{\beta}} + \frac{1}{2}\left(\frac{\lambda}{\lambda_{cr}^{\mathcal{G}}}\right)^2. \tag{66}$$

We can now use Eqs. (8), (35) and (62) to write

$$G^T = \gamma_s(0)\sqrt{\frac{E}{\mu}}\frac{L}{h}\frac{hk_bT}{ELbY_M^2}\coth\left(\frac{Lb-a}{bh}\sqrt{\frac{E}{\mu}}\right) + \gamma_s(0)\frac{\sigma^2}{\sigma_{cr}^2}. \tag{67}$$

We finally observe that, considering the result obtained for the critical temperature in Eq. (53), we can rewrite G^T as

$$G^T = \gamma_s(0)\frac{T}{T_c^{\mathcal{G}}} + \gamma_s(0)\frac{\sigma^2}{\sigma_{cr}^2} = \gamma_s(0)\left(\frac{\sigma^2}{\sigma_{cr}^2} + \frac{T}{T_c^{\mathcal{G}}}\right), \tag{68}$$

where it is important to remember that σ_{cr} is the Griffith critical stress at zero temperature. It means that $\sigma_{cr} = EY_M\lambda_{cr}/h$, where λ_{cr} is given in Eq. (30). It can be seen immediately that in our simplified model the energy release rate increases linearly with temperature. This result is in fairly good agreement with some experimental results (Wang et al., 2020; Belhouari et al., 2023). Since the critical energy release rate is given by $G_c^T = \gamma_s(0)$, the Griffith criterion for the crack propagation can be written as $G^T > \gamma_s(0)$. This exactly corresponds to $\sigma > \sigma_{cr}\sqrt{1 - T/T_c^{\mathcal{G}}}$, which is consistent with Eq. (54). Finally, the presence of a critical behavior described by a second-order phase transition is equivalent to a linear behavior of the energy release rate as a function of temperature, as stated in Eq. (68).

4.1. Temperature-dependent fracture surface energy

As anticipated in Section 4, $\gamma_s(0)$ defined in Eq. (62), represents the purely mechanical value of the fracture energy per unit surface at zero temperature. Based on previous results, we are able to determine the fracture surface energy $\gamma_s(T)$ at an arbitrary temperature. Observe that the dependence of the fracture surface energy on temperature is implicitly captured in Eq. (54), where the temperature-dependent critical load is expressed as the purely mechanical critical load multiplied by the entropic term $\sqrt{1 - T/T_c^{\mathcal{G}}}$. It is worth noting that, within the Griffith theory, the critical stress for fracture propagation is proportional to the square root of the surface energy $\sqrt{\gamma_s}$. This proportionality can be deduced also for the proposed model. Indeed, considering the critical load in Eq. (30) and the appropriate rescalings introduced in Eq. (8), we obtain

$$\sigma_{cr}(0) = \sqrt{\frac{2E}{h}}\lambda_{cr}^{\mathcal{G}}(0)\sqrt{\gamma_s(0)}. \tag{69}$$

Moreover, from Eq. (54), we deduce the similar relation

$$\sigma_{cr}(T) = \sqrt{\frac{2E}{h}}\lambda_{cr}^{\mathcal{G}}(T)\sqrt{\gamma_s(0)}. \tag{70}$$

Hence, since $\lambda_{cr}^{\mathcal{G}}(T) = \lambda_{cr}^{\mathcal{G}}(0)\sqrt{1 - \frac{T}{T_c^{\mathcal{G}}}}$, we can write $\sigma_{cr}(T) = \sqrt{\frac{2E}{h}}\lambda_{cr}^{\mathcal{G}}(0)\sqrt{\gamma_s(0)\left(1 - \frac{T}{T_c^{\mathcal{G}}}\right)}$, and we can identify the fracture surface energy as

$$\gamma_s(T) \sim \gamma_s(0)\left(1 - \frac{T}{T_c^{\mathcal{G}}}\right), \tag{71}$$

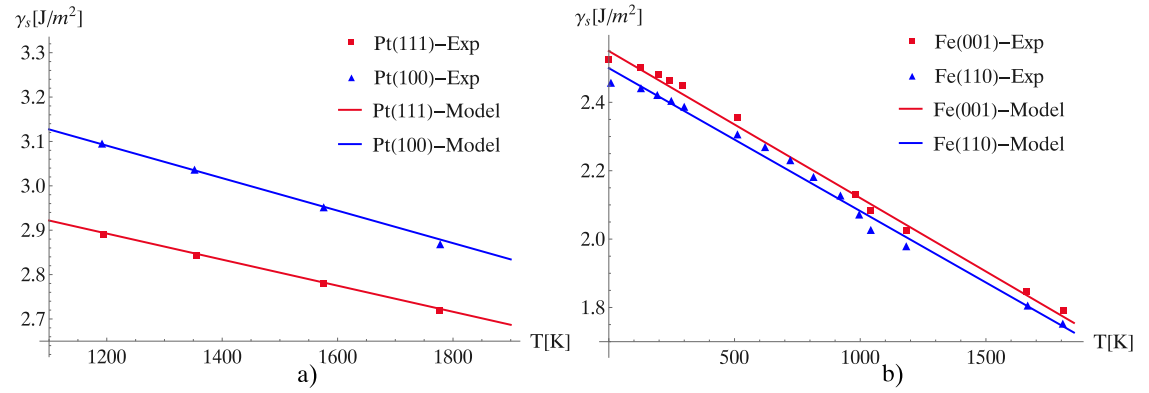

Fig. 10. Comparison of the temperature-dependent fracture surface energy $\gamma_s(T)$ obtained by the model described in the present paper, see Eq. (71), with experimental results on platinum and iron proposed by McLean and Mykura (1966) and Schönecker et al. (2015). Panel (a) shows results for fcc (111) and (100) facets of Pt, and panel (b) shows results for bcc (110) and (001) facets of Fe.

demonstrating that the proposed model is fully consistent with existing theoretical and experimental results in the literature, which recognize that surface energy decreases linearly with temperature (Kitamura, 2008; McLean and Mykura, 1966; Schönecker et al., 2015; Maksimov et al., 2001; Ramanaiah et al., 2015; Cheng et al., 2017; Kholtobina et al., 2023).

For instance, this equation aligns with the results obtained by Kitamura (2008), apart from the second-order term. Observe that the higher-order contribution in Kitamura's work arises from the nonlinearities of the system, whereas in our present model such effect is not observed, as the analysis is restricted to a linear force–extension behavior. Of course, the linear behavior of $\gamma_s(T)$ with temperature is valid only in a certain range that depends on the material, beyond which the behavior becomes more complex.

In Fig. 10, we compare the results obtained through Eq. (71) with experimental results concerning the fracture surface energy of platinum and iron proposed by McLean and Mykura (1966) and Schönecker et al. (2015), and we observe a quite good agreement.

4.2. Stress intensity factor

It is well known that the energy release rate G can be related to the stress intensity factor K by the expression (Irwin, 1957; Paris and Sih, 1965)

$$K = \sqrt{EG}, \tag{72}$$

where we considered the mode I of the fracture propagation. In particular, substituting Eq. (63) in Eq. (72), we obtain

$$K = \frac{\sigma}{\sigma_{cr}}\sqrt{E\gamma_s(0)}, \tag{73}$$

which is the stress intensity factor for a purely mechanical system, without thermal effects. Similarly, for the thermo-mechanical fracture process, using Eq. (68), we obtain

$$K^T = \sqrt{EG^T} = \frac{\sigma}{\sigma_{cr}}\sqrt{E\gamma_s(0)\left(\frac{\sigma_{cr}^2}{\sigma^2}\frac{T}{T_c^{\mathcal{G}}}+1\right)}, \tag{74}$$

where, as before, σ_{cr} is the Griffith critical stress at zero temperature. This result shows that the stress intensity factor grows proportionally to the root of temperature. It is worth noting that in this context the stress intensity factor is simply defined by Eq. (72) to be consistent with general fracture theory and can be used, for example, to reformulate the Griffith criterion in terms of this parameter. Nevertheless, in our model, the parameter itself does not describe the divergence of stress near the crack tip since the stress remains finite and regular everywhere in our structure.

4.3. J-Integral

Another application of the energy release rate concept for the crack propagation in the system under isotensional boundary condition consists in the calculation of the J-integral. We start by defining the "configurational force" (also referred to as "driving force") on a defect, first introduced by Eshelby (1951). He defined the "force acting on an elastic singularity" within a solid as the derivative of the energy with respect to the defect's displacement. Then, for a defect moving along the x-direction in a solid under tension, this force has been related to the Rice (1968) J-integral. Specifically Eshelby defined the "energy–momentum tensor" that, for the three-dimensional linear elasticity, reads

$$\mathbf{P} = \mathcal{W}\mathbf{I} - (\nabla\mathbf{u})^T\boldsymbol{\sigma}, \qquad P_{\ell j} = \mathcal{W}\delta_{\ell j} - \frac{\partial \mathcal{W}}{\partial u_{i,j}}u_{i,\ell} = \mathcal{W}\delta_{\ell j} - \sigma_{ij}u_{i,\ell}, \tag{75}$$

where $\mathcal{W}$ is the strain energy density, δ_{ij} is the Kronecker delta, u_i are the components of the elastic displacement vector, and σ_{ij} are the components of the stress tensor. Here, as usually, the subscripts following a comma mean partial differentiation. Then he found that the integral over a closed surface S of normal $\mathbf{n}$ of this tensor, namely

$$F_\ell = \int_S \mathbf{P}\cdot\mathbf{n}dS = \int_S \left(\mathcal{W}\delta_{\ell j} - \sigma_{ij}u_{i,\ell}\right) n_j dS, \tag{76}$$

vanishes for any closed surface free of defects, whereas F_ℓ measures exactly the configurations force if the surface contains a crack moving along the ℓ-direction. This is consistent with the Rice's development when ℓ coincides with the x-direction (Rice, 1968).

For our system, we consider the total potential energy (in the continuum limit), which consists of Eq. (17) without the fracture term

$$\Pi\left(v(x), v'(x)\right) = \int_0^L \left[\frac{Eb}{2h}\left(1-\chi(x)\right)v^2(x) + \frac{1}{2}\mu v'^2(x)bh - \sigma b v(x)\right] dx. \tag{77}$$

Then, we can define the potential energy density

$$\pi\left(v(x), v'(x)\right) = \frac{Eb}{2h}\left(1-\chi(x)\right)v^2(x) + \frac{1}{2}\mu bh v'^2(x) - \sigma b v(x). \tag{78}$$

We observe that such a potential energy density is defined by the two quantities introduced in Eq. (18). It means that it depends not only on the shear strain $v'(x)$, but also directly on the extensional field $v(x)$. In the classical Eshelby theory, the strain energy density $\mathcal{W}$ depends on the strain components $u_{i,j}$, but not on the displacement component u_i. Therefore, we cannot directly apply the Eshelby's theory in its classical form and we must apply the following alternative procedure. We first remember that the characteristic function χ distinguishes between intact and broken regions of the system. Equivalently, we can affirm that χ takes into account discontinuity in the stiffness of the system (being 0 in the broken region and 1 in the intact region). For the following calculations, we will consider explicitly the dependence of the stiffness of the system $\mathbb{C}$ on the position, and on the fracture extension within the system. We then define $\mathbb{C} = E$ in the intact region, and $\mathbb{C} = 0$ in the broken one. Then, the crack propagation is represented by

$$\mathbb{C}(x,\zeta) = E\left\{1 - \mathbf{1}\left[x - (L-\zeta)\right]\right\}, \tag{79}$$

where $0 \le x \le L$ is the position where we define the stiffness, and ζ is the crack extension corresponding to $\zeta = \xi L$, with $0 \le \xi \le 1$. Here, $\mathbf{1}(z)$ is the Heaviside step function, the value of which is zero for negative arguments and one for positive arguments. The crack nucleates to the left and moves to the right, as defined above, and thus we have the following two extreme cases. For $\zeta = 0$ (or $\xi = 0$), the system is fully intact and we have $\mathbb{C}(x,0) = E\left[1 - \mathbf{1}(x-L)\right]$, that is $\mathbb{C}(x,0) = E$ within the system. Similarly, for $\zeta = L$ (or $\xi = 1$), the system is fully broken and we have $\mathbb{C}(x,L) = E\left[1-\mathbf{1}(x)\right]$, that is $\mathbb{C}(x,L) = 0$ within the system. Using this notation, we rewrite the energy density of the system, given in Eq. (78), as

$$\pi\left(v(x), v'(x)\right) = \frac{b}{2h}\mathbb{C}(x,\zeta)v^2(x) + \frac{1}{2}\mu bh v'^2(x) - \sigma b v(x). \tag{80}$$

According to Eshelby, the configurational force acting on the crack is given by

$$F = -\frac{\partial\Pi\left(v, v'\right)}{\partial\zeta} = -\frac{\partial}{\partial\zeta}\left[\int_0^L \left(\frac{b}{2h}\mathbb{C}v^2 + \frac{1}{2}\mu bh v'^2 - \sigma b v\right) dx\right]. \tag{81}$$

Since both v and $\mathbb{C}$ depend on ζ, the differentiation provides

$$F = -\int_0^L \left(\frac{b}{2h}\frac{\partial\mathbb{C}}{\partial\zeta}v^2 + \frac{b}{h}\mathbb{C}v\frac{\partial v}{\partial\zeta} + \mu bh v'\frac{\partial v'}{\partial\zeta} - \sigma b\frac{\partial v}{\partial\zeta}\right) dx. \tag{82}$$

Here we have, with a little abuse, derived the function $\mathbb{C}$ as if it were regular, and we have clearly assumed that v depends on ζ since it is the solution of the problem with $\mathbb{C}$ (and thus ζ) fixed. The governing equation for v has been obtained in non-dimensional form in Eq. (23), and it is rewritten here in its dimensional form

$$\mu bh v'' - \frac{b}{h}\mathbb{C}v = -\sigma b, \tag{83}$$

which is associated with the boundary conditions $v'(0) = v'(L) = 0$. Now, we consider the configurational force in Eq. (82), and we substitute σ taken from Eq. (83). We get

$$\begin{aligned} F &= -\int_0^L \left(\frac{b}{2h}\frac{\partial\mathbb{C}}{\partial\zeta}v^2 + \frac{b}{h}\mathbb{C}v\frac{\partial v}{\partial\zeta} + \mu bh v'\frac{\partial v'}{\partial\zeta} + \mu bh v''\frac{\partial v}{\partial\zeta} - \frac{b}{h}\mathbb{C}v\frac{\partial v}{\partial\zeta}\right) dx \\ &= -\int_0^L \left[\frac{b}{2h}\frac{\partial\mathbb{C}}{\partial\zeta}v^2 + \mu bh\left(v'\frac{\partial v'}{\partial\zeta} + v''\frac{\partial v}{\partial\zeta}\right)\right] dx, \end{aligned} \tag{84}$$

and we observe that

$$\frac{\partial}{\partial x}\left(v'\frac{\partial v}{\partial\zeta}\right) = v''\frac{\partial v}{\partial\zeta} + v'\frac{\partial v'}{\partial\zeta}, \tag{85}$$

leading to

$$\int_0^L \frac{\partial}{\partial x}\left(v'\frac{\partial v}{\partial\zeta}\right) dx = 0, \tag{86}$$

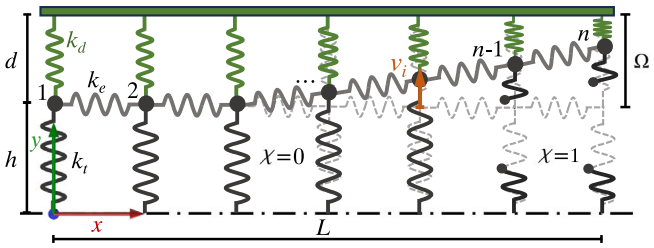

Fig. 11. Schematic representation of the hard device configuration: the material properties are mimicked by $n-1$ horizontal elastic springs of stiffness k_e, and by n vertical breakable units of stiffness k_t, describing the crack propagation. L is the total length of the system, and h is its height. We study the response of the system when is subjected to a prescribed displacement Ω, uniformly applied to all units by a device of length L and height d, modeled as a discrete sequence of linear elastic springs of stiffness k_d.

as we assume that the two ends of the system are free, that is $v'(0) = v'(L) = 0$. Hence, Eq. (84) becomes

$$F = -\int_0^L \frac{b}{2h}\frac{\partial \mathbb{C}}{\partial \zeta} v^2 dx. \tag{87}$$

We use now the form of the stiffness $\mathbb{C}$ defined in Eq. (79), and we obtain that $\frac{\partial \mathbb{C}}{\partial \zeta} = -E\delta[x-(L-\zeta)]$, where $\delta(z) = d\mathbf{1}(z)/dz$ represents the Dirac delta function. Thus, we obtain

$$F = \int_0^L \frac{Eb}{2h}\delta[x-(L-\zeta)]\, v^2(x)dx = \frac{Eb}{2h}v^2(L-\zeta). \tag{88}$$

This is the main result concerning the configurational force and the J-integral in our model. Substituting now the solution for the displacement obtained in Eq. (27), and using the rescaling $v = \tilde{v}Y_M$, it is easy to verify that

$$F = \frac{EY_M^2}{2h} b \frac{\sigma^2}{\sigma_{cr}^2} = \gamma_s(0)\frac{\sigma^2}{\sigma_{cr}^2} b, \tag{89}$$

which is consistent with the energy release obtained in Eq. (63), provided that we impose $G = F/b$. In fact, to obtain the configurational force we derived the energy with respect to the linear extent of the fracture ζ, and to obtain the energy release rate we derived with respect to the fracture surface a (being $b = a/\zeta$ their ratio).

To conclude, we can calculate the driving force for the crack propagation within the system with thermal effects. In this case, we have to include the entropic term in the total energy, as it was already done in Eq. (46). We get

$$\Pi^T(v, v', T) = \Pi - TS = \Pi(v, v') + \frac{k_b T}{2}\ln\left[\sinh\left(\frac{L-\zeta}{\sqrt{\frac{\mu}{E}}h}\right)\right], \tag{90}$$

where $\Pi(v, v')$ refers to the mechanical energy defined in Eq. (77). Following the same procedure previously developed, and using Eqs. (53) and (62), we determine the temperature-dependent driving force as follows

$$F^T = -\frac{\partial \Pi^T}{\partial \zeta} = \frac{Eb}{2h}v^2(L-\zeta) + \frac{k_B T}{2\sqrt{\frac{\mu}{E}}h}\coth\left(\frac{L-\zeta}{\sqrt{\frac{\mu}{E}}h}\right) = \gamma_s(0)\left(\frac{\sigma^2}{\sigma_{cr}^2} + \frac{T}{T_c^{\mathcal{G}}}\right)b, \tag{91}$$

which is in perfect agreement with Eq. (68), provided that we define $G^T = F^T/b$. To conclude, the result of the J-integral calculation obtained in Eq. (88) gives the correct results for the energy release rate in both the purely mechanical case and the case with thermal fluctuations.

5. Hard device (statistical Helmholtz ensemble)

While in the previous Section the fracture propagation was analyzed under an externally applied load (soft device), in this Section we delve into the study of a different type of external loading inducing crack propagation, *i.e.* the case when the total extension of the system is prescribed (hard device). Similarly to the approach used with the soft device configuration, we initially examine the purely mechanical model and subsequently we incorporate the influence of thermal fluctuations. We start by considering the mechanical model represented in Fig. 11. The geometric parameters are the same as those of the soft device configuration: L is the total length of the system along the x-axis, h is the height along the y-axis, and b is the (out of plane) depth along the z-axis. The external hard device is composed of a discrete sequence of linearly elastic springs of stiffness k_d, which impose a displacement Ω on the entire system. It should be noted that the springs, describing the traction device, were not considered in the case of the Gibbs

ensemble because with force applied these springs transmit the force unchanged and are therefore irrelevant to the behavior of the system. The geometrical parameters of the device are the length, equal to the system's length L along the x-direction and the height d along y-direction. The elastic energy describing the ith unit of the device is

$$T_i\left(v_i\right)=\frac{1}{2}k_d\left(\Omega-v_i\right)^2, \tag{92}$$

where Ω is the prescribed overall extension. By recalling Eqs. (3) and (4), the total mechanical energy of the system reads

$$\begin{aligned}\phi\left(\{v_i\},\{\chi_i\}\right)&=\sum_{i=1}^{n}U_i\left(\{v_i\},\{\chi_i\}\right)+\sum_{i=1}^{n-1}V_i\left(\{v_i\}\right)+\sum_{i=1}^{n}T_i\left(\{v_i\}\right)\\&=\frac{1}{2}k_t\sum_{i=1}^{n}\left[\left(1-\chi_i\right)v_i^2+\chi_i Y_M^2\right]+\frac{1}{2}k_e\sum_{i=1}^{n-1}\left(v_{i+1}-v_i\right)^2+\frac{1}{2}k_d\sum_{i=1}^{n}\left(\Omega-v_i\right)^2.\end{aligned} \tag{93}$$

Following the same methodology as the soft device configuration, we define the following material parameters

$$E=\frac{nk_t h}{bL},\qquad E_d=\frac{nk_d d}{bL},\qquad \mu=\frac{Lk_e}{nhb}, \tag{94}$$

where E is the material's Young modulus, E_d is the device's Young's modulus, and μ is the material's shear modulus. Moreover, we introduce the non-dimensional parameters $\tilde{v}_i$ (breakable units elongation), $\tilde{\Omega}$ (assigned displacement), $\tilde{\phi}$ (energy), ν^2 (reduce ratio between material's shear and Young moduli), ρ^2 (reduced ratio between device's and material's Young moduli) as follows

$$\tilde{v}_i=\frac{v_i}{Y_M},\quad \tilde{\Omega}=\frac{\Omega}{Y_M},\quad \tilde{\phi}=\frac{\phi h}{ELbY_M^2},\quad \nu^2=\frac{\mu h^2}{EL^2},\quad \rho^2=\frac{hE_d}{dE}=\frac{k_d}{k_t}, \tag{95}$$

in order to have the correct continuum rescaling. Hence, from Eq. (93), we can obtain the non-dimensional energy in the case of hard device

$$n\tilde{\phi}\left(\{\tilde{v}_i\},\{\chi_i\}\right)=\frac{1}{2}\sum_{i=1}^{n}\left[\left(1-\chi_i\right)\tilde{v}_i^2+\chi_i\right]+\frac{1}{2}n^2\nu^2\sum_{i=1}^{n-1}\left(\tilde{v}_{i+1}-\tilde{v}_i\right)^2+\frac{1}{2}\rho^2\sum_{i=1}^{n}\left(\tilde{\Omega}-\tilde{v}_i\right)^2. \tag{96}$$

As before, it is useful to rewrite the mechanical energy in Eq. (96), by using the matrix notation

$$n\tilde{\phi}\left(\tilde{\boldsymbol{v}},\chi\right)=\frac{1}{2}\mathbf{Q}\tilde{\boldsymbol{v}}\cdot\tilde{\boldsymbol{v}}+\frac{1}{2}\chi\cdot\mathbf{1}+\frac{1}{2}n\rho^2\tilde{\Omega}^2-\rho^2\tilde{\Omega}\tilde{\boldsymbol{v}}\cdot\mathbf{1}, \tag{97}$$

where the structure of $\tilde{\boldsymbol{v}}$, χ and $\mathbf{1}$ is defined in Eq. (12), and $\mathbf{Q}$ is a tridiagonal symmetric matrix defined as

$$\mathbf{Q}=n^2\nu^2\begin{bmatrix}\mathrm{Q}_1 & -1 & 0 & \dots & 0\\ -1 & \mathrm{Q}_2 & -1 & \ddots & \vdots\\ 0 & \ddots & \ddots & \ddots & 0\\ \vdots & \ddots & -1 & \mathrm{Q}_{n-1} & -1\\ 0 & \dots & 0 & -1 & \mathrm{Q}_n\end{bmatrix}. \tag{98}$$

Here, we introduced $\mathrm{Q}_i=(1-\chi_i+\rho^2)/(n^2\nu^2)+2$ for $i=2,\dots n-1$, and the first and last coefficients as it follows: $\mathrm{Q}_1=(1-\chi_1+\rho^2)/(n^2\nu^2)+1$, and $\mathrm{Q}_n=(1-\chi_n+\rho^2)/(n^2\nu^2)+1$.

5.1. Equilibrium configurations

As we have already done in the isotensional case, also for the isometric one we can find the equilibrium configurations for the purely mechanical system by minimizing the energy with respect to the displacement vector $\tilde{\boldsymbol{v}}$, considering a fixed number of broken units assigned by means of the vector χ. The equilibrium equations then read

$$\frac{\partial}{\partial\tilde{\boldsymbol{v}}}\left(n\tilde{\phi}\left(\tilde{\boldsymbol{v}},\chi\right)\right)=\mathbf{Q}\tilde{\boldsymbol{v}}-\rho^2\tilde{\Omega}\mathbf{1}=\mathbf{0}, \tag{99}$$

which can be solved eventually obtaining the displacement vector at equilibrium as

$$\tilde{\boldsymbol{v}}_e^{\mathcal{H}}=\rho^2\tilde{\Omega}\mathbf{Q}^{-1}\mathbf{1}. \tag{100}$$

So doing, the equilibrium energy assumes the value

$$n\tilde{\phi}\left(\tilde{\boldsymbol{v}}_e^{\mathcal{H}},\chi\right)=n\tilde{\phi}_e\left(\chi\right)=-\frac{1}{2}\rho^4\tilde{\Omega}^2\mathbf{Q}^{-1}\mathbf{1}\cdot\mathbf{1}+\frac{1}{2}\chi\cdot\mathbf{1}+\frac{1}{2}n\rho^2\tilde{\Omega}^2, \tag{101}$$

which describes the non-dimensional energy of the equilibrated system at prescribed displacement $\tilde{\Omega}$, and assigned fracture configuration χ. As before, we consider a fracture that nucleates to the right and propagates to the left, and is described by a number m of broken springs. This choice fully defines the vector χ.

In Fig. 12(a) we show the energy curves corresponding to a system composed by $n=20$ units, with a variable number m of broken springs: the thickest curve (left side) corresponds to the fully intact system ($m=0$), while the horizontal thick line (right side) describes the completely broken system ($m=20$). The thin curves represent all the intermediate possible configurations between

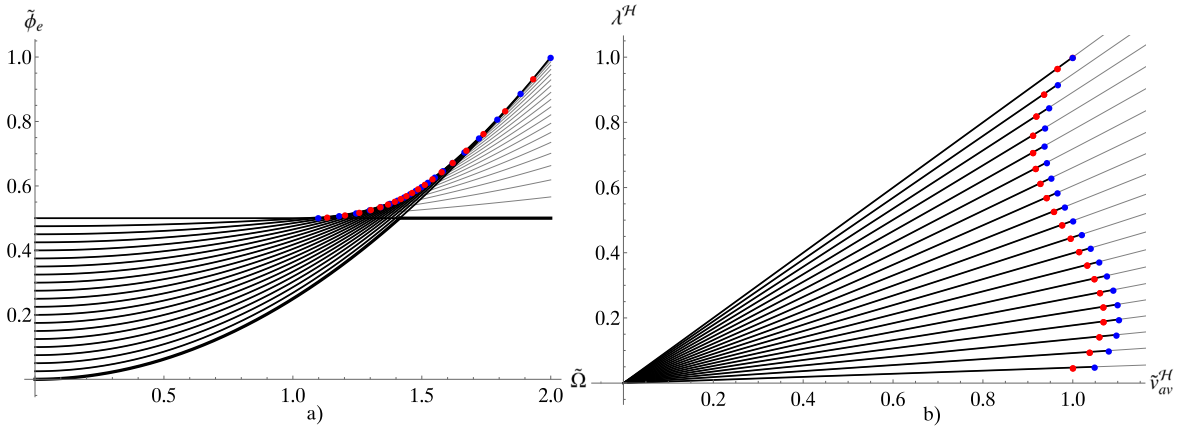

Fig. 12. Equilibrium configurations for a discrete system with $n = 20$ units, in hard device configuration. In both panels gray curves describe the system response with a fixed number of broken units m. In panel (a), we show the minimized energy $\tilde{\phi}_e$ as function of the imposed total displacement $\tilde{\Omega}$. The thickest curves indicate the energy global minima of the system, switching from fully intact to completely broken configurations. The blue points indicate the critical threshold value of $\tilde{\Omega}$, represented by the condition $\tilde{v}_{n-m} = 1$. The red points describe the situation where the energy of the system with m broken units equals the energy of the system with $m + 1$ broken units (Griffith threshold). In panel (b), we show the force–displacement relations. Each straight line corresponds to a different value of m, and the red and blue points are defined as in the panel (a). The parameters used in this diagram are $\nu = 0.5$ and $\rho = 1$.

fully intact and fully broken states, characterized by an increasing value of m. It is interesting to note in Fig. 12(a) that the global minima of the energy for the system in the hard device configuration are represented by the thickest curves, exploring the fully intact system (represented by the bottom curve on the left side of the plot) and the completely broken configuration (horizontal line on the right side), without passing through intermediate configurations. However, according with the Griffith approach, we deduce the fracture strategy by comparing the local energy minima of two adjacent configurations (with m and $m + 1$ broken springs), corresponding to the crack propagation. Moreover, as in the case of soft device configuration, we indicate with the blue points the critical threshold represented by the condition $\tilde{v}_{n-m} = 1$, and with the red points the situation where the energy of the system with m broken units equals the energy of the system with $m + 1$ broken units. Thus representing a discrete version of the Griffith propagation threshold. Observe that, as in the case with a soft device, that as n increases, the red points converge to blue points. This is in particular the case of the continuum Γ-limit analyzed in the following.

In Fig. 12(b), we show the curves representing the relation between the force λ and the average displacement $\tilde{v}_{av}$, for a system composed of $n = 20$ units, with a varying number of broken units m. Specifically, each curve represents the system's response for a given number of broken units m, with the upper curve representing the system with $m = 0$, and the curve parallel to the x-axis describing the case with $m = 20$. The decrease in slope as fracture extension increases represents the progressive decrease in stiffness. The force–displacement relation is obtained by defining the non-dimensional stress as

$$n\lambda^{\mathcal{H}} = \frac{\partial}{\partial\tilde{\Omega}}\left(n\tilde{\phi}(\tilde{\boldsymbol{v}}_e^{\mathcal{H}}, \chi)\right) = n\rho^2\tilde{\Omega} - \rho^4\tilde{\Omega}\,\mathbf{Q}^{-1}\mathbf{1}\cdot\mathbf{1}, \tag{102}$$

and the average displacement as

$$\tilde{v}_{av}^{\mathcal{H}} = \frac{1}{n}\tilde{\boldsymbol{v}}_e^{\mathcal{H}}\cdot\mathbf{1} = \frac{1}{n}\rho^2\tilde{\Omega}\,\mathbf{Q}^{-1}\mathbf{1}\cdot\mathbf{1}, \tag{103}$$

which represent the mean value of the displacements at equilibrium of all the units in the system for a given m, and assigned displacement Ω. These values would be particularly representative in a multiscale approach when the proposed model represents the process zone of fracture propagation. Therefore, the force–extension relations are given by

$$\lambda^{\mathcal{H}} = \left(\frac{n}{\mathbf{Q}^{-1}\mathbf{1}\cdot\mathbf{1}} - \rho^2\right)\tilde{v}_{av}^{\mathcal{H}}. \tag{104}$$

These straight lines are plotted in Fig. 12(b), together with the red and blue points, defined shortly above. One moves on each straight line by varying the value of the total extension Ω, and then reaches such limit points representing the fracture state existence threshold (blue) and Griffith's threshold describing propagation (red), respectively. As we have seen before for the isotensional case, and as we will also demonstrate shortly for the isometric case, red points tend to the blue ones in the continuous limit that is, for $n \to \infty$. Also we point out again that the existence thresholds (blue dots) are not considered in the classical Griffith approach.

5.2. Continuum limit

To study the behavior of the system in the continuum limit, we can proceed with two different but equivalent approaches, as demonstrated for the soft device configuration. In the first approach, we start from the minimized energy given in Eq. (101), and we analyze the limit for $n \to \infty$. In that case, the detailed calculations were provided in Appendix. In the second approach, we consider

the continuum limit of the non-minimized energy given in Eq. (96), and we apply the energy minimization through a variational method. Since the equivalence of the two procedures has been demonstrated with the isotensional configuration, in the present isometric case, for the sake of brevity, we perform only the variational procedure, which is simpler. By using the same notation introduced in Eq. (17), we can write the functional representing the total mechanical energy under isometric condition as

$$\phi\left(v,v'\right)=\int_0^L\left[\frac{1}{2}E\left(\frac{v^2}{h^2}\left(1-\chi(x)\right)+\chi(x)\frac{Y_M^2}{h^2}\right)bh+\frac{1}{2}\mu v'^2(x)bh+\frac{1}{2}E_d\frac{\left(\Omega-v(x)\right)^2}{d^2}bd\right]dx, \tag{105}$$

which corresponds to the discrete version given in Eq. (96). For the continuum description, as before, the extensional and the shear strains of the system are defined in Eq. (18) and the shear force is given in Eq. (19). For the hard device configuration we also define the device extensional strain

$$\epsilon_d(x)=\frac{\Omega-v(x)}{d}. \tag{106}$$

We rewrite the total energy in the non-dimensional form, rescaling x as $\tilde{x}=x/L$, with $\tilde{x}\in[0,1]$, and introducing once again the non-dimensional quantities

$$\tilde{v}=\frac{v}{Y_M},\quad \tilde{\Omega}=\frac{\Omega}{Y_M},\quad \tilde{\phi}=\frac{\phi h}{ELbY_M^2},\quad \nu^2=\frac{\mu h^2}{EL^2},\quad \rho^2=\frac{hE_d}{dE}. \tag{107}$$

Straightforward calculations deliver

$$\tilde{\phi}(\tilde{v},\tilde{v}')=\int_0^1\left[\frac{1}{2}\left(1-\chi(\tilde{x})\right)\tilde{v}^2(\tilde{x})+\frac{1}{2}\chi(\tilde{x})+\frac{1}{2}\nu^2\tilde{v}'^2(\tilde{x})+\frac{1}{2}\rho^2\left(\tilde{\Omega}-\tilde{v}(\tilde{x})\right)^2\right]d\tilde{x}. \tag{108}$$

In order to find the equilibrium configurations, we look for the extremals of the functional $\tilde{\phi}$. Therefore, once the Lagrangian density ς is defined as

$$\varsigma(\tilde{v},\tilde{v}')=\frac{1}{2}\left(1-\chi(\tilde{x})\right)\tilde{v}^2(\tilde{x})+\frac{1}{2}\chi(\tilde{x})+\frac{1}{2}\nu^2\tilde{v}'^2(\tilde{x})+\frac{1}{2}\rho^2\left(\tilde{\Omega}-\tilde{v}(\tilde{x})\right)^2, \tag{109}$$

we study the Euler–Lagrange equation

$$\frac{d}{dx}\frac{\partial}{\partial\tilde{v}'}\varsigma(\tilde{v},\tilde{v}')-\frac{\partial}{\partial\tilde{v}}\varsigma(\tilde{v},\tilde{v}')=0, \tag{110}$$

which leads to

$$\nu^2\tilde{v}''(\tilde{x})-\left(1-\chi(\tilde{x})+\rho^2\right)\tilde{v}(\tilde{x})=-\rho^2\tilde{\Omega}. \tag{111}$$

As before, we study the case of a single domain wall separating the intact region $\tilde{x}\in(0,1-\xi)$ from the broken region $\tilde{x}\in(1-\xi,1)$. The solutions for the displacement $\tilde{v}$ in the intact region ($\chi=0$), and in the broken region ($\chi=1$), can be analytically obtained by solving the elastica equations as

$$\begin{aligned}\tilde{v}_I^{\mathcal{H}}(\tilde{x})&=A\exp\left[-\sqrt{\frac{1+\rho^2}{\nu^2}}\tilde{x}\right]+B\exp\left[\sqrt{\frac{1+\rho^2}{\nu^2}}\tilde{x}\right]+\frac{\rho^2}{1+\rho^2}\tilde{\Omega},\\ \tilde{v}_B^{\mathcal{H}}(\tilde{x})&=C\exp\left[\frac{\rho}{\nu}\tilde{x}\right]+D\exp\left[-\frac{\rho}{\nu}\tilde{x}\right]+\tilde{\Omega}.\end{aligned} \tag{112}$$

The four constants A,B,C,D can be evaluated by imposing that there are no applied shear forces at the two ends of the system, and that both the force and the displacement are continuous in the point representing the fracture propagation front (domain wall at $\tilde{x}=1-\xi$). These boundary conditions can be summed up by the following system of equations

$$\begin{cases}\tilde{v}_I'^{\mathcal{H}}(0)=0,\\ \tilde{v}_B'^{\mathcal{H}}(1)=0,\\ \tilde{v}_I'^{\mathcal{H}}(1-\xi)=\tilde{v}_B'^{\mathcal{H}}(1-\xi),\\ \tilde{v}_I^{\mathcal{H}}(1-\xi)=\tilde{v}_B^{\mathcal{H}}(1-\xi).\end{cases} \tag{113}$$

Its solution allows us to determine the displacement field in the intact and broken regions of the system as

$$\begin{aligned}\tilde{v}_I^{\mathcal{H}}(\tilde{x})&=\frac{\tilde{\Omega}}{1+\rho^2}\left[\frac{\rho}{Y(\xi)}\sinh\left(\frac{\rho\xi}{\nu}\right)\cosh\left(\sqrt{\frac{1+\rho^2}{\nu^2}}\tilde{x}\right)+\rho^2\right],\\ \tilde{v}_B^{\mathcal{H}}(\tilde{x})&=\tilde{\Omega}-\frac{\tilde{\Omega}}{Y(\xi)\sqrt{1+\rho^2}}\sinh\left(\sqrt{\frac{1+\rho^2}{\nu^2}}(1-\xi)\right)\cosh\left[\frac{\rho}{\nu}(1-\tilde{x})\right],\end{aligned} \tag{114}$$

where $Y(\xi)$ is given by

$$Y(\xi)=\rho\sinh\left(\frac{\rho\xi}{\nu}\right)\cosh\left(\sqrt{\frac{1+\rho^2}{\nu^2}}(1-\xi)\right)+\sqrt{1+\rho^2}\cosh\left(\frac{\rho\xi}{\nu}\right)\sinh\left(\sqrt{\frac{1+\rho^2}{\nu^2}}(1-\xi)\right). \tag{115}$$

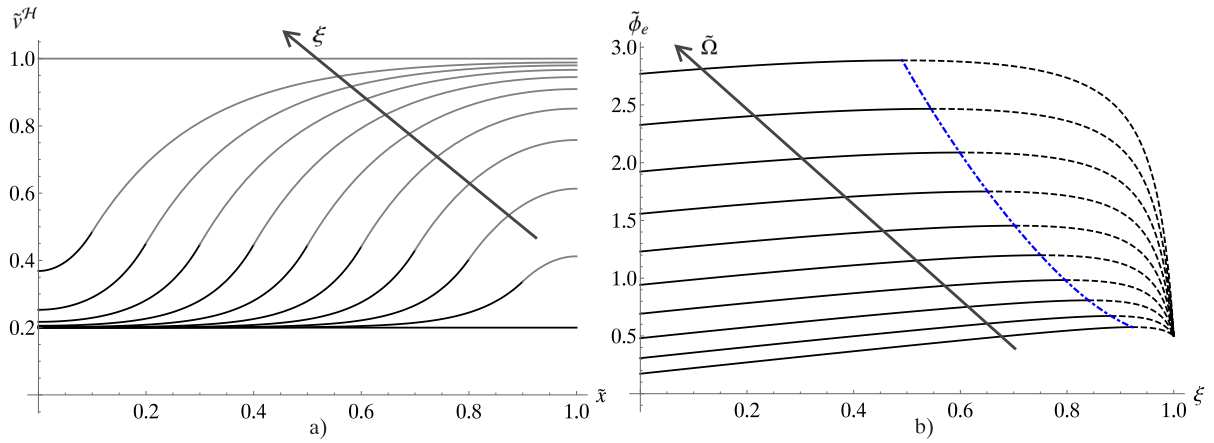

Fig. 13. Equilibrium solutions for the continuum system within the hard device configuration. In panel (a), we show the displacement field for different values of ξ. Black lines describe the displacement $\tilde{v}_I^{\mathcal{H}}$ in the intact region, and gray lines represent $\tilde{v}_B^{\mathcal{H}}$ in the broken region. We used the parameters $\nu = 0.1$, $\rho = 0.5$ and $\tilde{\Omega} = 1$. In panel (b), we represent the minimized energy versus detached extension ξ, for different values of $\tilde{\Omega}$. The blue dashed curve passes through the points of maximum energy. For this diagrams the values $\nu = 0.5$, $\rho = 0.2$ and $\tilde{\Omega} \in [3, 12]$ have been used.

In Fig. 13(a), we deliver a graphical representation of the displacement field $\tilde{v}(\tilde{x})$, obtained at the equilibrium for different values of ξ. Thick and thin lines distinguish the intact area from the broken area. Moreover, by substituting $\tilde{v}_I^{\mathcal{H}}(\tilde{x})$ and $\tilde{v}_B^{\mathcal{H}}(\tilde{x})$ in the total energy stated in Eq. (108), we obtain the final expression for the energy minimized with respect to the displacement $\tilde{v}$, for the system with prescribed extension $\tilde{\Omega}$, and assigned broken portion ξ. The result is

$$\begin{aligned}\tilde{\phi}_e(\xi) &= \frac{1}{2}\xi + \frac{1}{2}\tilde{\Omega}^2 \frac{\rho^2}{1+\rho^2}(1-\xi) + \frac{1}{2}\tilde{\Omega}^2 \frac{\rho\nu}{\Upsilon(\xi)(1+\rho^2)\sqrt{1+\rho^2}} \sinh\left(\frac{\rho\xi}{\nu}\right) \sinh\left(\sqrt{\frac{1+\rho^2}{\nu^2}}(1-\xi)\right) \\ &= \frac{1}{2}\xi + \frac{1}{2}\tilde{\Omega}^2 \frac{\rho^2}{1+\rho^2}(1-\xi) + \frac{1}{2}\tilde{\Omega}^2 \frac{\rho\nu}{(1+\rho^2)\sqrt{1+\rho^2}} \frac{1}{\sqrt{1+\rho^2}\coth\left(\frac{\rho\xi}{\nu}\right) + \rho\coth\left(\sqrt{\frac{1+\rho^2}{\nu^2}}(1-\xi)\right)}.\end{aligned} \tag{116}$$

In Fig. 13(b), we observe the evolution of the energy $\tilde{\phi}_e$ with respect to the extension ξ of the broken region of the system, for different values of the prescribed overall displacement $\tilde{\Omega}$. In particular, we observe the influence of $\tilde{\Omega}$ on the fracture propagation, noting that as $\tilde{\Omega}$ increases, the maximum of the energy function shifts toward lower values of ξ. This means that as the imposed displacement increases, smaller cracks are stable, in agreement with Griffith's criterion (see below for quantitative details). Such a behavior is similar to what has already been observed for the soft device case in Fig. 7(a). However, we can point out a difference between soft and hard device behaviors. In the case of soft device, the total energy decreases with applied load, while in the case of hard device, the total energy increases with prescribed displacement. This is due to the fact that in the case with soft device the total energy also includes the energy associated to external forces that, being negative for positive forces, tends to reduce the value of the total energy. In the case of hard device, conversely, there are no energy terms due to the applied load. From the thermodynamic point of view, this means that we use the enthalpy function within the Gibbs ensemble and the internal energy within the Helmholtz ensemble.

5.3. Griffith energy criterion for fracture propagation

In this Section, we examine the propagation of an existing crack of extension ξ under isometric condition. The propagation is induced by the variable displacement $\tilde{\Omega}$, applied to the system by an hard device. More specifically, as in the case of a system subjected to a mechanical load, we apply the Griffith's energy criterion. Hence, the condition for having the crack propagation can be written as

$$\frac{\partial \tilde{\phi}_e(\xi)}{\partial \xi} < 0. \tag{117}$$

By evaluating the derivative of the energy with respect to the crack extension, we can rewrite the propagation Griffith's condition as

$$\frac{\tilde{\Omega}^2\rho^2}{1+\rho^2}\left[\frac{\Delta(\xi)}{\Upsilon(\xi)}\right]^2 > 1, \tag{118}$$

where we have defined the function $\Delta(\xi)$, as follows

$$\Delta(\xi) = \rho \cosh\left(\frac{\rho\xi}{\nu}\right) \sinh\left(\sqrt{\frac{1+\rho^2}{\nu^2}}(1-\xi)\right) + \sqrt{1+\rho^2} \sinh\left(\frac{\rho\xi}{\nu}\right) \cosh\left(\sqrt{\frac{1+\rho^2}{\nu^2}}(1-\xi)\right), \tag{119}$$

while $Y(\xi)$ is defined in Eq. (115). From Eq. (118), we deduce the equivalent inequality

$$\tilde{\Omega} > \frac{\sqrt{1+\rho^2}}{\rho} \frac{Y(\xi)}{\Delta(\xi)}. \tag{120}$$

Therefore, we can define the following critical threshold $\tilde{\Omega}_{cr}$ of the prescribed displacement, which generates propagation

$$\begin{aligned} \tilde{\Omega}_{cr} &= \frac{\sqrt{1+\rho^2}}{\rho} \frac{Y(\xi)}{\Delta(\xi)} = 1 + \frac{\cosh\left(\frac{\rho\xi}{\nu}\right) \sinh\left(\sqrt{\frac{1+\rho^2}{\nu^2}}(1-\xi)\right)}{\rho\Delta(\xi)} \\ &= 1 + \frac{\coth\left(\frac{\rho\xi}{\nu}\right)}{\rho^2 \coth\left(\frac{\rho\xi}{\nu}\right) + \rho\sqrt{1+\rho^2} \coth\left(\sqrt{\frac{1+\rho^2}{\nu^2}}(1-\xi)\right)}. \end{aligned} \tag{121}$$

In Fig. 14(a) and (b), we show how the critical value $\tilde{\Omega}_{cr}$ decreases as the broken extension of the system ξ increases, by considering different values of the parameters ν and ρ. This trend is fully consistent with the behavior shown in Fig. 13(b). Furthermore, in Fig. 14(c) and (d), it is possible to observe the critical stress $\lambda^{\mathcal{H}}_{cr}$ corresponding to $\tilde{\Omega}_{cr}$, defined as follows

$$\begin{aligned} \lambda^{\mathcal{H}}_{cr} &= \frac{\partial \tilde{\phi}_e}{\partial \tilde{\Omega}}\bigg|_{\tilde{\Omega}=\tilde{\Omega}_{cr}} = \frac{\rho\tilde{\Omega}}{1+\rho^2} \left[\rho(1-\xi) + \frac{\nu}{\sqrt{1+\rho^2}Y(\xi)} \sinh\left(\frac{\rho\xi}{\nu}\right) \sinh\left(\sqrt{\frac{1+\rho^2}{\nu^2}}(1-\xi)\right)\right]_{\tilde{\Omega}=\tilde{\Omega}_{cr}} \\ &= \frac{Y(\xi)}{\Delta(\xi)} \frac{1}{\sqrt{1+\rho^2}} \left[\rho(1-\xi) + \frac{\nu}{\sqrt{1+\rho^2}Y(\xi)} \sinh\left(\frac{\rho\xi}{\nu}\right) \sinh\left(\sqrt{\frac{1+\rho^2}{\nu^2}}(1-\xi)\right)\right]. \end{aligned} \tag{122}$$

This quantity is plotted versus ξ and parameterized with respect to both coefficients ν and ρ. We observe that also the quantity $\lambda^{\mathcal{H}}_{cr}$ decreases with increasing ξ. Particularly noteworthy is the fact that the curves in Fig. 14(c) are obtained by varying ν and maintaining a very low value of ρ. This describes the response of a system where the stiffness of the device is significantly lower than the one of the system itself. Consequently, it can be inferred that in this case, the response converges to that of the system in the soft device configuration (Florio et al., 2024). This is confirmed by comparing Fig. 14(c) with Fig. 7(b). To conclude, we observe that the displacement $\tilde{v}_{cr}$, corresponding to $\tilde{\Omega} = \tilde{\Omega}_{cr}$, and calculated at the fracture propagation front $\tilde{x} = 1-\xi$, is identically equal to the critical threshold 1 (or Y_M with dimensional quantities). It is possible to prove this result by evaluating Eq. (114) for $\tilde{x} = 1-\xi$ and $\tilde{\Omega} = \tilde{\Omega}_{cr}$, as follows

$$\tilde{v}^{\mathcal{H}}_B(1-\xi) = \tilde{\Omega}_{cr} - \frac{\tilde{\Omega}_{cr}}{Y(\xi)\sqrt{1+\rho^2}} \sinh\left(\sqrt{\frac{1+\rho^2}{\nu^2}}(1-\xi)\right) \cosh\left(\frac{\rho\xi}{\nu}\right). \tag{123}$$

Substituting $\tilde{\Omega}_{cr}$ from Eq. (121) into Eq. (123), we obtain

$$\tilde{v}^{\mathcal{H}}_B(1-\xi) = \frac{Y(\xi)\sqrt{1+\rho^2}}{\rho\Delta(\xi)} - \frac{1}{\rho\Delta(\xi)} \sinh\left(\sqrt{\frac{1+\rho^2}{\nu^2}}(1-\xi)\right) \cosh\left(\frac{\rho\xi}{\nu}\right), \tag{124}$$

and, by using the definitions of $Y(\xi)$ and $\Delta(\xi)$ in Eqs. (115) and (119), respectively, we can easily demonstrate that $\tilde{v}^{\mathcal{H}}_B(1-\xi) = 1$. This means that, also in the case with hard device, Griffith's threshold coincides with the existence threshold of any equilibrium solution at ξ fixed. And therefore, we have rigorously proved that the red points in Fig. 12 converge to the blue points in the continuum limit.

5.4. Temperature effects within the Helmholtz ensemble

In this Section, we introduce the effect of thermal fluctuations on breakable systems under isometric boundary conditions. As before, we study the system at thermodynamic equilibrium, in contact with a thermal bath at temperature T. The isometric condition corresponds to the Helmholtz ensemble in the statistical mechanics framework. Therefore, we consider the energy ϕ of the discrete system stated in Eq. (93), where we have prescribed the total extension Ω of the system. Based on these premises, we evaluate the Helmholtz partition function

$$\mathcal{Z}^{\mathcal{H}}(\chi, T) = \int_{\mathbf{R}^n} \exp\left[-\frac{\phi(\boldsymbol{v}, \chi)}{k_B T}\right] d\boldsymbol{v}, \tag{125}$$

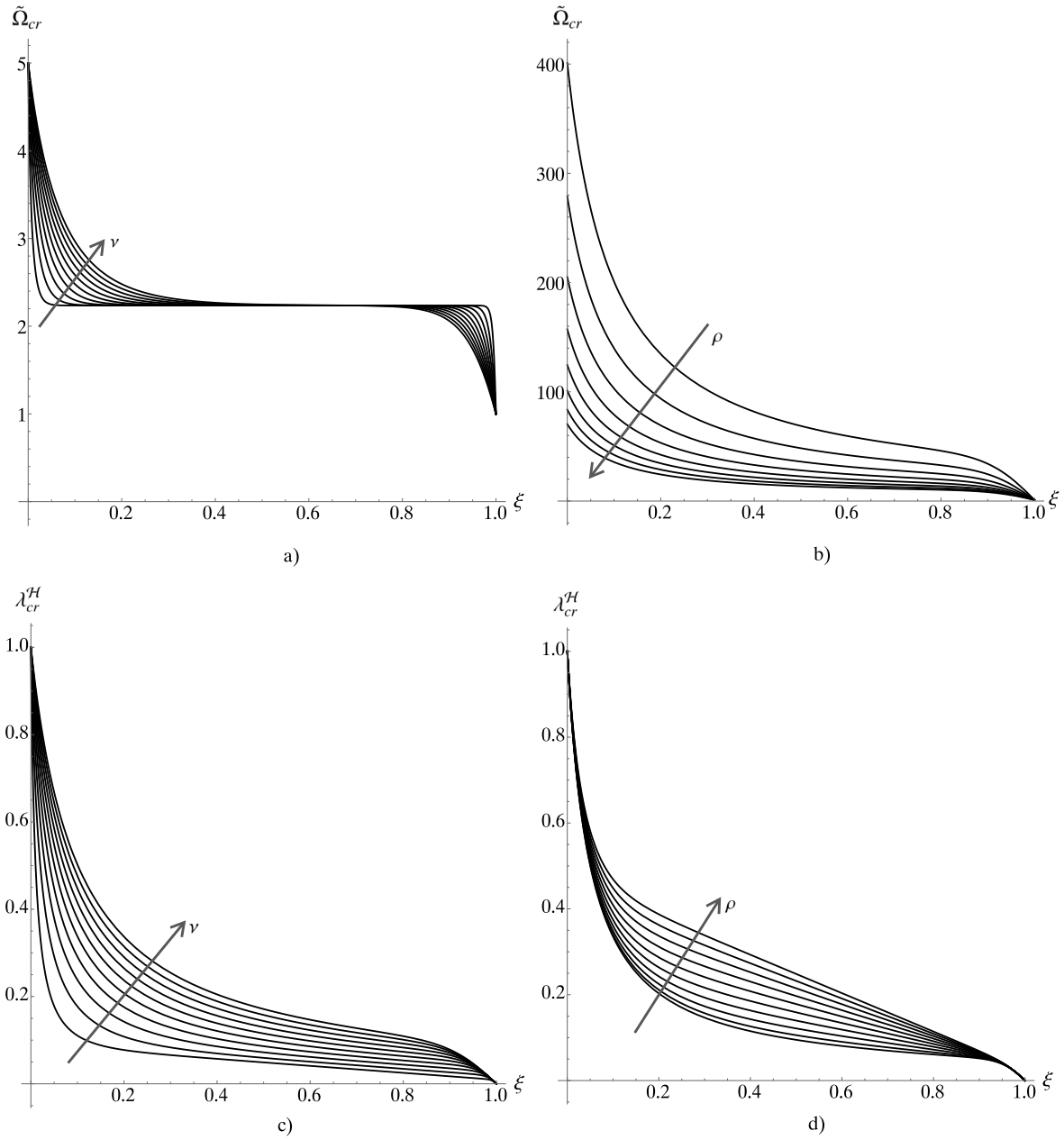

Fig. 14. In panels (a) and (b), we show the critical displacement, required for fracture propagation according to the Griffith energy criterion, versus ξ, and for different values of the parameters ν and ρ: in both cases, $\tilde{\Omega}_{cr}$ decreases as the system progressively breaks. In panel (a), we assigned $\rho = 0.5$, and the curves are obtained for $\nu \in [0.01, 0.1]$. In panel (b), we used $\nu = 0.2$, and $\rho \in [0.05, 0.12]$. In panels (c) and (d), we show the behavior of the critical load corresponding to $\tilde{\Omega}_{cr}$, obtained through Eq. (122). In panel (c), we adopted $\rho = 0.08$, and $\nu \in [0.01, 0.1]$, while in panel (d), we assigned $\nu = 0.05$, and $\rho \in [0.05, 0.5]$.

where k_B is the Boltzmann constant, $\boldsymbol{v} = \{v_1, v_2, \dots v_n\}$ and $\boldsymbol{\chi} = \{\chi_1, \chi_2, \dots \chi_n\}$. To simplify the calculations, we substitute ϕ with the non-dimensional counterpart $\tilde{\phi}$, defined in Eq. (107), and $\boldsymbol{v}$ with $\tilde{\boldsymbol{v}} = \boldsymbol{v}/Y_M$, eventually obtaining

$$\mathcal{Z}^{\mathcal{H}}(\boldsymbol{\chi}, T) = \left(Y_M\right)^n \int_{\mathbf{R}^n} \exp\left[-\tilde{\beta}\tilde{\phi}(\tilde{\boldsymbol{v}}, \boldsymbol{\chi})\right] d\tilde{\boldsymbol{v}}, \tag{126}$$

where the non-dimensional parameter $\tilde{\beta}$ is defined in Eq. (35). By substituting Eq. (97) in Eq. (126), we can write

$$\begin{aligned}\mathcal{Z}^{\mathcal{H}}(\chi,T) &= \left(Y_M\right)^n \int_{\mathbf{R}^n} \exp\left[-\frac{\tilde{\beta}}{n}\left(\frac{1}{2}\boldsymbol{Q}\tilde{\boldsymbol{v}}\cdot\tilde{\boldsymbol{v}} + \frac{1}{2}\chi\cdot\mathbf{1} + \frac{1}{2}n\rho^2\tilde{\Omega}^2 - \rho^2\tilde{\Omega}\tilde{\boldsymbol{v}}\cdot\mathbf{1}\right)\right] d\tilde{\boldsymbol{v}} \\ &= \left(Y_M\right)^n \exp\left[-\frac{\tilde{\beta}}{2n}\left(\chi\cdot\mathbf{1} + n\rho^2\tilde{\Omega}^2\right)\right] \int_{\mathbf{R}^n} \exp\left[-\frac{\tilde{\beta}}{n}\left(\frac{1}{2}\boldsymbol{Q}\tilde{\boldsymbol{v}}\cdot\tilde{\boldsymbol{v}} - \rho^2\tilde{\Omega}\tilde{\boldsymbol{v}}\cdot\mathbf{1}\right)\right] d\tilde{\boldsymbol{v}}.\end{aligned} \tag{127}$$

As already done within the Gibbs ensemble, the integration can be performed through the classical Gaussian property stated in Eq. (37), and recalling the expression for the minimized energy in Eq. (101), we get

$$\begin{aligned}\mathcal{Z}^{\mathcal{H}}(\chi,T) &= \left(Y_M\right)^n \sqrt{\frac{(2\pi n)^n}{\tilde{\beta}^n \det \boldsymbol{Q}}} \exp\left[-\frac{\tilde{\beta}}{n}\left(-\frac{1}{2}\rho^4\tilde{\Omega}^2\boldsymbol{Q}^{-1}\mathbf{1}\cdot\mathbf{1} + \frac{1}{2}\chi\cdot\mathbf{1} + \frac{1}{2}n\rho^2\tilde{\Omega}^2\right)\right] \\ &= \left(Y_M\right)^n \sqrt{\frac{(2\pi n)^n}{\tilde{\beta}^n \det \boldsymbol{Q}}} \exp\left[-\tilde{\beta}\tilde{\phi}_e(\chi)\right].\end{aligned} \tag{128}$$

In the limit for $n \to \infty$, the energy $\tilde{\phi}_e(\chi)$ in Eq. (128) can be substituted with the explicit expression for $\tilde{\phi}_e(\xi)$, obtained in Eq. (116). Moreover, following the same method shown in Appendix for the Gibbs ensemble, it is possible to calculate the asymptotic behavior of $\det \boldsymbol{Q}$ as $n \to \infty$ that gives

$$\det \boldsymbol{Q} = \frac{\left(n^2\nu^2\right)^n}{n\nu} Y(\xi), \tag{129}$$

where $Y(\xi)$ is defined in Eq. (115). Therefore, the partition function for large values of n, in the Helmholtz ensemble, is given by

$$\mathcal{Z}^{\mathcal{H}}(\xi,T) = \left(Y_M\right)^n \sqrt{\frac{(2\pi n)^n n\nu}{\tilde{\beta}^n \left(n^2\nu^2\right)^n Y(\xi)}} \exp\left[-\tilde{\beta}\tilde{\phi}_e(\xi)\right]. \tag{130}$$

We can now calculate the Helmholtz free energy as follows (Manca et al., 2012; Gibbs, 1902; Weiner, 1983)

$$\mathcal{F}(\xi,T) = -k_B T \ln\left(\mathcal{Z}^{\mathcal{H}}(\xi,T)\right). \tag{131}$$

As already done within the Gibbs ensemble, we adopt its non-dimensional version

$$\tilde{\mathcal{F}}(\xi,T) = \frac{h}{ELbY_M^2}\mathcal{F}(\xi,T) = -\frac{hk_B T}{ELbY_M^2}\ln\left(\mathcal{Z}^{\mathcal{H}}(\xi,T)\right) = -\frac{1}{\tilde{\beta}}\ln\left(\mathcal{Z}^{\mathcal{H}}(\xi,T)\right), \tag{132}$$

where we used the non-dimensional parameters introduced in Eq. (107), and $\tilde{\beta}$ defined in Eq. (35). Therefore, we can evaluate $\ln\left(\mathcal{Z}^{\mathcal{H}}(\xi,T)\right)$ as follows

$$\ln\left(\mathcal{Z}^{\mathcal{H}}(\xi,T)\right) = \ln c - \frac{1}{2}\ln Y(\xi) - \tilde{\beta}\tilde{\phi}_e(\xi), \tag{133}$$

where the constant c is defined below

$$c = \left(Y_M\right)^n \sqrt{\frac{(2\pi n)^n n\nu}{\tilde{\beta}^n \left(n^2\nu^2\right)^n}}. \tag{134}$$

We can finally write the non-dimensional Helmholtz free energy in the form

$$\tilde{\mathcal{F}}(\xi,T) = \tilde{\mathcal{F}}_0 + \frac{1}{2\tilde{\beta}}\ln Y(\xi) + \tilde{\phi}_e(\xi), \tag{135}$$

where $\tilde{\mathcal{F}}_0$ takes into account the non-influential multiplicative constant c in front of the partition function $\mathcal{Z}^{\mathcal{H}}(\xi,T)$. We underline that $\tilde{\mathcal{F}}_0$ depends on the temperature but it cannot depend on ξ. Moreover, we observe that, as already found in the Gibbs free energy, the second term in Eq. (135) accounts for the entropic contribution (effect of thermal fluctuations), whereas the last term represents the purely mechanical energy. This is consistent with the classical definition of Helmholtz free energy

$$\mathcal{F} = U - TS, \tag{136}$$

where T is the temperature, U is the internal energy of the system, and S is its entropy. In this case, since it is the displacement that is imposed, the internal energy is used instead of the enthalpy, see Eq. (32) for comparison. In fact, in the enthalpy function, in addition to the internal energy, there is also the contribution of the energy associated with the applied forces, which are not present here. To summarize, the Gibbs free energy (based on enthalpy) is used for isotensional conditions, and the Helmholtz free energy (based on internal energy) is used with isometric conditions.

The explicit form of the Helmholtz free energy in Eq. (135) represents an important result because it allows us to develop the new version of the Griffith criterion for fracture propagation in a system where the total elongation is prescribed. Specifically, in order to understand how thermal fluctuations influence the crack extension, we study when the derivative of $\tilde{\mathcal{F}}(\xi,T)$ with respect to the extension of the fracture ξ is negative

$$\frac{\partial\tilde{\mathcal{F}}(\xi,T)}{\partial\xi} < 0, \tag{137}$$

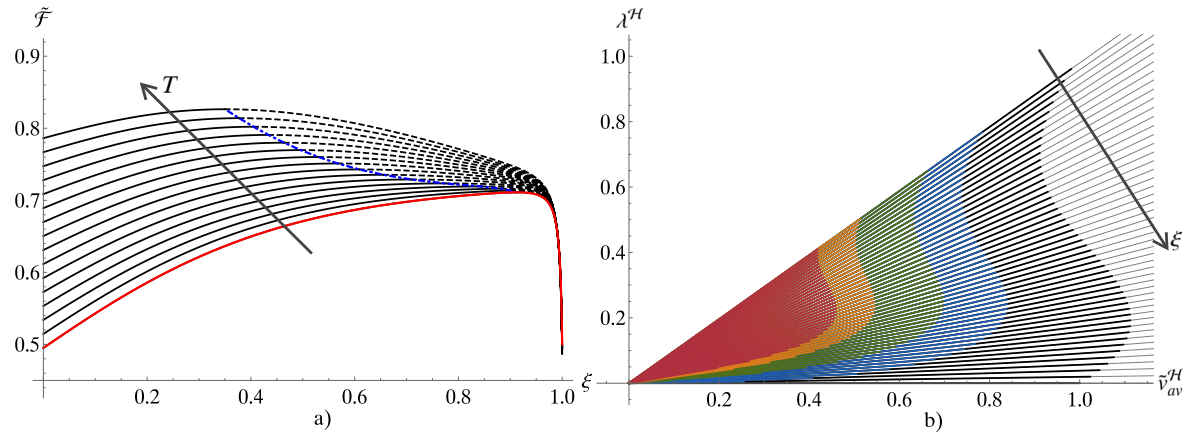

Fig. 15. Temperature effects on the system within the Helmholtz ensemble. In panel (a), the non-dimensional Helmholtz free energy $\tilde{\mathcal{F}}$ is plotted versus the broken portion ξ. The curves describe the behavior at different temperatures T such that $1/\tilde{\beta} \in [0, 0.03]$. The blue dashed curve passes through the energy maximum points. The red curve represent the purely mechanical system at $T = 0$. For this diagram, the values $\nu = 0.05$, $\rho = 0.1$ and $\tilde{\Omega} = 10$ have been used. In panel (b), we show the influence of the temperature on the 1.0 force–displacement relation. We recall that $\tilde{v}^{\mathcal{H}}_{av}$ is the average displacement. The different straight lines correspond to different values of ξ, and the endpoint of each line represents the temperature dependent Griffith threshold. The different colors indicate different temperature values (the black lines correspond to the purely mechanical case ($T = 0$), and the red ones to the larger temperature). The parameter used for this diagram are $\nu = 0.5$ and $\rho = 0.5$.

which corresponds to the condition of fracture propagation. We emphasize again that we have substituted the purely mechanical energy with the Helmholtz free energy to introduce the effects of temperature into the Griffith's criterion. The calculation of the derivative of Eq. (135) yields the temperature dependent condition

$$\frac{\partial \tilde{\mathcal{F}}(\xi, T)}{\partial \xi} = \frac{1}{2\tilde{\beta} Y(\xi)} \frac{\partial Y(\xi)}{\partial \xi} + \frac{\partial \tilde{\phi}_e(\xi)}{\partial \xi} < 0. \tag{138}$$

The first term can be calculated through the result

$$\frac{\partial Y(\xi)}{\partial \xi} = -\frac{1}{\nu} \cosh\left(\frac{\rho\xi}{\nu}\right) \cosh\left(\sqrt{\frac{1+\rho^2}{\nu^2}}(1-\xi)\right), \tag{139}$$

while the derivative $\partial\tilde{\phi}_e/\partial\xi$ of the mechanical energy is given by

$$\frac{\partial \tilde{\phi}_e(\xi)}{\partial \xi} = \frac{1}{2} - \frac{\tilde{\Omega}^2 \rho^2}{2(1+\rho^2)} \left[\frac{\Delta(\xi)}{Y(\xi)}\right]^2. \tag{140}$$

Therefore, using Eqs. (115), (138), (139), (140), and introducing the parameter $\tilde{\beta}^{\mathcal{H}}_c$ defined as

$$\tilde{\beta}^{\mathcal{H}}_c = \frac{1}{\nu Y(\xi)} \cosh\left(\frac{\rho\xi}{\nu}\right) \cosh\left(\sqrt{\frac{1+\rho^2}{\nu^2}}(1-\xi)\right) \tag{141}$$

we obtain the following necessary condition for fracture propagation

$$\tilde{\Omega} > \frac{\sqrt{1+\rho^2}}{\rho} \frac{Y(\xi)}{\Delta(\xi)} \sqrt{1 - \frac{\tilde{\beta}^{\mathcal{H}}_c}{\tilde{\beta}}}. \tag{142}$$

Moreover, similarly to what has been developed for the Gibbs ensemble, we can calculate the critical temperature $T^{\mathcal{H}}_c$ by means of the relation

$$\frac{\tilde{\beta}^{\mathcal{H}}_c}{\tilde{\beta}} = \frac{T}{T^{\mathcal{H}}_c}. \tag{143}$$

The explicit expression of $T_c^{\mathcal{H}}$ reads

$$\begin{aligned} T_c^{\mathcal{H}} &= \frac{\nu E L b Y_M^2 Y(\xi)}{h k_B \cosh\left(\frac{\rho\xi}{\nu}\right)\cosh\left(\sqrt{\frac{1+\rho^2}{\nu^2}}(1-\xi)\right)} = \frac{\nu E L b Y_M^2}{h k_B}\left[\rho\tanh\left(\frac{\rho\xi}{\nu}\right)+\sqrt{1+\rho^2}\tanh\left(\sqrt{\frac{1+\rho^2}{\nu^2}}(1-\xi)\right)\right] \\ &= \frac{\sqrt{\mu E} b Y_M^2}{k_B}\left[\sqrt{\frac{hE_d}{dE}}\tanh\left(\frac{\zeta}{h}\sqrt{\frac{hE_d}{d\mu}}\right)+\sqrt{1+\frac{hE_d}{dE}}\tanh\left(\sqrt{\frac{dE+hE_d}{\mu d h^2}}(L-\zeta)\right)\right], \end{aligned} \tag{144}$$

where ζ is the crack extension, corresponding to $\zeta = \xi L$. Hence, we can write an alternative form of Eq. (142), which describes explicitly the temperature dependent behavior of the Griffith's criterion

$$\tilde{\Omega} > \frac{\sqrt{1+\rho^2}}{\rho}\frac{Y(\xi)}{\Delta(\xi)}\sqrt{1-\frac{T}{T_c^{\mathcal{H}}}} = \tilde{\Omega}_{cr}(0)\sqrt{1-\frac{T}{T_c^{\mathcal{H}}}} =: \tilde{\Omega}_{cr}(T), \tag{145}$$

where $\tilde{\Omega}_{cr}(0)$ is the critical threshold defined for the purely mechanical system in Eq. (121). It is easy to verify that when $T \to 0$, Eq. (145) converges to Eq. (120).

In Fig. 15(a), we exhibit thermal effect on the Helmholtz free energy. Similarly to what has already been observed for the Gibbs ensemble, for increasing temperature values, the maximum of the energy function shifts toward lower values of detached extension ξ. All the curves are obtained applying the same value of prescribed extension $\tilde{\Omega}$. Consequently, this plot demonstrates that as temperature increases, a smaller broken region is sufficient to generate Griffith instability. As before, this means that thermal fluctuations promote fracture propagation.

In Fig. 15(b), we show the force–extension behavior as a function of temperature. More precisely, we use the expected values of force and extension, derived from the fundamental relations of statistical mechanics. To begin, the expectation value of the force, conjugated to the prescribed extension $\tilde{\Omega}$, can be calculated from the Helmholtz free energy, see Eq. (132), as follows

$$\begin{aligned} \langle\lambda\rangle^{\mathcal{H}} &= \frac{\partial\tilde{F}(\xi,T)}{\partial\tilde{\Omega}} = -\frac{1}{\tilde{\beta}\mathcal{Z}^{\mathcal{H}}(\xi,T)}\frac{\partial\mathcal{Z}^{\mathcal{H}}(\xi,T)}{\partial\tilde{\Omega}} \\ &= -\frac{1}{\tilde{\beta}(Y_M)^n\sqrt{\frac{(2\pi n)^n}{\tilde{\beta}^n\det\boldsymbol{Q}}}\exp\left[-\tilde{\beta}\tilde{\phi}_e(\xi)\right]}(Y_m)^n\sqrt{\frac{(2\pi n)^n}{\tilde{\beta}^n\det\boldsymbol{Q}}}\exp\left[-\tilde{\beta}\tilde{\phi}_e(\xi)\right]\frac{\partial\tilde{\phi}_e(\xi)}{\partial\tilde{\Omega}}\left(-\tilde{\beta}\right) = \frac{\partial\tilde{\phi}_e(\xi)}{\partial\tilde{\Omega}} \\ &= \tilde{\Omega}\frac{\rho^2}{1+\rho^2}(1-\xi)+\tilde{\Omega}\frac{\rho\nu}{Y(\xi)(1+\rho^2)\sqrt{1+\rho^2}}\sinh\left(\frac{\rho\xi}{\nu}\right)\sinh\left(\sqrt{\frac{1+\rho^2}{\nu^2}}(1-\xi)\right) = \lambda^{\mathcal{H}}, \end{aligned} \tag{146}$$

where $\lambda^{\mathcal{H}} = \partial\tilde{\phi}_e(\xi)/\partial\tilde{\Omega}$ is the non-dimensional stress calculated for the purely mechanical system. This result shows that this quantity is not affected by thermal effects. We can also determine the expectation value of the displacement vector $\tilde{\boldsymbol{v}}$ by means of the relation

$$\langle\tilde{\boldsymbol{v}}\rangle^{\mathcal{H}} = \frac{(Y_M)^n}{\mathcal{Z}^{\mathcal{H}}(\chi,T)}\int_{\mathbb{R}^n}\tilde{\boldsymbol{v}}\exp\left[-\tilde{\beta}\tilde{\phi}(\tilde{\boldsymbol{v}},\chi)\right]d\tilde{\boldsymbol{v}}. \tag{147}$$

By the definition of $\tilde{\phi}(\tilde{\boldsymbol{v}},\chi)$, given in Eq. (97), we can obtain the more explicit expression

$$\begin{aligned} \langle\tilde{\boldsymbol{v}}\rangle^{\mathcal{H}} &= \frac{(Y_M)^n}{\mathcal{Z}^{\mathcal{H}}(\chi,T)}\int_{\mathbb{R}^n}\tilde{\boldsymbol{v}}\exp\left[-\frac{\tilde{\beta}}{n}\left(\frac{1}{2}\boldsymbol{Q}\tilde{\boldsymbol{v}}\cdot\tilde{\boldsymbol{v}}+\frac{1}{2}\chi\cdot\mathbf{1}+\frac{1}{2}n\rho^2\tilde{\Omega}^2-\rho^2\tilde{\Omega}\tilde{\boldsymbol{v}}\cdot\mathbf{1}\right)\right]d\tilde{\boldsymbol{v}} \\ &= \frac{(Y_M)^n}{\mathcal{Z}^{\mathcal{H}}(\chi,T)}\exp\left[-\frac{\tilde{\beta}}{2n}\left(\chi\cdot\mathbf{1}+n\rho^2\tilde{\Omega}^2\right)\right]\int_{\mathbf{R}^n}\tilde{\boldsymbol{v}}\exp\left[-\frac{\tilde{\beta}}{n}\left(\frac{1}{2}\boldsymbol{Q}\tilde{\boldsymbol{v}}\cdot\tilde{\boldsymbol{v}}-\rho^2\tilde{\Omega}\tilde{\boldsymbol{v}}\cdot\mathbf{1}\right)\right]d\tilde{\boldsymbol{v}}. \end{aligned} \tag{148}$$

Now, if we differentiate Eq. (37) with respect to $\mathbf{a}$, we get the new integral expression

$$\int_{\mathbb{R}^n}\mathbf{y}\exp\left[-\mathbf{M}\mathbf{y}\cdot\mathbf{y}-\mathbf{a}\cdot\mathbf{y}\right]d\mathbf{y} = -\frac{1}{2}\sqrt{\frac{\pi^n}{\det\mathbf{M}}}\exp\left[\frac{1}{4}\mathbf{M}^{-1}\mathbf{a}\cdot\mathbf{a}\right]\mathbf{M}^{-1}\mathbf{a}. \tag{149}$$

Therefore, we can develop Eq. (148), as follows

$$\begin{aligned} \langle\tilde{\boldsymbol{v}}\rangle^{\mathcal{H}} &= \frac{(Y_M)^n}{\mathcal{Z}^{\mathcal{H}}(\chi,T)}\exp\left[-\frac{\tilde{\beta}}{2n}\left(\chi\cdot\mathbf{1}+n\rho^2\tilde{\Omega}^2\right)\right]\sqrt{\frac{(2\pi n)^n}{\tilde{\beta}^n\det\boldsymbol{Q}}}\exp\left[\frac{\tilde{\beta}}{n}\left(\frac{1}{2}\rho^4\tilde{\Omega}^2\mathbf{1}\cdot\mathbf{1}\right)\right]\rho^2\tilde{\Omega}\boldsymbol{Q}^{-1}\mathbf{1} \\ &= \frac{(Y_M)^n}{\mathcal{Z}^{\mathcal{H}}(\chi,T)}\sqrt{\frac{(2\pi n)^n}{\tilde{\beta}^n\det\boldsymbol{Q}}}\exp\left[-\tilde{\beta}\tilde{\phi}_e(\tilde{\boldsymbol{v}})\right]\rho^2\tilde{\Omega}\boldsymbol{Q}^{-1}\mathbf{1} = \tilde{\boldsymbol{v}}_e^{\mathcal{H}}(0), \end{aligned} \tag{150}$$

where we have used Eqs. (101) and (128) for $\tilde{\phi}_e(\tilde{\boldsymbol{v}})$ and $\mathcal{Z}^{\mathcal{H}}(\chi,T)$, respectively, and $\tilde{v}_e^{\mathcal{H}}(0)$ represents the displacement vector at equilibrium obtained for the purely mechanical system in Eq. (100). As a consequence, we observe that the average displacement

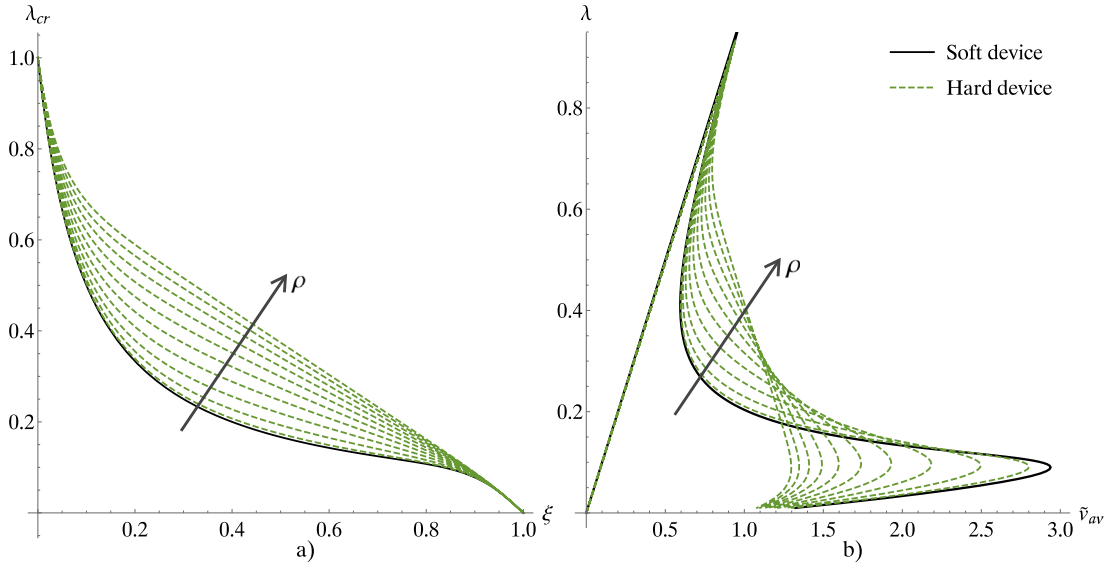

Fig. 16. Comparison of the purely mechanical response in soft and hard device configurations. The dashed green curves represent the isometric system (hard device) for different values of ρ, while the solid black curves correspond to the isotensional system (soft device). In panel (a), we observe that the critical force required for fracture propagation, $\lambda_{cr}^{\mathcal{H}}$, in Eq. (122), converges to $\lambda_{cr}^{\mathcal{G}}$, in Eq. (30), for low values of ρ. In panel (b), the force-average displacement behavior is shown (see Eqs. (30) and (55) for the Gibbs ensemble, and Eqs. (103) and (104) for the Helmholtz ensemble). Also in this case, the convergence for low values of ρ is demonstrated and this means that Gibbs' behavior converges to Helmholtz's behavior with a soft device. In both plots, $\nu = 0.1$ and $\rho \in [0.1, 1]$ have been used.

for the thermo-mechanical system within the Helmholtz ensemble converges to the average displacement of the purely mechanical system, previously evaluated in Eq. (103). Indeed, we can write

$$\tilde{v}_{av}^{\mathcal{H}}(T) = \frac{1}{n}\tilde{\boldsymbol{v}}_e^{\mathcal{H}}(0)\cdot\mathbf{1} = \frac{1}{n}\rho^2\tilde{\Omega}\mathbf{Q}^{-1}\mathbf{1}\cdot\mathbf{1} = \tilde{v}_{av}^{\mathcal{H}}(0). \tag{151}$$

In the limit for $n \to \infty$, we can calculate the average displacement from Eq. (114), and we get

$$\begin{aligned}\tilde{v}_{av}^{\mathcal{H}} &= \int_0^{1-\xi} \tilde{v}_I^{\mathcal{H}}(\tilde{x})d\tilde{x} + \int_{1-\xi}^{1} \tilde{v}_B^{\mathcal{H}}(\tilde{x})d\tilde{x} \\ &= \tilde{\Omega}\frac{\xi}{1+\rho^2} + \tilde{\Omega}\frac{\rho^2}{1+\rho^2} + \tilde{\Omega}\frac{\nu}{\Upsilon(\xi)\rho(1+\rho^2)\sqrt{1+\rho^2}}\sinh\left(\frac{\rho\xi}{\nu}\right)\sinh\left(\sqrt{\frac{1+\rho^2}{\nu^2}}(1-\xi)\right).\end{aligned} \tag{152}$$

The relationships found allow us to obtain the force–strain relationship as depicted in Fig. 15(b). Each straight line corresponds to a different value of ξ and it is determined by using Eqs. (146) and (152). Therefore, the slope is not affected by the temperature. This depends on the fact that the system is linear from the point of view of elasticity theory when ξ has a well-determined value. However, the Griffith threshold is influenced by the temperature as indicated in the plot, where one can see that the fracture threshold decreases with increasing temperature. This behavior is consistent with what has already been described for the Gibbs ensemble, and with the general idea that thermal fluctuations promote fracture propagation.

To conclude this discussion, let us compare the behavior of the system in the isotensional and isometric conditions. Although the behavior is quantitatively different, we can find a condition of convergence between the two statistical ensembles, corresponding to a very soft traction device. In fact, when the device is soft ($\rho \to 0$), the Helmholtz ensemble converges to the Gibbs ensemble. This is true for the purely mechanical case (i.e., at zero temperature) as seen in Fig. 16, and also for arbitrary values of temperature as seen in Fig. 17.

In Fig. 16(a), we show the behavior of critical load as a function of the fracture progress. It is clearly seen that, as the value of ρ decreases, the curves corresponding to the isometric conditions converge to the curve of the isotensional model. Moreover, all curves are consistent with Griffith's criterion since the critical load decreases as the initial fracture extension increases. Similar behavior is observed in Fig. 16(b), where the relationship between applied load and average displacement is shown for the two boundary conditions. Again, in fact, the isometric curves converge to the isotensional one for small values of ρ, i.e., with an easily deformable tensile device. We remark that, in that plot, the curves are constructed by the same method adopted in Fig. 15(b), but we used zero temperature. We remark that, when we consider this model as a tool for describing the behavior of the process zone, Figs. 15 and 16 show that different Barenblatt type cohesive fracture behaviors can be obtained by varying the molecular scale geometrical and material parameters.

When we consider the effects of temperature, we find the critical behavior for both Gibbs and Helmholtz ensembles, as shown in Fig. 17(a). In fact, for both statistical ensembles we observe the presence of a phase transition characterized by a critical temperature

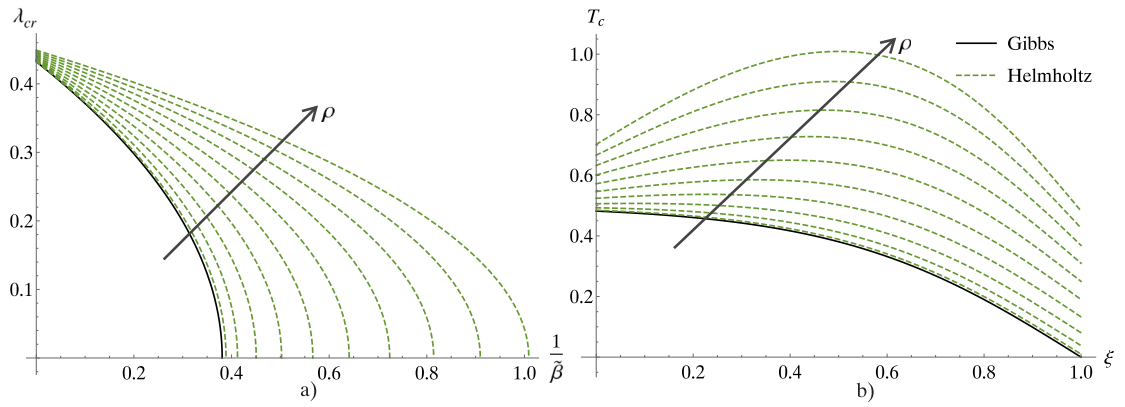

Fig. 17. Comparison of thermal effects under Gibbs and Helmholtz ensembles. The dashed green curves represent the Helmholtz ensemble, while the solid black curve describes the Gibbs ensemble. In panel (a), we show the critical stress versus the temperature (represented by $1/\tilde{\beta}$). For Gibbs ensemble we used Eq. (54), while for Helmholtz ensemble, we used Eq. (146), where we substituted the temperature dependent critical value of the prescribed extension $\tilde{\Omega}_{cr}$ given in Eq. (145). In panel (b), the critical temperature is represented versus the broken fraction, by using Eqs. (53) and (144). For both panels, we adopted the elastic ratio $\nu = 0.5$ and $\rho \in [0.1, 1]$ (in the first panel, we also considered a broken fraction equal to $\xi = 0.5$).

corresponding to the complete fracture caused only by thermal fluctuations. With respect to this point, it is interesting to observe that the Helmholtz critical temperature value in Eq. (144) converges to the corresponding Gibbs value in Eq. (53), when ρ approaches zero. This can be also underlined in Fig. 17(a), where it can be seen that the critical load as a function of temperature in the Helmholtz ensemble converges to that of Gibbs for increasingly soft devices. Finally, in Fig. 17(b), we directly represented the behavior of critical temperature as a function of fracture state of progression for the two statistical ensembles. Once again we observe the convergence of the Helmholtz response to the Gibbs response for $\rho \to 0$. Furthermore, it is interesting to point out that for higher values of the parameter ρ, the critical temperature in the Helmholtz ensemble exhibits a maximum value for some value of ξ, and that this non-monotonic behavior is absent in the Gibbs ensemble. It means that the Helmholtz system is able to resist thermal fluctuations better in an intermediate state of fracture progression.

Observe that the critical temperature obtained within the Helmholtz ensemble is defined as the temperature able to induce the complete fracture when the applied displacement is fixed to zero. Of course, it is also possible to redefine this critical temperature by maintaining the system at an arbitrary value δ of the applied displacement. For $\delta = 0$ the critical behavior is described by Eq. (145), and this expression can be elaborated as follows

$$\sqrt{\tilde{\Omega}_{cr}^2(T) - \delta^2} = \sqrt{\tilde{\Omega}_{cr}^2(0)\left(1 - \frac{T}{T_c^{\mathcal{H}}}\right) - \delta^2} = \sqrt{\tilde{\Omega}_{cr}^2(0) - \delta^2}\sqrt{1 - \frac{\tilde{\Omega}_{cr}^2(0)}{\tilde{\Omega}_{cr}^2(0) - \delta^2}\frac{T}{T_c^{\mathcal{H}}}}. \tag{153}$$

This expression allows us to define a new value of the critical temperature corresponding to a fixed displacement δ, as follows

$$T_{c,\delta}^{\mathcal{H}} = \frac{\tilde{\Omega}_{cr}^2(0) - \delta^2}{\tilde{\Omega}_{cr}^2(0)} T_c^{\mathcal{H}}. \tag{154}$$

An interesting case corresponds to $\delta = 1$, which is exactly the decohesion threshold. The behavior of $T_{c,1}^{\mathcal{H}}$ is represented in Fig. 18, where we show the critical temperature versus ξ when the applied displacement is $\delta = 1$. We represented this quantity for two different values of ν in panels (a) and (b). In both cases, we see that the critical temperature at the fully broken system ($\xi = 1$) is always zero, regardless of the value of ρ and consistent with the results of the Gibbs ensemble. This happens because the value $\delta = 1$ corresponds precisely to the breaking threshold. In Fig. 17(b), this did not happen because the system was kept at $\delta = 0$ and thus there was a conflict between mechanical and thermal detachment. Finally, we observe that the value of ν can affect the behavior of the critical temperature shifting from a non-monotonic to a monotonic curve from Fig. 18(a) to (b).

In conclusion, we observe that despite the convergence of the Helmholtz ensemble to the Gibbs ensemble for $\rho \to 0$, the two behaviors remain different for arbitrary values of ρ, and thus the two ensembles are not equivalent in the continuous limit we have developed. This observed non-equivalence is similar to the one previously proved for the adhesion phenomena, where we considered the alternative thermodynamic limit (Florio et al., 2020; Cannizzo et al., 2021).

6. Comparison with simulations of graphene fracture

In this section, we test the effectiveness of our model in capturing the influence of thermal fluctuations on fracture propagation by comparing our theoretical results with molecular dynamics (MD) simulations of 2D pristine graphene, reported by Gamboa-Suárez et al. (2022). In their paper, the authors investigate the impact of temperature on the fracture mechanical properties of 2D carbon sheets, in particular those of pristine graphene. Previous studies had already observed a general decrease in mechanical

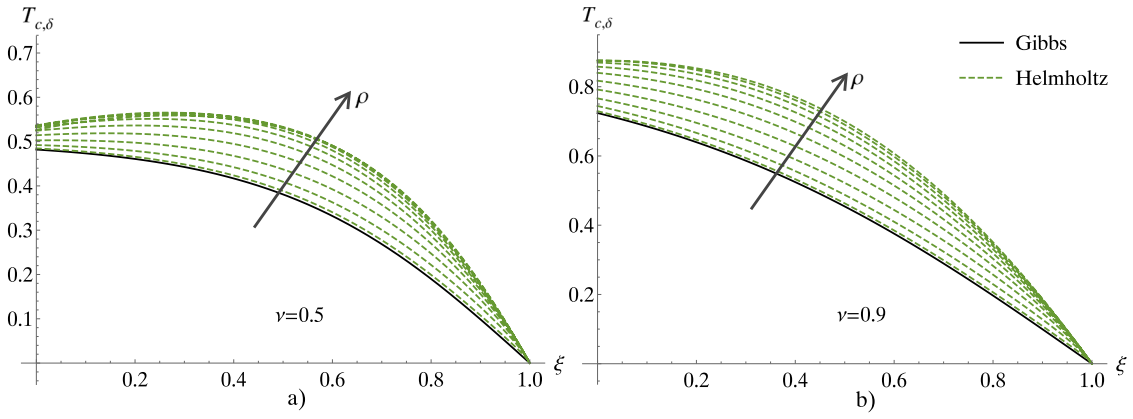

Fig. 18. Critical temperature for a prescribed displacement $\delta = 1$. In both panels we represent the curves for the Helmholtz ensemble (dashed green) that converge to the Gibbs ensemble (solid black curves). For both panels $\rho \in [0.1, 1]$. In panel (a) the elastic ratio is $\nu = 0.5$, and in panel (b) it is $\nu = 0.9$.

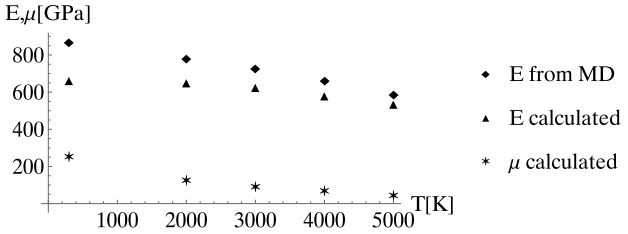

Fig. 19. Graphene elastic moduli at different temperatures: the diamond symbols correspond to the Young's modulus tangent values, obtained by Gamboa-Suárez et al. (2022), the upward-pointing triangle symbols represent the Young's modulus secant values, and the asterisk symbols correspond to the shear modulus we adopted for the comparison.

properties with increasing temperature (both elastic constants and strength), though these analyses were limited to a relatively narrow temperature range (Wang et al., 2012; Li et al., 2019). In Gamboa-Suárez et al. (2022), the authors examine the mechanical properties over a broader temperature spectrum, from 300 K to 5000 K. We emphasize that the exact melting temperature of graphene is not known but the initial stages of melting of graphene have been observed between 4000 K and 6000 K (Ganz et al., 2017). More specifically, Gamboa-Suárez et al. (2022) consider a 2D pristine graphene sheet consisting of 10 032 atoms, and calculate the mechanical properties using molecular dynamics methods, and modeling the interatomic interactions through the SED-REBO potential (Perriot et al., 2013). The authors report the temperature dependence of graphene's mechanical properties applying the traction along both the armchair (AC) and zigzag (ZZ) directions. In the following, we focus on the thermo-mechanical response along the AC direction, since in this case the fracture propagates between parallel carbon bonds, exactly as in our theoretical model, see Fig. 4 in Gamboa-Suárez et al. (2022).

To compare our theoretical results with those presented in Gamboa-Suárez et al. (2022), we adopt the following approach: considering that the MD simulations use a graphene sheet composed of 10 032 carbon atoms, the system forms a square with dimensions $L \times L$, with $L \simeq 123$ Å. From this configuration, we select a single layer of hexagonal cells aligned in a row. This system resembles the structure illustrated in Fig. 2, with the key difference being that graphene's cells are hexagonal rather than square. The height h is taken as the length of one side of the hexagonal graphene cell, namely $h = 1.42$ Å, while the thickness b is assumed, as is customary in graphene MD simulations, as the diameter of a carbon atom, $b = 3.35$ Å.

To derive the stress–strain and critical stress–temperature curves, we use the dimensional form of the Eqs. (30) and (54), taking into account Eqs. (6) and (8). We get

$$\sigma_{cr}^{\mathcal{G}}(0) = \frac{EY_M}{h + \zeta \coth\left(\sqrt{\frac{E}{\mu}}\frac{L-\zeta}{h}\right)\sqrt{\frac{E}{\mu}}}, \qquad \sigma_{cr}^{\mathcal{G}}(T) = \sigma_{cr}^{\mathcal{G}}(0)\sqrt{1 - \frac{T}{T_c^{\mathcal{G}}}}, \tag{155}$$

with critical temperature defined in Eq. (53), and the average strain calculated from Eq. (55) as

$$\varepsilon_{av} = \frac{v_{av}^{\mathcal{G}}}{h} = \frac{\tilde{v}_{av}^{\mathcal{G}} Y_M}{h} = \frac{\sigma}{E} + \frac{\sigma\zeta}{EL} + \frac{\sigma\zeta^2}{ELh}\sqrt{\frac{E}{\mu}}\coth\left(\sqrt{\frac{E}{\mu}}\frac{L-\zeta}{h}\right) + \frac{\sigma\zeta^3}{3\mu L h^2}. \tag{156}$$

Since the molecular dynamics simulations have been performed by implementing both a thermostat and a barostat, we used the theoretical results obtained within the Gibbs ensemble. We assume that the initial broken portion of the system represents 0.9% of the total length L, thus $\zeta = 0.009L$, and the extension threshold corresponds to 37% of the height h, $Y_M = 0.529$ Å.

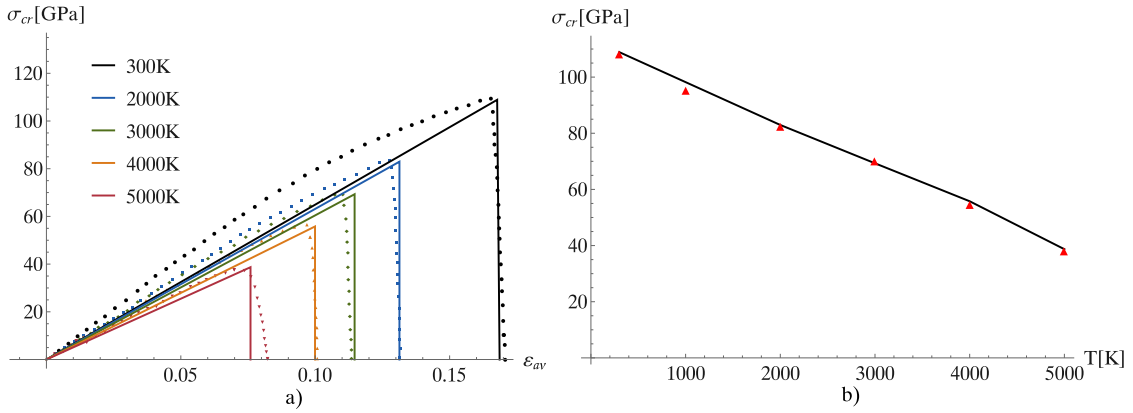

Fig. 20. Comparison of results obtained with our model and with MD simulations proposed by Gamboa-Suárez et al. (2022). In panel (a) stress–strain curves at different temperatures: the solid lines are the responses given by our model, the points represent MD simulations. In panel (b) critical stress–temperature curve: the red triangles show the MD simulation points, and the black curve is obtained from the results given by our model.

Regarding Young's modulus E, we choose to use the secant modulus, which slightly differs from the tangent modulus calculated in Gamboa-Suárez et al. (2022). This choice is motivated by the fact that graphene exhibits highly nonlinear behavior (Cadelano et al., 2009). We are attempting to give an interpretation of numerical results concerning this nonlinear system with a linear model. Hence, the secant Young's modulus helps to mitigate this different behavior by accurately reflecting the temperature-dependent response of the system, avoiding the bias introduced by the nonlinearity. Also for the shear modulus, we fitted its value for each temperature. In Fig. 19 we show the values of graphene elastic moduli at different temperatures: the diamond symbols correspond to the Young's modulus tangent values, obtained by Gamboa-Suárez et al. (2022), the upward-pointing triangle symbols represent the Young's modulus secant values, and the asterisk symbols correspond to the shear modulus we adopted for the comparison.

In Fig. 20 we show the comparison between the results obtained with the proposed model and the MD simulations for the stress–strain curves and for the critical stress as function of the temperature. In Fig. 20(a), we plot stress–strain curves at different temperatures, ranging from 300 K to 5000 K: the solid lines are obtained from Eqs. (155) and (156), while the points are extracted from MD simulations. In Fig. 20(b), we show the critical stress as function of the temperature: the solid black line is derived from Eq. (155), and the red triangles are the points computed in Gamboa-Suárez et al. (2022). A good agreement between MD simulations and our theoretical model can be underlined and validates the use of our model for describing fracture in nanosystems.

7. Discussion and conclusion

In this paper, we have presented a simplified fracture model that allows the effects of thermal fluctuations to be introduced in a rigorous way, namely through classical statistical mechanics (Gibbs, 1902; Weiner, 1983). In addition, such a model is able to correct some well-known problems of linear elastic fracture mechanics. In particular, we obtain a finite fracture nucleation stress, and a finite value of the stress at the crack tip, which are features experimentally verified. In the development of the model, the multiscale paradigm was implemented in the following way: initially, the model is introduced through a discrete structure formed by linear springs, some of which have a rupture threshold useful to study the propagation of a fracture. This allows us to discuss a discrete version of the Griffith's criterion and its interpretation. In a second step, the continuous limit of that structure was developed in order to have a model capable of describing the behavior of a system at the mesoscopic scale. For this purpose, all the discrete parameters were properly rescaled to have a correct convergence of the discrete model to the continuous one, exactly as happens in Γ-convergence theory (Braides, 2002; Dal Maso, 2012). The need to begin the treatment from a discrete model comes from the fact that we need a numerable set of variables to apply statistical mechanics, and in particular to calculate the partition function of the system in the established statistical ensemble (Gibbs, 1902; Weiner, 1983). The partition function is the most important quantity, which allows by derivation to obtain the average value of any physical observable. Once the main thermodynamic variables have been calculated for the discrete model (in particular free energies), the continuous limit can be applied to obtain the thermomechanic behavior of the continuous system at the mesoscale. In both the discrete model and its continuous limit, the fracture geometry is introduced by imposing the fracture progress state in a one-dimensional breakable structure. This means that the fraction of the fractured system (starting from the right and proceeding to the left, considering only one front or domain wall) is imposed and the corresponding elastic fields and energy functions are calculated analytically. In this way it is possible to determine the propagation condition for the fracture by applying the Griffith (1921) criterion: the fracture propagates if this process is energetically favorable, *i.e.*, if the total energy decreases with the advancement of the fracture. This total energy, for the purely mechanical system, is composed of the elastic energy, the energy of the applied loads, and the fracture energy, originally introduced by Griffith (1921). However, when we study the effects of the thermal fluctuations on the Griffith condition, we have to add the entropic term, whose evaluation represents the most important result obtained through the application of the statistical mechanics. In other terms, we can

say that for applying the Griffith criterion to a system embedded in a thermal bath at a given temperature, we have to substitute the total mechanical energy with the pertinent free energy, compatible with the specific boundary conditions, and automatically considering thermal fluctuations (Eftis and Liebowitz, 1976; Stevens and Guiu, 1991). The decrease in total energy (or free energy) for a propagating fracture immediately leads to the concept of energy release rate, which represents the derivative of energy (except for the fracture energy) with respect to the state of advancement (extension) of the fracture. This quantity, useful for an alternative characterization of the Griffith criterion, was calculated exactly for our model, and its link with the concepts of stress intensity factor and J-integral was shown. The elastic energy of the proposed models does not depend exclusively on the elastic strain, as usually happens, but also on the displacement field. For this reason, in calculating the J-integral, we had to implement an original approach that takes into account the actual complexity of our energy function. The approach described has been carefully developed for two different boundary conditions, which represent two different statistical ensembles of the statistical mechanics: the soft device configuration, which corresponds to the application of an external force field, that is to the Gibbs statistical ensemble, and the hard device configuration, which corresponds to the prescription of the displacement field, and then to the Helmholtz statistical ensemble (Giordano, 2017; Bellino et al., 2019). In both cases, the fundamental result we demonstrate concerns the temperature dependence of the Griffith threshold for the fracture advancement, describing a specific critical behavior. In fact, both the threshold force and the threshold displacement decrease with temperature with a law of the type $\sqrt{1-T/T_c}$, which corresponds to a second order phase transition. More precisely, we proved that the purely mechanical Griffith threshold must be multiplied by $\sqrt{1-T/T_c}$ when thermal fluctuations are to be taken into account. The critical temperature T_c has been calculated in closed form, and depends on the physical and geometrical parameters of the system. Moreover, it also depends on the actual extension of the fracture and therefore it can change its value during the fracture propagation. We want to underline that the critical behavior, characterized by phase transitions, obtained for systems in the continuum limit represents an important theoretical result from the point of view of the statistical mechanics. These behaviors are in fact mostly studied in discrete systems. We showed the application of our model, in the case of the Gibbs ensemble, to the interpretation of fracture in graphene, studied by molecular dynamics methods. The results showed good agreement between simulations and theory. Also the temperature dependent fracture surface energy obtained from experiments on platinum and iron has been compared with theoretical results, showing an excellent agreement.

This work opens different perspectives. First of all, we can think to generalize the model in order to consider the real dynamics imposed by the speed of application of the loads. In our development, we adopted the equilibrium statistical mechanics and therefore the results are valid in a quasi-static regime, in which the system is able to re-equilibrate on timescales smaller than those of applied loading. For higher speed of the traction process, it becomes important to implement the out-of-equilibrium statistical mechanics and, in particular, to approach the problem by means of Langevin or Fokker–Planck equations. A simplified method could be based on the Kramers law and the transition state theory (Weiner, 1983; Giordano et al., 2023; Cannizzo and Giordano, 2024). In any case, the fracture propagation with thermal and dynamic effects requires further studies in the near future. Another important aspect, regarding the possible applications of our approach, concerns the integration of the model within numerical techniques for continuum mechanics. In fact, we can think of using numerical multiscale techniques, where the mesoscale behavior of the fracture process zone is implemented through our model, and the surrounding zones are described by classical finite element or finite difference schemes. To this end it is necessary to implement a bridging between the two methodologies to eventually get a combined system, which can be numerically studied to couple the mechanical and thermal effects on fracture propagation. Another generalization concerns the consideration of a more complex fracture structure. Indeed, the developed model allows the determination of the fracture propagation strategy also in presence of complex cracks configurations such as bubbles, different interacting cracks, periodic distribution of cracks, and so on. These aspects were not considered in this first work as we focused on the thermal effects on a single fracture front, but will be investigated in future developments.

CRediT authorship contribution statement

Claudia Binetti: Writing – original draft, Visualization, Software, Methodology, Investigation, Formal analysis, Conceptualization. **Giuseppe Florio:** Writing – original draft, Methodology, Funding acquisition, Conceptualization. **Nicola M. Pugno:** Writing – original draft, Methodology, Funding acquisition, Conceptualization. **Stefano Giordano:** Writing – original draft, Methodology, Funding acquisition, Conceptualization. **Giuseppe Puglisi:** Writing – original draft, Methodology, Funding acquisition, Conceptualization.

Declaration of Generative AI and AI-assisted technologies in the writing process

During the preparation of this work, the authors used Deepl and ChatGPT to correct and improve the text. After using this tool/service, the authors reviewed and edited the content as needed and take full responsibility for the content of the published article.

Declaration of competing interest

The authors declare that they have no known competing financial interests or personal relationships that could have appeared to influence the work reported in this paper.

Acknowledgments

C.B., G.F. and G.P. have been supported by GNFM - Gruppo Nazionale per la Fisica Matematica(INdAM), Italy. G.F. and G.P.'s research is funded by the European Union (EU) - Next Generation EU. G.P. and G.F. are supported by PNRR, Italy, National Center for HPC, Italy, Big Data and Quantum Computing - M4C2 - I 1.4, Italy (grant number N00000013, CUP D93C22000430001) - Spoke 5 (Environment and Natural Disasters). G.P. and C.B. are supported by the Project of National Relevance (PRIN), Italy, financed by EU - Next- GenerationEU - NRRP - M4C2 - I 1.1, CALL PRIN 2022 PNRR (Project P2022KHFNB, CUP D53D23018910001) granted by the Italian MUR. G.P. is supported by the PRIN, Italy, financed by Eu - Next- Generation EU - NRRP - M4C2 - I 1.1, CALL PRIN 2022 (Project 2022XLBLRX, CUP D53D23006020006) granted by the Italian MUR. G.F. is supported by the PRIN, Italy, financed by EU - Next-Generation EU - NRRP - M4C2 - I 1.1, CALL PRIN 2022 PNRR (Project P2022MXCJ2, CUP D53D23018940001) and CALL PRIN 2022 (Project 2022MKB7MM, CUP D53D23005900006) granted by the Italian MUR. G.F. is also supported by "Istituto Nazionale di Fisica Nucleare" (INFN), Italy through the project QUANTUM. S.G. and C.B. have been supported by "Central Lille, France" and "Région Hauts de France" under project StaMeNa (Statistical mechanics for macromolecular structures of nanotechnology). N.M.P. acknowledges the financial support of the European Union - Next Generation EU - National Recovery and Resilience Plan - NRRP - M4C2 - I 1.1, CALL PRIN 2022 D.D. 104/02-02-2022 - (PRIN2022 2022ATZCJN AMPHYBIA) CUP N. E53D23003040006. C.B. has been supported by "Université Franco Italienne, France" under the mobility grant VINCI 2024. The authors acknowledge useful discussions on the subject of the paper with Djimedo Kondo.

Appendix. Calculations for the soft device

In this Appendix, we provide all detailed calculations required to obtain the expressions for the minimized energy and for the partition function within the Gibbs isotensional configuration, when the continuum limit is considered ($n \to \infty$). We begin by outlining our procedure for calculating the inverse matrix $\mathbf{B}^{-1}$, used in Eq. (15). Next, we analyze the asymptotic behavior, as $n \to \infty$, of the sum $\mathbf{B}^{-1}\mathbf{1}\cdot\mathbf{1}$, useful to derive Eq. (16) for the total energy in the continuum limit. Finally, we examine the asymptotic behavior of $\det \mathbf{B}$ to obtain the Gibbs partition function, given in Eq. (41).

A.1. Determination of the inverse matrix $\mathbf{B}^{-1}$

To make the calculations easier, we observe that $\mathbf{B}$ can be written as

$$\mathbf{B} = n^2\nu^2\left[\mathbf{A} - \left(\mathbf{e}_1 \otimes \mathbf{e}_1 + \mathbf{e}_n \otimes \mathbf{e}_n\right)\right], \tag{A.1}$$

where we have defined the tensor product of two vectors $\mathbf{a}$ and $\mathbf{b}$ such that $(\mathbf{a}\otimes\mathbf{b})\mathbf{c} = (\mathbf{b}\cdot\mathbf{c})\mathbf{a}$ for all vectors $\mathbf{c}$ (so that in a given framework $(\mathbf{a}\otimes\mathbf{b})_{ij} = a_i b_j$). Moreover, we defined $\mathbf{e}_i$ as the ith element of the canonical basis of $\mathbf{R}^n$. The matrix $\mathbf{A}$ is tridiagonal and symmetric, and can be written as

$$\mathbf{A} = \begin{bmatrix} \mathcal{A}_1 & -1 & 0 & \dots & 0 \\ -1 & \mathcal{A}_2 & -1 & \ddots & \vdots \\ 0 & \ddots & \ddots & \ddots & 0 \\ \vdots & \ddots & -1 & \mathcal{A}_{n-1} & -1 \\ 0 & \dots & 0 & -1 & \mathcal{A}_n \end{bmatrix} \tag{A.2}$$

with $\mathcal{A}_i = \left(1-\chi_i\right)/\left(n^2\nu^2\right) + 2$, for $i = 1 \dots n$. Therefore, we have to determine the inverse matrix

$$\mathbf{B}^{-1} = \frac{1}{n^2\nu^2}\left[\mathbf{A} - \left(\mathbf{e}_1 \otimes \mathbf{e}_1 + \mathbf{e}_n \otimes \mathbf{e}_n\right)\right]^{-1}. \tag{A.3}$$

Since $\mathbf{A}$ is a tridiagonal symmetric matrix, also its inverse is symmetric. For later use, we identify the elements of the first and last row and column of the inverse $\mathbf{A}^{-1}$ as

$$\mathcal{A}^{-1}_{1j} = \mathcal{A}^{-1}_{j1} = q_j, \qquad \mathcal{A}^{-1}_{nj} = \mathcal{A}^{-1}_{jn} = w_j, \tag{A.4}$$

where we have introduced the two vectors $\boldsymbol{q}$ and $\boldsymbol{w}$

$$\boldsymbol{q} = \begin{Bmatrix} q_1 \\ q_2 \\ \vdots \\ q_n \end{Bmatrix}, \quad \boldsymbol{w} = \begin{Bmatrix} w_1 \\ w_2 \\ \vdots \\ w_n \end{Bmatrix}. \tag{A.5}$$

Therefore, we notice that $q_n = w_1$. It is possible now to prove that for a generic non-singular matrix $\mathbf{M}$, a vector $\mathbf{m}$, and a scalar quantity β, the inverse of $[\mathbf{M} + \beta\,(\mathbf{m}\otimes\mathbf{m})]$ reads

$$[\mathbf{M} + \beta\,(\mathbf{m}\otimes\mathbf{m})]^{-1} = \mathbf{M}^{-1} - \beta\frac{\mathbf{M}^{-1}(\mathbf{m}\otimes\mathbf{m})\mathbf{M}^{-1}}{1+\beta\mathbf{M}^{-1}\mathbf{m}\cdot\mathbf{m}}. \tag{A.6}$$

Therefore, we apply this property twice to Eq. (A.3), considering that in our case $\beta = -1$ in both steps. We evaluate

$$n^2 v^2 \mathbf{B}^{-1} = \mathbf{Y}^{-1} + \frac{\mathbf{Y}^{-1}\mathbf{e}_n \otimes \mathbf{e}_n \mathbf{Y}^{-1}}{1 - \mathbf{Y}^{-1}\mathbf{e}_n \cdot \mathbf{e}_n}, \tag{A.7}$$

where

$$\mathbf{Y}^{-1} = \mathbf{A}^{-1} + \frac{\mathbf{A}^{-1}\mathbf{e}_1 \otimes \mathbf{e}_1 \mathbf{A}^{-1}}{1 - \mathbf{A}^{-1}\mathbf{e}_1 \cdot \mathbf{e}_1}. \tag{A.8}$$

It is easy to recognize that

$$\begin{aligned} &\mathbf{A}^{-1}\mathbf{e}_1 \otimes \mathbf{e}_1 \mathbf{A}^{-1} = \boldsymbol{q} \otimes \boldsymbol{q}, \\ &\mathbf{A}^{-1}\mathbf{e}_1 \cdot \mathbf{e}_1 = q_1, \end{aligned} \tag{A.9}$$

and therefore, Eq. (A.8) can be written as

$$\mathbf{Y}^{-1} = \mathbf{A}^{-1} + \frac{\boldsymbol{q} \otimes \boldsymbol{q}}{1 - q_1}. \tag{A.10}$$

Substituting this result in Eq. (A.7), we obtain

$$n^2 v^2 \mathbf{B}^{-1} = \mathbf{A}^{-1} + \frac{\boldsymbol{q} \otimes \boldsymbol{q}}{1 - q_1} + \frac{\left(\mathbf{A}^{-1} + \frac{\boldsymbol{q} \otimes \boldsymbol{q}}{1 - q_1}\right) \mathbf{e}_n \otimes \mathbf{e}_n \left(\mathbf{A}^{-1} + \frac{\boldsymbol{q} \otimes \boldsymbol{q}}{1 - q_1}\right)}{1 - \left(\mathbf{A}^{-1} + \frac{\boldsymbol{q} \otimes \boldsymbol{q}}{1 - q_1}\right) \mathbf{e}_n \cdot \mathbf{e}_n} = \mathbf{A}^{-1} + \frac{\boldsymbol{q} \otimes \boldsymbol{q}}{1 - q_1} + \frac{\mathcal{N}}{\mathcal{D}}. \tag{A.11}$$

We calculate the denominator $\mathcal{D}$ as follows

$$\mathcal{D} = 1 - \mathbf{A}^{-1}\mathbf{e}_n \cdot \mathbf{e}_n - \frac{\boldsymbol{q} \otimes \boldsymbol{q}}{1 - q_1}\mathbf{e}_n \cdot \mathbf{e}_n = 1 - w_n - \frac{q_n^2}{1 - q_1}, \tag{A.12}$$

where we used the properties

$$\begin{aligned} &\mathbf{A}^{-1}\mathbf{e}_n \cdot \mathbf{e}_n = w_n, \\ &(\boldsymbol{q} \otimes \boldsymbol{q})\,\mathbf{e}_n \cdot \mathbf{e}_n = q_n^2. \end{aligned} \tag{A.13}$$

On the other side, expanding the products, the numerator $\mathcal{N}$ can be written as

$$\mathcal{N} = \left(\mathbf{A}^{-1}\mathbf{e}_n \otimes \mathbf{e}_n \mathbf{A}^{-1}\right) + \left(\mathbf{A}^{-1}\mathbf{e}_n \otimes \mathbf{e}_n \frac{\boldsymbol{q} \otimes \boldsymbol{q}}{1 - q_1}\right) + \left(\frac{\boldsymbol{q} \otimes \boldsymbol{q}}{1 - q_1}\mathbf{e}_n \otimes \mathbf{e}_n \mathbf{A}^{-1}\right) + \left(\frac{(\boldsymbol{q} \otimes \boldsymbol{q})\left(\mathbf{e}_n \otimes \mathbf{e}_n\right)(\boldsymbol{q} \otimes \boldsymbol{q})}{\left(1 - q_1\right)^2}\right). \tag{A.14}$$

The four terms can be calculated as follows

$$\begin{aligned} &\mathbf{A}^{-1}\mathbf{e}_n \otimes \mathbf{e}_n \mathbf{A}^{-1} = \boldsymbol{w} \otimes \boldsymbol{w}, \\ &\mathbf{A}^{-1}\left(\mathbf{e}_n \otimes \mathbf{e}_n\right)(\boldsymbol{q} \otimes \boldsymbol{q}) = (\boldsymbol{w} \otimes \boldsymbol{q})\, q_n, \\ &(\boldsymbol{q} \otimes \boldsymbol{q})\left(\mathbf{e}_n \otimes \mathbf{e}_n\right)\mathbf{A}^{-1} = (\boldsymbol{q} \otimes \boldsymbol{w})\, q_n, \\ &(\boldsymbol{q} \otimes \boldsymbol{q})\left(\mathbf{e}_n \otimes \mathbf{e}_n\right)(\boldsymbol{q} \otimes \boldsymbol{q}) = (\boldsymbol{q} \otimes \boldsymbol{q})\, q_n^2, \end{aligned} \tag{A.15}$$

so that $\mathcal{N}$ becomes

$$\mathcal{N} = \boldsymbol{w} \otimes \boldsymbol{w} + \frac{(\boldsymbol{w} \otimes \boldsymbol{q})\, q_n}{1 - q_1} + \frac{(\boldsymbol{q} \otimes \boldsymbol{w})\, q_n}{1 - q_1} + \frac{(\boldsymbol{q} \otimes \boldsymbol{q})\, q_n^2}{\left(1 - q_1\right)^2}. \tag{A.16}$$

By substituting $\mathcal{D}$ and $\mathcal{N}$ in Eq. (A.11), we obtain

$$n^2 v^2 \mathbf{B}^{-1} = \mathbf{A}^{-1} + \frac{\boldsymbol{q} \otimes \boldsymbol{q}}{1 - q_1} + \frac{\boldsymbol{w} \otimes \boldsymbol{w} + \frac{(\boldsymbol{w} \otimes \boldsymbol{q})\, q_n}{1 - q_1} + \frac{(\boldsymbol{q} \otimes \boldsymbol{w})\, q_n}{1 - q_1} + \frac{(\boldsymbol{q} \otimes \boldsymbol{q})\, q_n^2}{\left(1 - q_1\right)^2}}{1 - w_n - \frac{q_n^2}{1 - q_1}}, \tag{A.17}$$

and simplifying, we get the expression for the inverse matrix $\mathbf{B}^{-1}$

$$n^2 v^2 \mathbf{B}^{-1} = \mathbf{A}^{-1} + \frac{\left(1 - w_n\right)\boldsymbol{q} \otimes \boldsymbol{q} + \left(1 - q_1\right)\boldsymbol{w} \otimes \boldsymbol{w} + (\boldsymbol{q} \otimes \boldsymbol{w} + \boldsymbol{w} \otimes \boldsymbol{q})\, q_n}{\left(1 - w_n\right)\left(1 - q_1\right) - q_n^2}. \tag{A.18}$$

This is the first result of our procedure, and it shows that only the inverse matrix $\mathbf{A}^{-1}$ must be calculated to obtain $\mathbf{B}^{-1}$. For this purpose, we adopt the algorithm developed by Usmani (1994) for determining the explicit inverse of a general tridiagonal matrix.

Accordingly, we consider a generic tridiagonal matrix $\mathbf{T}$,

$$\mathbf{T} = \begin{bmatrix} b_1 & c_1 & & & 0 \\ a_1 & b_2 & c_2 & & \\ & \ddots & \ddots & \ddots & \\ & & a_{n-2} & b_{n-1} & c_{n-1} \\ 0 & & & a_{n-1} & b_n \end{bmatrix}, \tag{A.19}$$

and we remember that the element τ_{ij} of the inverse matrix $\mathbf{T}^{-1}$ is defined as follows

$$\tau_{ij} = \begin{cases} \dfrac{(-1)^{i+j}\, c_i c_{i+1} \dots c_{j-1} \theta_{i-1} \phi_{j+1}}{\theta_n} & \text{for} \quad i < j, \\ \dfrac{\theta_{i-1}\phi_{i+1}}{\theta_n} & \text{for} \quad i = j, \\ \dfrac{(-1)^{i+j}\, a_{j+1} a_{j+2} \dots a_i \theta_{j-1} \phi_{i+1}}{\theta_n} & \text{for} \quad i > j, \end{cases} \tag{A.20}$$

where we have introduced the two sequences θ_i and ϕ_i for $i = 1 \dots n$

$$\theta_i : \begin{cases} \theta_i = b_i \theta_{i-1} - a_i c_{i-1} \theta_{i-2}, \\ \theta_{-1} = 0, \\ \theta_0 = 1, \end{cases}$$
$$\phi_i : \begin{cases} \phi_i = b_i \phi_{i+1} - c_i a_{i+1} \phi_{i+2}, \\ \phi_{n+2} = 0, \\ \phi_{n+1} = 1. \end{cases} \tag{A.21}$$

We remark that the first sequence is defined by a progressive recursion (i from 1 to n), and the second one by a regressive recursion (i from n to 1). Moreover, we have that $\phi_1 = \theta_n = \det \mathbf{T}$. In our system the matrix $\mathbf{A}$ can be subdivided in two blocks (corresponding to intact and broken regions), as follows

$$\mathbf{A} = \left[\begin{array}{ccccccccc} 2+\alpha & -1 & & & & & & & 0 \\ -1 & 2+\alpha & -1 & & & & & & \\ & \ddots & \ddots & \ddots & & & & & \\ & & -1 & 2+\alpha & -1 & & & & \\ \hline & & & -1 & 2 & -1 & & & \\ & & & & \ddots & \ddots & \ddots & & \\ & & & & & -1 & 2 & -1 & \\ 0 & & & & & & -1 & 2 & \end{array}\right], \tag{A.22}$$

where $\alpha = 1/n^2 v^2$. The broken part of the system is represented by the lower part of matrix $\mathbf{A}$. It is evident that we have $a_i = c_i = -1$, while b_i is given by

$$b_i = \begin{cases} 2+\alpha & \text{for} \quad i \le p, \\ 2 & \text{for} \quad i > p, \end{cases} \tag{A.23}$$

where p is the number of unbroken elements. It follows that the ijth element of the inverse matrix $\mathbf{A}^{-1}$, in our case, is obtained as

$$\mathcal{A}^{-1}_{ij} = \begin{cases} \dfrac{\theta_{i-1}\phi_{j+1}}{\theta_n} & \text{for} \quad i < j, \\ \dfrac{\theta_{i-1}\phi_{i+1}}{\theta_n} & \text{for} \quad i = j, \\ \dfrac{\theta_{j-1}\phi_{i+1}}{\theta_n} & \text{for} \quad i > j, \end{cases} \tag{A.24}$$

where we have different expressions for the sequences θ_i and ϕ_i, depending on the region (intact or broken) under consideration. Specifically, for the intact part ($i \leq p$), considering the conditions given in Eq. (A.21), we have

$$\begin{cases} \theta_i = (2+\alpha)\,\theta_{i-1} - \theta_{i-2} \\ \theta_0 = 1 \\ \theta_{-1} = 0 \end{cases} \qquad \text{for} \quad i \leq p. \tag{A.25}$$

The solutions of this difference equation exhibit an exponential form $\theta_i \sim \Lambda^i$, which, when substituted into the equation, delivers

$$\Lambda^i = (2+\alpha)\Lambda^{i-1} - \Lambda^{i-2}, \quad \text{or} \quad \Lambda^2 - (2+\alpha)\Lambda + 1 = 0. \tag{A.26}$$

The solution for θ_i is then a linear combination $\theta_i = A\Lambda_1^i + B\Lambda_2^i$, where Λ_1 and Λ_2 are the two roots of Eq. (A.26), and where the two constants A and B must be evaluated considering the conditions for θ_0 and θ_{-1}. Eventually, θ_i assumes the compact form

$$\theta_i = \Theta\,(i+1) \qquad \text{for} \quad i \leq p, \tag{A.27}$$

where we have introduced the function $\Theta(z)$ as

$$\Theta\,(z) = \frac{1}{\sqrt{\alpha^2+4\alpha}} \left[\left(\frac{2+\alpha+\sqrt{\alpha^2+4\alpha}}{2} \right)^z - \left(\frac{2+\alpha-\sqrt{\alpha^2+4\alpha}}{2} \right)^z \right]. \tag{A.28}$$

Since $\Lambda_1\Lambda_2 = 1$, we can observe that $\Theta\,(-z) = -\Theta\,(z)$. Following the same approach, we can determine the solution for θ_i in the broken region of the system ($i > p$). In this case, the system to be solved reads

$$\begin{cases} \theta_i = 2\theta_{i-1} - \theta_{i-2}, \\ \theta_p = \Theta\,(p+1)\,, \\ \theta_{p-1} = \Theta\,(p)\,, \end{cases} \qquad \text{for} \quad i > p \tag{A.29}$$

where the two conditions ensure the continuity of θ_i between the intact and broken regions. We remark that in this case the solution is $\theta_i = C + Di$. By applying the initial conditions, we obtain

$$\theta_i = (p-i)\Theta\,(p) - (p-i-1)\,\Theta\,(p+1)\,, \qquad \text{for} \quad i > p. \tag{A.30}$$

Summing up, the sequence θ_i can be rewritten as

$$\theta_i = \begin{cases} \Theta\,(i+1) & \text{for} \quad i \leq p, \\ (p-i)\,\Theta\,(p) - (p-i-1)\,\Theta\,(p+1) & \text{for} \quad i > p. \end{cases} \tag{A.31}$$

For the calculation of the sequence ϕ_i, we proceed using a similar method. The difference equations to solve for the intact and broken regions of the system are

$$\begin{cases} \phi_i = 2\phi_{i+1} - \phi_{i+2} \\ \phi_{n+1} = 1 \\ \phi_{n+2} = 0 \end{cases} \qquad \text{for} \quad i > p, \tag{A.32}$$

$$\begin{cases} \phi_i = (2+\alpha)\,\phi_{i+1} - \phi_{i+2} \\ \phi_{p+1} = n-p+1 \\ \phi_{p+2} = n-p \end{cases} \qquad \text{for} \quad i \leq p, \tag{A.33}$$

where the boundary conditions follow from Eq. (A.21) in the broken region, and from continuity arguments in the unbroken one. The solution can be written as follows

$$\phi_i = \begin{cases} (n-p)\Theta\,(i-p-1) - (n-p+1)\,\Theta\,(i-p-2) & \text{for} \quad i \leq p, \\ n+2-i & \text{for} \quad i > p. \end{cases} \tag{A.34}$$

The sequences θ_i and ϕ_i give the ijth element of the inverse $\mathbf{A}^{-1}$, as stated in Eq. (A.24). Hence, we can deduce the expression for the ijth element of the inverse of $\mathbf{B}$ through Eq. (A.18). Moreover, we remember that $\phi_1 = \theta_n = \det \mathbf{A}$.

A.2. Asymptotic behavior for $n \to \infty$ of the minimized energy

We can now estimate the asymptotic behavior for $n \to \infty$ of the minimized energy $\tilde{g}_e$ defined in Eq. (15). For this purpose, we use Eqs. (A.1) and (A.18), and we obtain

$$\begin{aligned} n\tilde{g}_e(\chi) &= -\frac{1}{2}\frac{\lambda^2}{n^2\nu^2}\left[\mathbf{A} - \mathbf{e_1}\otimes\mathbf{e_1} - \mathbf{e_n}\otimes\mathbf{e_n}\right]^{-1}\mathbf{1}\cdot\mathbf{1} + \frac{1}{2}\chi\cdot\mathbf{1} \\ &= -\frac{1}{2}\frac{\lambda^2}{n^2\nu^2}\left[\mathbf{A}^{-1}\mathbf{1}\cdot\mathbf{1} + \frac{\left(1-w_n\right)\Sigma_q^2 + \left(1-q_1\right)\Sigma_w^2 + 2\Sigma_q\Sigma_w q_n}{\left(1-w_n\right)\left(1-q_1\right) - q_n^2}\right] + \frac{1}{2}(n-p), \end{aligned} \tag{A.35}$$

where we have used the symbols Σ_q and Σ_w to indicate the sums

$$\Sigma_q = \sum_{i=1}^{n} q_i = \boldsymbol{q}\cdot\mathbf{1}, \quad \Sigma_w = \sum_{i=1}^{n} w_i = \boldsymbol{w}\cdot\mathbf{1}. \tag{A.36}$$

It is useful to introduce the parameter ξ, representing the broken fraction of the system. If $n-p$ is the number of broken units, ξ is defined as $(n-p)/n$ with $n \to \infty$. Hence, from now on, we will substitute the number of unbroken units p with $n(1-\xi)$. For example, we can study the asymptotic behavior of the function $\Theta(p) = \Theta(n(1-\xi))$, defined in Eq. (A.28)

$$\Theta\left(n(1-\xi)\right) = \frac{1}{\sqrt{\alpha^2+4\alpha}}\left[\left(\frac{2+\alpha+\sqrt{\alpha^2+4\alpha}}{2}\right)^{n(1-\xi)} - \left(\frac{2+\alpha-\sqrt{\alpha^2+4\alpha}}{2}\right)^{n(1-\xi)}\right]. \tag{A.37}$$

Recalling that $\alpha = 1/n^2\nu^2$, the asymptotic value of the square root reads

$$\frac{1}{\sqrt{\alpha^2+4\alpha}} = \frac{1}{\sqrt{\frac{1}{n^4\nu^4} + \frac{4}{n^2\nu^2}}} \underset{n\to\infty}{\sim} \frac{1}{\sqrt{\frac{4}{n^2\nu^2}}} = \frac{n\nu}{2} \tag{A.38}$$

In the continuum limit, $\Theta(n(1-\xi))$ becomes

$$\begin{aligned} \Theta\left(n(1-\xi)\right) &\underset{n\to\infty}{\sim} \frac{n\nu}{2}\left[\left(1+\frac{1}{2n^2\nu^2}+\frac{1}{n\nu}\right)^{n(1-\xi)} - \left(1+\frac{1}{2n^2\nu^2}-\frac{1}{n\nu}\right)^{n(1-\xi)}\right] \\ &\underset{n\to\infty}{\sim} \frac{n\nu}{2}\left[\left(1+\frac{1}{n\nu}\right)^{n(1-\xi)} - \left(1-\frac{1}{n\nu}\right)^{n(1-\xi)}\right] \\ &\underset{n\to\infty}{\sim} \frac{n\nu}{2}\left[\exp\left(\frac{1-\xi}{\nu}\right) - \exp\left(-\frac{1-\xi}{\nu}\right)\right] = n\nu\sinh\left(\frac{1-\xi}{\nu}\right). \end{aligned} \tag{A.39}$$

We can calculate the asymptotic behavior of θ_n by considering Eq. (A.31), as follows

$$\begin{aligned} \theta_n &= -n\xi\Theta(n(1-\xi)) + (n\xi+1)\,\Theta(n(1-\xi)+1) \\ &= \Theta(n(1-\xi)+1) + n\xi\left[\Theta(n(1-\xi)+1) - \Theta(n(1-\xi))\right] \\ &= \Theta(n(1-\xi)+1) + \xi\frac{\Theta\left(n\left(1-\xi+\frac{1}{n}\right)\right) - \Theta(n(1-\xi))}{\frac{1}{n}}. \end{aligned} \tag{A.40}$$

We observe that when $n \to \infty$, the asymptotic behavior of the first term $\Theta(n(1-\xi)+1)$ is again $n\nu\sinh[(1-\xi)/\nu]$, while the second term can be seen as a derivative of $\Theta(n(1-\xi))$ with respect to $1-\xi$. Therefore, we eventually obtain

$$\theta_n \underset{n\to\infty}{\sim} n\nu\sinh\left(\frac{1-\xi}{\nu}\right) + n\xi\cosh\left(\frac{1-\xi}{\nu}\right). \tag{A.41}$$

Following the same approach, we can write the asymptotic behavior of q_1, which corresponds to the first element $\mathcal{A}_{11}^{-1}$ of the inverse matrix of $\mathcal{A}$

$$q_1 = \mathcal{A}_{11}^{-1} = \frac{\theta_0\phi_2}{\theta_n} = \frac{\phi_2}{\theta_n} = \frac{n\xi\Theta(1-n(1-\xi)) - (n\xi+1)\Theta(-n(1-\xi))}{-n\xi\Theta(n(1-\xi)) + (n\xi+1)\Theta(n(1-\xi)+1)}, \tag{A.42}$$

where we have used the expression for ϕ_2 within the intact region since we assume that the fracture propagates from the left to the right. Thus, the term $\mathcal{A}_{11}^{-1}$ necessarily corresponds to an intact element (otherwise $\mathbf{A}$ would be singular). It is not difficult to see that $q_1 \underset{n\to\infty}{\sim} 1$. Moreover, we are interested in the asymptotic behavior of $(1-q_1)$, that reads

$$(1-q_1) \underset{n\to\infty}{\sim} \frac{\frac{\xi}{\nu}\sinh\left(\frac{1-\xi}{\nu}\right) + \cosh\left(\frac{1-\xi}{\nu}\right)}{n\nu\sinh\left(\frac{1-\xi}{\nu}\right) + n\xi\cosh\left(\frac{1-\xi}{\nu}\right)}. \tag{A.43}$$

Similarly, for w_n we have the expression

$$w_n = \mathcal{A}_{nn}^{-1} = \frac{\theta_{n-1}\phi_{n+1}}{\theta_n} = \frac{\theta_{n-1}}{\theta_n}, \tag{A.44}$$

which can be used to determine the asymptotic behavior of $(1-w_n)$. The result follows

$$(1-w_n) \underset{n\to\infty}{\sim} \frac{\cosh\left(\frac{1-\xi}{\nu}\right)}{n\nu\sinh\left(\frac{1-\xi}{\nu}\right)+n\xi\cosh\left(\frac{1-\xi}{\nu}\right)}. \tag{A.45}$$

The term q_n, in the limit for $n\to\infty$, is simply obtained as

$$q_n = \mathcal{A}^{-1}_{1n} = \frac{\theta_0\phi_{n+1}}{\theta_n} = \frac{1}{\theta_n} \underset{n\to\infty}{\sim} \frac{1}{n\nu\sinh\left(\frac{1-\xi}{\nu}\right)+n\xi\cosh\left(\frac{1-\xi}{\nu}\right)}. \tag{A.46}$$

By using the last achievements, we can calculate the asymptotic value of the denominator in Eq. (A.35), finally obtaining

$$(1-q_1)(1-w_n)-q_n^2 \underset{n\to\infty}{\sim} \frac{\sinh\left(\frac{1-\xi}{\nu}\right)}{n^2\nu\left[\xi\cosh\left(\frac{1-\xi}{\nu}\right)+\nu\sinh\left(\frac{1-\xi}{\nu}\right)\right]}. \tag{A.47}$$

We can now determine the asymptotic behavior of Σ_q, which can be written as

$$\Sigma_q = \sum_{i=1}^{n} q_i = \sum_{i=1}^{n} \mathcal{A}^{-1}_{1i} = \sum_{i=1}^{n} \frac{\theta_0\phi_{i+1}}{\theta_n} = \sum_{i=1}^{n} \frac{\phi_{i+1}}{\theta_n}, \tag{A.48}$$

where ϕ_{i+1} is given by

$$\phi_{i+1} = \begin{cases} n\xi\Theta(i-n(1-\xi)) - (n\xi+1)\,\Theta(i-n(1-\xi)-1) & \text{for} \quad i < n(1-\xi), \\ n+1-i & \text{for} \quad i \geq n(1-\xi). \end{cases} \tag{A.49}$$

Therefore we can write Σ_q as

$$\Sigma_q = \sum_{i=1}^{n(1-\xi)-1} \frac{n\xi\Theta(i-n(1-\xi)) - (n\xi+1)\,\Theta(i-n(1-\xi)-1)}{\theta_n} + \sum_{i=n(1-\xi)}^{n} \frac{n-i+1}{\theta_n}. \tag{A.50}$$

We observe that for $m \leq n$, we have

$$\sum_{j=m}^{n} j = \frac{n(n+1)}{2} - \frac{m(m-1)}{2}, \tag{A.51}$$

so that the second term of Eq. (A.50) can be elaborated as follows

$$\sum_{i=n(1-\xi)}^{n} \frac{n-i+1}{\theta_n} = \sum_{i=n(1-\xi)}^{n} \frac{n+1}{\theta_n} - \sum_{i=n(1-\xi)}^{n} \frac{i}{\theta_n} \underset{n\to\infty}{\sim} \frac{n^2\xi^2}{2\theta_n}. \tag{A.52}$$

On the other side, the asymptotic behavior of the numerator of first term of Eq. (A.50) is

$$\begin{aligned} &\sum_{i=1}^{n(1-\xi)-1} \left[n\xi\Theta(i-n(1-\xi)) - (n\xi+1)\,\Theta(i-n(1-\xi)-1)\right] \\ &\underset{n\to\infty}{\sim} n^2 \int_0^{1-\xi} \left[\xi\cosh\left(\frac{x-1+\xi}{\nu}\right) - \nu\sinh\left(\frac{x-1+\xi}{\nu}\right)\right] dx \\ &\underset{n\to\infty}{\sim} n^2\nu\left[\xi\sinh\left(\frac{1-\xi}{\nu}\right) + \nu\cosh\left(\frac{1-\xi}{\nu}\right) - \nu\right]. \end{aligned} \tag{A.53}$$

Recalling the results obtained in Eqs. (A.41) and (A.52), we can write the asymptotic value of Σ_q in the following final form

$$\Sigma_q \underset{n\to\infty}{\sim} n\frac{\nu\left[\xi\sinh\left(\frac{1-\xi}{\nu}\right) + \nu\cosh\left(\frac{1-\xi}{\nu}\right) - \nu\right] + \frac{1}{2}\xi^2}{\nu\sinh\left(\frac{1-\xi}{\nu}\right) + \xi\cosh\left(\frac{1-\xi}{\nu}\right)}. \tag{A.54}$$

Following a similar procedure, we calculate the asymptotic behavior for the sum Σ_w and we get

$$\begin{aligned} \Sigma_w &= \sum_{i=1}^{n} w_i = \sum_{i=1}^{n} \mathcal{A}^{-1}_{in} = \frac{\theta_{i-1}\phi_{n+1}}{\theta_n} = \sum_{i=1}^{n} \frac{\theta_{i-1}}{\theta_n} \\ &\underset{n\to\infty}{\sim} n\frac{\nu^2\cosh\left(\frac{1-\xi}{\nu}\right) - \nu^2 + \xi\nu\sinh\left(\frac{1-\xi}{\nu}\right) + \frac{\xi^2}{2}\cosh\left(\frac{1-\xi}{\nu}\right)}{\nu\sinh\left(\frac{1-\xi}{\nu}\right) + \xi\cosh\left(\frac{1-\xi}{\nu}\right)}. \end{aligned} \tag{A.55}$$

The last term that we have to evaluate is $\mathbf{A}^{-1}\mathbf{1}\cdot\mathbf{1}$. It corresponds to the sum of all elements of the matrix $\mathbf{A}^{-1}$, which can be decomposed into the sum of the terms on the main diagonal and the sum of the terms out of diagonal, as follows

$$\begin{aligned}\mathbf{A}^{-1}\mathbf{1}\cdot\mathbf{1} &= \sum_{i=1}^{n}\sum_{j=1}^{n}\mathcal{A}^{-1}_{ij} = \sum_{i=1}^{n}\mathcal{A}^{-1}_{ii} + 2\sum_{i=1}^{n-1}\sum_{j=i+1}^{n}\mathcal{A}^{-1}_{ij}\\ &= \frac{1}{\theta_n}\sum_{i=1}^{n}\theta_{i-1}\phi_{i+1} + \frac{2}{\theta_n}\sum_{i=1}^{n-1}\sum_{j=i+1}^{n}\theta_{i-1}\phi_{j+1} = \mathcal{S}_1 + \mathcal{S}_2.\end{aligned} \tag{A.56}$$

Notice that both sequences θ_i and ϕ_i are given in Eqs. (A.31) and (A.34). Therefore, we have to consider different sums for each intact or broken region. For instance, for the sum $\mathcal{S}_1$ of the terms on the diagonal, we split the result into two terms

$$\mathcal{S}_1\theta_n = \sum_{i=1}^{n(1-\xi)}\theta_{i-1}\phi_{i+1} + \sum_{i=n(1-\xi)+1}^{n}\theta_{i-1}\phi_{i+1}. \tag{A.57}$$

On the other side, for the sum $\mathcal{S}_2$ of the terms out of diagonal, we split the result into three terms

$$\frac{\mathcal{S}_2\theta_n}{2} = \sum_{i=1}^{n(1-\xi)-1}\sum_{j=i+1}^{n(1-\xi)}\theta_{i-1}\phi_{j+1} + \sum_{i=1}^{n(1-\xi)-1}\sum_{j=n(1-\xi)+1}^{n}\theta_{i-1}\phi_{j+1} + \sum_{i=n(1-\xi)}^{n-1}\sum_{j=i+1}^{n}\theta_{i-1}\phi_{j+1}. \tag{A.58}$$

After performing very long but straightforward calculations, we observe that in the limit as $n\to\infty$, the term $\mathcal{S}_1$ can be neglected since it scales as n^2, whereas $\mathcal{S}_2$ scales as n^3. In the end, we obtain the asymptotic expression for $\mathbf{A}^{-1}\mathbf{1}\cdot\mathbf{1}$, which reads

$$\mathbf{A}^{-1}\mathbf{1}\cdot\mathbf{1} \underset{n\to\infty}{\sim} \mathcal{S}_2 \underset{n\to\infty}{\sim} n^3\frac{\mathcal{R}}{\nu\sinh\left(\frac{1-\xi}{\nu}\right)+\xi\cosh\left(\frac{1-\xi}{\nu}\right)}, \tag{A.59}$$

where

$$\begin{aligned}\mathcal{R} =& \nu^2(2\nu^2-\xi^2)\left[1-\cosh\left(\frac{1-\xi}{\nu}\right)\right] + \nu^2\xi(1-\xi)\cosh\left(\frac{1-\xi}{\nu}\right)\\ &+ \frac{1}{12}\xi^4\cosh\left(\frac{1-\xi}{\nu}\right) + (1-2\xi)\nu^3\sinh\left(\frac{1-\xi}{\nu}\right) + \frac{1}{3}\nu\xi^3\sinh\left(\frac{1-\xi}{\nu}\right).\end{aligned} \tag{A.60}$$

From results obtained in Eqs. (A.41), (A.43), (A.45), (A.46), (A.47), (A.54), (A.55), and (A.59), we can finally calculate the asymptotic behavior for $n\to\infty$ of the energy in Eq. (A.35) as

$$\tilde{g}_e(\xi) = -\frac{1}{2}\lambda^2 - \frac{1}{2}\frac{\lambda^2}{\nu^2}\xi\left[\nu^2 + \nu\xi\coth\left(\frac{1-\xi}{\nu}\right) + \frac{\xi^2}{3}\right] + \frac{1}{2}\xi, \tag{A.61}$$

which corresponds to Eq. (16) of the main text. If we consider the term

$$\mathbf{A}^{-1}\mathbf{1}\cdot\mathbf{1} + \frac{\left(1-w_n\right)\Sigma_q^2 + \left(1-q_1\right)\Sigma_w^2 + 2\Sigma_q\Sigma_w q_n}{\left(1-w_n\right)\left(1-q_1\right) - q_n^2}, \tag{A.62}$$

we easily deduce that it scales as n^3, and therefore, the energy defined in Eq. (A.35) remains finite in the continuum limit, that is for $n\to\infty$.

To conclude, we emphasize that this result was found in two ways: in this Appendix the minimized discrete energy was considered and the limit for $n\to\infty$ was carried out. In the main text we reobtained the same result by first applying the limit for $n\to\infty$ to the not-yet-minimized energy, and then minimization was carried out by variational calculus. The coincidence of the two results is consistent with the Γ-convergence, as already mentioned in the main text.

A.3. Asymptotic behavior of $\det\mathbf{B}$ *as* $n\to\infty$

To evaluate the asymptotic behavior of $\det\mathbf{B}$ we consider again Eq. (A.1). In general, it is possible to prove that for a generic non-singular matrix $\mathbf{M}$, a vector $\mathbf{m}$, and a scalar quantity β, the determinant of $\mathbf{M}+\beta\mathbf{m}\otimes\mathbf{m}$ is given by

$$\det\left(\mathbf{M}+\beta\mathbf{m}\otimes\mathbf{m}\right) = \det\mathbf{M}\left(1+\beta\mathbf{m}\cdot\mathbf{m}\right). \tag{A.63}$$

Then, to obtain the determinant of $\mathbf{B}$, we apply this formula (with $\beta=-1$) twice to Eq. (A.1)

$$\begin{aligned}\det\mathbf{B} &= \left(n^2\nu^2\right)^n\det\left(\mathbf{A}-\mathbf{e}_1\otimes\mathbf{e}_1-\mathbf{e}_n\otimes\mathbf{e}_n\right)\\ &= \left(n^2\nu^2\right)^n\left[\det\left(\mathbf{A}-\mathbf{e}_1\otimes\mathbf{e}_1\right)\right]\left[1-\left(\mathbf{A}-\mathbf{e}_1\otimes\mathbf{e}_1\right)^{-1}\mathbf{e}_n\cdot\mathbf{e}_n\right]\\ &= \left(n^2\nu^2\right)^n\det\mathbf{A}\left[1-\mathbf{A}^{-1}\mathbf{e}_1\cdot\mathbf{e}_1\right]\left[1-\left(\mathbf{A}-\mathbf{e}_1\otimes\mathbf{e}_1\right)^{-1}\mathbf{e}_n\cdot\mathbf{e}_n\right].\end{aligned} \tag{A.64}$$

From Eq. (A.6), we know that

$$\left(\mathbf{A}-\mathbf{e}_1\otimes\mathbf{e}_1\right)^{-1} = \mathbf{A}^{-1} + \frac{\mathbf{A}^{-1}\mathbf{e}_1\otimes\mathbf{e}_1\mathbf{A}^{-1}}{1-\mathbf{A}^{-1}\mathbf{e}_1\cdot\mathbf{e}_1}, \tag{A.65}$$

and then, by recalling Eqs. (A.9) and (A.13), we can write

$$\left(\mathbf{A}-\mathbf{e}_1\otimes\mathbf{e}_1\right)^{-1}\mathbf{e}_n\cdot\mathbf{e}_n=\mathbf{A}^{-1}\mathbf{e}_n\cdot\mathbf{e}_n+\frac{\mathbf{A}^{-1}\mathbf{e}_1\otimes\mathbf{e}_1\mathbf{A}^{-1}}{1-\mathbf{A}^{-1}\mathbf{e}_1\cdot\mathbf{e}_1}\mathbf{e}_n\cdot\mathbf{e}_n=w_n+\frac{q_n^2}{1-q_1}. \tag{A.66}$$

Substituting this result in Eq. (A.64), we obtain

$$\det\mathbf{B}=\left(n^2\nu^2\right)^n\det\mathbf{A}\left(1-q_1\right)\left(1-w_n-\frac{q_n^2}{1-q_1}\right)=\left(n^2\nu^2\right)^n\det\mathbf{A}\left[\left(1-w_n\right)\left(1-q_1\right)-q_n^2\right]. \tag{A.67}$$

We remember that the asymptotic value of $\left(1-w_n\right)\left(1-q_1\right)-q_n^2$ has been evaluated in Eq. (A.47). Moreover from Eq. (A.41), we deduce the behavior of $\det\mathbf{A}=\theta_n$. Finally, substituting Eqs. (A.47) and (A.41) into Eq. (A.67), we obtain the expression for $\det\mathbf{B}$ in the continuum limit

$$\det\mathbf{B}\underset{n\to\infty}{\sim}\left(n^2\nu^2\right)^n\frac{\sinh\left(\frac{1-\xi}{\nu}\right)}{n\nu}, \tag{A.68}$$

useful to develop the partition function within the Gibbs ensemble.

Data availability

No data was used for the research described in the article.

References

Alava, M.J., Nukala, P.K., Zapperi, S., 2006. Statistical models of fracture. Adv. Phys. 55, 349–476.

Barenblatt, G.I., 1959. The formation of equilibrium cracks during brittle fracture. General ideas and hypotheses. Axially-symmetric cracks. J. Appl. Math. Mech. 23, 622–636.

Barenblatt, G.I., 1962. The mathematical theory of equilibrium cracks in brittle fracture. Adv. Appl. Mech. 7, 55–129.

Bazant, Z.P., Kazemi, M.T., 1990. Determination of fracture energy, process zone longth and brittleness number from size effect, with application to rock and conerete. Int. J. Fract. 44, 111–131.

Belhouari, M., Benkheira, A., Madani, K., Campilho, R.D.S.G., Gong, X.L., 2023. Effect of temperature on the energy release rate variation in repaired laminate composites. J. Fail. Anal. Prev. 23, 420–435.

Bellino, L., Florio, G., Giordano, S., Puglisi, G., 2020. On the competition between interface energy and temperature in phase transition phenomena. Appl. Eng. Sci. 2, 100009.

Bellino, L., Florio, G., Puglisi, G., 2019. The influence of device handles in single-molecule experiments. Soft Matter 15, 8680–8690.

Benedito, M., Giordano, S., 2018a. Thermodynamics of small systems with conformational transitions: The case of two-state freely jointed chains with extensible units. J. Chem. Phys. 149, 054901.

Benedito, M., Giordano, S., 2018b. Isotensional and isometric force–extension response of chains with bistable units and Ising interactions. Phys. Rev. E 98, 052146.

Bitzek, E., Kermode, J.R., Gumbsch, P., 2015. Atomistic aspects of fracture. Int. J. Fract. 191, 13–30.

Bleha, T., Cifra, P., 2022. Energy/entropy partition of force at dna stretching. Biopolymers 113, e23487.

Blom, K., Godec, A., 2021. Criticality in cell adhesion. Phys. Rev. X 11, 031067.

Blumberg Selinger, R.L., Wang, Z.G., Gelbart, W.M., 1991. Effect of temperature and small-scale defects on the strength of solids. J. Chem. Phys. 95, 9128–9141.

Bonilla, L., Carpio, A., Prados, A., 2015. Theory of force–extension curves for modular proteins and DNA hairpins. Phys. Rev. E 91, 052712.

Borja da Rocha, H., Truskinovsky, L., 2022. Mean field fracture in disordered solids: Statistics of fluctuations. J. Mech. Phys. Solids 158, 104646.

Bourdin, B., 2007. Numerical implementation of the variational formulation for quasi-static brittle fracture. Interfaces Free Bound. 9, 411–430.

Bourdin, B., Francfort, G.A., Marigo, J.J., 2000. Numerical experiments in revisited brittle fracture. J. Mech. Phys. Solids 48, 797–826.

Braides, A., 2002. Gamma-Convergence for Beginners. Vol. 22, Clarendon Press.

Buche, M., Grutzik, S., 2024. Statistical mechanical model for crack growth. Phys. Rev. E 109, 015001.

Buche, M., Silberstein, M., 2020. Statistical mechanical constitutive theory of polymer networks: The inextricable links between distribution, behavior, and ensemble. Phys. Rev. E 102, 012501.

Burdekin, F.M., Dawes, M.G., 1971. Practical use of linear elastic and yielding fracture mechanics with particular reference to pressure vessels. In: Proc. of the Institute of Mechanical Engineers Conference. 1971, pp. 28–37.

Cadelano, E., Palla, P.L., Giordano, S., Colombo, L., 2009. Nonlinear elasticity of monolayer graphene. Phys. Rev. Lett. 102, 235502.

Cannizzo, A., Bellino, L., Florio, G., Giordano, S., Puglisi, G., 2022. Thermal control of nucleation and propagation transition stresses in discrete lattices with non-local interactions and non-convex energy. Eur. Phys. J. Plus 137, 569.

Cannizzo, A., Florio, G., Puglisi, G., Giordano, S., 2021. Temperature controlled decohesion regimes of an elastic chain adhering to a fixed substrate by softening and breakable bonds. J. Phys. A 54, 445001.

Cannizzo, A., Giordano, S., 2023. Thermal effects on fracture and the brittle-to-ductile transition. Phys. Rev. E 107, 035001.

Cannizzo, A., Giordano, S., 2024. Statistical mechanics approaches for studying temperature and rate effects in multistable systems. Symmetry 16, 632.

Caruel, M., Truskinovsky, L., 2016. Statistical mechanics of the huxley-simmons model. Phys. Rev. E 93, 062407.

Caruel, M., Truskinovsky, L., 2018. Physics of muscle contraction. Rep. Progr. Phys. 81, 036602.

Charmet, J., Roux, S., Guyon, E., 1990. Disorder and Fracture. Vol. 235, Springer Science & Business Media, Heidelberg.

Cheng, T., Fang, D., Yang, Y., 2017. The temperature-dependent surface energy of ceramic single crystals. J. Am. Ceram. Soc. 100, 1598–1605.

Creton, C., Ciccotti, M., 2016. Fracture and adhesion of soft materials: a review. Rep. Progr. Phys. 79.

Dal Maso, G., 2012. An Introduction To Γ-Convergence. Vol. 8, Springer Science & Business Media, Heidelberg.

De Giorgi, E., Carriero, M., Leaci, A., 1989. Existence theorem for a minimum problem with free discontinuity set. Arch. Ration. Mech. Anal. 108, 195–218.

De Tommasi, D., Millardi, N., Puglisi, G., Saccomandi, G., 2013. An energetic model for macromolecules unfolding in stretching experiments. J. R. Soc. Interface 10, 20130651.

Del Piero, G., 2013. A variational approach to fracture and other inelastic phenomena. J. Elasticity 112, 3–77.

Del Piero, G., Truskinovsky, L., 2001. Macro-and micro-cracking in one-dimensional elasticity. Int. J. Solids Struct. 38, 1135–1148.

Dillard, D.A., Mukherjee, B., Karnal, P., Batra, R.C., Frechette, J., 2018. A review of Winkler's foundation and its profound influence on adhesion and soft matter applications. Soft Matter 14, 3669–3683.
Dimitrov, D., Klushin, L., Skvortsov, A., Milchev, A., Binder, K., 2009. The escape transition of a polymer: A unique case of non-equivalence between statistical ensembles. Eur. Phys. J. E 29, 9–25.
Dormieux, L., Kondo, D., 2016. Micromechanics of Fracture and Damage. John Wiley & Sons.
Dudko, O., 2016. Decoding the mechanical fingerprints of biomolecules. Q. Rev. Biophys. 49, e3.
Dugdale, D.S., 1960. Yielding of steel sheets containing slits. J. Mech. Phys. Solids 8, 100–104.
Dutler, N., Nejati, M., Valley, B., Amann, F., Molinari, G., 2018. On the link between fracture toughness, tensile strength, and fracture process zone in anisotropic rocks. Eng. Fract. Mech. 201, 56–79.
Dutta, S., Benetatos, P., 2018. Inequivalence of fixed-force and fixed-extension statistical ensembles for a flexible polymer tethered to a planar substrate. Soft Matter 14, 6857–6866.
Dutta, S., Benetatos, P., 2019. Statistical ensemble inequivalence for flexible polymers under confinement in various geometries. Soft Matter 16, 2114–2127.
Eftis, J., Liebowitz, H., 1976. On surface energy and the continuum thermodynamics of brittle fracture. Eng. Fract. Mech. 8, 459–485.
Elliott, H., 1947. An analysis of the conditions for rupture due to griffith cracks. Proc. Phys. Soc. 59, 208–223.
Eshelby, J.D., 1951. The force on an elastic singularity. Philos. Trans. R. Soc. Lond. Ser. A, Math. Phys. Sci. 244, 87–112.
Esterling, D.M., Swaroop, A., 1979. Interatomic potentials from experimental phonon spectra i. prototypes. Phys. Status Solidi (B) 96, 401–411.
Estevez, R., Tijssens, M., Van der Giessen, E., 2000. Modeling of the competition between shear yielding and crazing in glassy polymers. J. Mech. Phys. Solids 48, 2585–2617.
Florio, G., Puglisi, G., 2019. Unveiling the influence of device stiffness in single macromolecule unfolding. Sci. Rep. 9, 4997.
Florio, G., Puglisi, G., 2023. A predictive model for the thermomechanical melting transition of double stranded DNA. Acta Biomater. 157, 225–235.
Florio, G., Puglisi, G., Giordano, S., 2020. Role of temperature in the decohesion of an elastic chain tethered to a substrate by onsite breakable links. Phys. Rev. Res. 2, 033227.
Florio, G., Pugno, N.M., Puglisi, G., 2024. Temperature, elasticity, and size effects in fibrillar biological adhesion. Submitted for publication.
Francfort, G.A., Marigo, J.J., 1998. Revisiting brittle fracture as an energy minimization problem. J. Mech. Phys. Solids 46, 1319–1342.
Frenkel, D., Smit, B., 2023. UnderstandIng Molecular Simulation: From Algorithms To Applications. Elsevier.
Gali, A., George, E.P., 2013. Tensile properties of high-and medium-entropy alloys. Intermetallics 39, 74–78.
Gamboa-Suárez, A., Seuret-Hernández, H.Y., Leyssale, J.M., 2022. Mechanical properties of pristine and nanocrystalline graphene up to ultra-high temperatures. Carbon Trends 9, 100197.
Ganz, E., Ganz, A.B., Yang, L.M., Dornfeld, M., 2017. The initial stages of melting of graphene between 4000 k and 6000 k. Phys. Chem. Chem. Phys. 19, 3756–3762.
Gent, A., Petrich, R., 1969. Adhesion of viscoelastic materials to rigid substrates. Proc. R. Soc. A 310, 433–448.
Gibbs, J.W., 1902. Elementary Principles in Statistical Mechanics: Developed with Especial Reference To the Rational Foundations of Thermodynamics. C. Scribner's sons.
Giordano, S., 2017. Spin variable approach for the statistical mechanics of folding and unfolding chains. Soft Matter 13, 6877–6893.
Giordano, S., 2022. Statistical mechanics of rate-independent stick–slip on a corrugated surface composed of parabolic wells. Contin. Mech. Thermodyn. 34, 1343–1372.
Giordano, S., 2023. Temperature dependent model for the quasistatic stick–slip process on a soft substrate. Soft Matter 19, 1813.
Giordano, S., Cleri, F., Blossey, R., 2023. On the one-dimensional transition state theory and the relation between statistical and deterministic oscillation frequencies of anharmonic energy wells. Ann. Phys. (Berlin) 2023, 2300294.
Giordano, S., Colombo, L., 2007a. Effects of the orientational distribution of cracks in solids. Phys. Rev. Lett. 98, 055503.
Giordano, S., Colombo, L., 2007b. Effects of the orientational distribution of cracks in isotropic solids. Eng. Fract. Mech. 74, 1983–2003.
Giordano, S., Colombo, L., 2008. Elastic properties of solids containing elliptic cracks. Phys. Rev. B 77, 054106.
Giordano, S., Mattoni, A., Colombo, L., 2010. Brittle fracture: from elasticity theory to atomistic simulations. Rev. Comput. Chem. 27, 1–83.
Griffith, A.A., 1921. The phenomena of rupture and flow in solids. Philos. Transl. R. Soc. Lond. 221, 163–198.
Guarino, A., Ciliberto, S., 2011. Thermally activated fracture of porous media. Eur. Phys. J. B 83, 215.
Guarino, A., Vanel, L., Scorretti, R., Ciliberto, S., 2006. The cooperative effect of load and disorder in thermally activated rupture of a two-dimensional random fuse network. J. Stat. Mech. 2006, P06020.
Gumbsch, P., Zhou, S., Holian, B., 1997. Molecular dynamics investigation of dynamic crack stability. Phys. Rev. B 55, 3445–3455.
Herrmann, H.J., Roux, S., 1990. Modelization of fracture in disordered systems. In: Herrmann, H.J., Roux, S. (Eds.), Statistical Models for the Fracture of Disordered Media. Elsevier, pp. 159–188.
Hillerborg, A., 1983. Analysis of one single crack. In: Wittmann, F.H. (Ed.), Fracture Mechanics of Concrete (Developments in Civil Engineering). Elsevier, pp. 223–249.
Hillerborg, A., Modéer, M., Petersson, P.E., 1976. Analysis of crack formation and crack growth in concrete by means of fracture mechanics and finite elements. Cem. Concr. Res. 6, 773–781.
Hilton, P.D., Hutchinson, J.W., 1971. Plastic intensity factors for cracked plates. Eng. Fract. Mech. 3, 435–451.
Hoagland, R.G., Hahn, G.T., Rosenfield, A.R., 1973. Influence of microstructure on fracture propagation in rock. Rock Mech. 5, 77–106.
Hui, C., Ruina, A., Long, R., Jagota, A., 2011. Cohesive zone models and fracture. J. Adhes. 87, 1–52.
Inglis, C.E., 1913. Stresses in a plate due to the presence of cracks and sharp corners. Trans. Inst. Nav. Arch. 55, 219–241.
Irwin, G.R., 1948. Fracture dynamics. In: Fracturing of Metals, A.S.M. Cleveland, 1948. pp. 147–166.
Irwin, G.R., 1957. Analysis of stresses and strains near the end of a crack traversing a plate. J. Appl. Mech. 24, 361–364.
Irwin, G.R., 1961. Plastic zone near a crack and fracture toughness. Sagamore Res. Conf. Proc. 4, 63–78.
Kachanov, M., 1992. Effective elastic properties of cracked solids: Critical review of some basic concepts. Appl. Mech. Rev. 45, 304–335.
Kachanov, M., 1993. Elastic solids with many cracks and related problems. Adv. Appl. Mech. 30, 259–445.
Kang, K., Cai, W., 2010. Size and temperature effects on the fracture mechanisms of silicon nanowires: Molecular dynamics simulations. Int. J. Plast. 26, 1387–1401.
Kawamura, H., Hatano, T., Kato, N., Biswas, S., Chakrabarti, B.K., 2012. Statistical physics of fracture, friction, and earthquakes. Rev. Modern Phys. 84, 839.
Kholtobina, A.S., Forslund, A., Ruban, A.V., Johansson, B., Skorodumova, N.V., 2023. Temperature dependence of (111) and (110) ceria surface energy. Phys. Rev. B 107, 035407.
Kirsch, E.G., 1898. Die theorie der elastizität und die bedürfnisse der festigkeitslehre. Z. Des Vereines Dtsch. Ingen. 42, 797–807.
Kitamura, K., 2008. Crack surface energy: Temperature and force dependence. Mater. Trans. 49, 643–649.
Kramer, E.J., 2005. Microscopic and molecular fundamentals of crazing. In: Crazing in Polymers. Springer, Heidelberg, pp. 1–56.
Kulakhmetova, S.A., Saraikin, V., Slepyan, L., 1984. Plane problem of a crack in a lattice. Mech. Solids 19, 102–108.
Lawn, B., 1993. Fracture of Brittle Solids. Cambridge University Press.
Lebihain, M., Ponson, L., Kondo, D., Leblond, J.B., 2021. Effective toughness of disordered brittle solids: A homogenization framework. J. Mech. Phys. Solids 153, 104463.

Levy, N., Marcal, P., Ostergren, W.J., Rice, J.R., 1971. Small scale yielding near a crack in plane strain: a finite element analysis. Int. J. Fract. Mech. 7, 143–156.
Li, M., Deng, T., Zheng, B., Zhang, Y., Liao, Y., Zhou, H., 2019. Effect of defects on the mechanical and thermal properties of graphene. Nanomaterials 9, 347.
Low, I.M., Mai, Y.W., 1989. Rate and temperature effects on crack blunting mechanisms in pure and modified epoxies. J. Mater. Sci. 24, 1634–1644.
Maddalena, F., Percivale, D., Puglisi, G., Truskinovsky, L., 2009. Mechanics of reversible unzipping. Contin. Mech. Thermodyn. 21, 251–268.
Maksimov, I., Kitamura, K., Nishioka, K., 2001. Temperature-dependent crack surface tension. Phil. Mag. Lett. 81, 547–554.
Manca, F., Giordano, S., Palla, P.L., Cleri, F., Colombo, L., 2013. Two-state theory of single-molecule stretching experiments. Phys. Rev. E 87, 032705.
Manca, F., Giordano, S., Palla, P.L., Cleri, F., Colombo, L., 2014. On the equivalence of thermodynamics ensembles for flexible polymer chains. Phys. A: Stat. Mech. Appl. 395, 154–170.
Manca, F., Giordano, S., Palla, P.L., Zucca, R., Cleri, F., Colombo, L., 2012. Elasticity of flexible and semiflexible polymers with extensible bonds in the Gibbs and Helmholtz ensembles. J. Chem. Phys. 136, 154906.
Marder, M., 1996. Statistical mechanics of cracks. Phys. Rev. E 54, 3442–3454.
Marigo, J.J., Truskinovsky, L., 2004. Initiation and propagation of fracture in the models of griffith and barenblatt. Contin. Mech. Thermodyn. 16, 391–409.
Markov, A., Abaimov, S., Sevostianov, I., Kachanov, M., Kanaun, S., Akhatov, I., 2019. The effect of multiple contacts between crack faces on crack contribution to the effective elastic properties. Int. J. Solids Struct. 163, 75–86.
Markov, A., Kanaun, S., 2017. Interactions of cracks and inclusions in homogeneous elastic media. Int. J. Fract. 206, 35–48.
Mastrangelo, C.H., 1997. Adhesion-related failure mechanisms in micromechanical devices. Tribol. Lett. 3, 223–238.
Mattoni, A., Colombo, L., Cleri, F., 2005. Atomic scale origin of crack resistance in brittle fracture. Phys. Rev. Lett. 95, 115501.
McLean, M., Mykura, H., 1966. The temperature dependence of the surface energy anisotropy of platinum. Surf. Sci. 5, 466–481.
Meurant, G., 1992. A review on the inverse of symmetric tridiagonal and block tridiagonal matrices. SIAM J. Matrix Anal. Appl. 13, 707–728.
Miehe, C., Hofacker, M., Welschinger, F., 2010. A phase field model for rate-independent crack propagation: Robust algorithmic implementation based on operator splits. Comput. Methods Appl. Mech. Engrg. 199, 2765–2778.
Miracle, D.B., Senkov, O.N., 2017. A critical review of high entropy alloys and related concepts. Acta Mater. 122, 448–511.
Mishuris, G.S., Movchan, A.B., Slepyan, L.I., 2009. Localised knife waves in a structured interface. J. Mech. Phys. Solids 57, 1958–1979.
Moore, D.E., Lockner, D., 1995. The role of microcracking in shear-fracture propagation in granite. J. Struct. Geol. 17, 95–114.
Moreno, Y., Gomez, J., Pacheco, A., 2000. Fracture and second-order phase transitions. Phys. Rev. Lett. 85, 2865–2868.
Mumford, D., Shah, J., 1989. Optimal approximations by piecewise smooth functions and associated variational problems. Comm. Pure Appl. Math. 17, 577–685.
Nitecki, S., Givli, S., 2021. The mechanical behavior of 2-d lattices with bi-stable springs. J. Mech. Phys. Solids 157, 104634.
Novozhilov, V., 1969a. On a necessary and sufficient criterion for brittle strength. J. Appl. Math. Mech. 33, 212–222.
Novozhilov, V., 1969b. On the foundations of a theory of equilibrium cracks in elastic solids. J. Appl. Math. Mech. 33, 797–812.
Öchsner, A., 2016. Continuum Damage Mechanics. Springer, Heidelberg.
Orowan, E., 1948. Fracture and strength of solids. Rep. Progr. Phys. 12, 185–232.
Paris, P.C., Sih, G.C., 1965. Stress analysis of cracks. In: Fracture Toughness Testing and Its Applications, 67th Annual Meeting of the American Society for Testing and Materials, Chicago. pp. 30–81.
Parisi, G., Procaccia, I., Rainone, C., Singh, M., 2017. Shear bands as manifestation of a criticality in yielding amorphous solids. Proc. Natl. Acad. Sci. 114, 5577–5582.
Paskin, A., Som, D.K., Dienes, G.J., 1981. Computer simulation of crack propagation: lattice trapping. J. Phys. C: Solid State Phys. 14, L171–L176.
Pereira Junior, M.L., Ribeiro Junior, L.A., Brandão, W.H., Aguiar, A.L., Galvão, D.S., De Sousa, J.M., 2020. Temperature effects on the fracture dynamics and elastic properties of popgraphene membranes. ChemPhysChem 21, 1918–1924.
Perriot, R., Gu, X., Lin, V.V., Oleynik, I.I., 2013. Screened environment-dependent reactive empirical bond-order potential for atomistic simulations of carbon materials. Phys. Rev. B 88, 064101.
Peyrard, M., 2004. Nonlinear dynamics and statistical physics of DNA. Nonlinearity 17, R1–R40.
Peyrard, M., Bishop, A.R., 1989. Statistical mechanics of a nonlinear model for DNA denaturation. Phys. Rev. Lett. 62, 2755–2758.
Ponson, L., Pindra, N., 2017. Crack propagation through disordered materials as a depinning transition: A critical test of the theory. Phys. Rev. E 95, 053004.
Prados, A., Carpio, A., Bonilla, L., 2013. Sawtooth patterns in force–extension curves of biomolecules: An equilibrium-statistical mechanics theory. Phys. Rev. E 88, 012704.
Puglisi, G., Truskinovsky, L., 2000. Mechanics of a discrete chain with bi-stable elements. J. Mech. Phys. Solids 48, 1–27.
Puglisi, G., Truskinovsky, L., 2013. Cohesion-decohesion asymmetry in geckos. Phys. Rev. E 87, 032714.
Pugno, N.M., Ruoff, R.S., 2004. Quantized fracture mechanics. Phil. Mag. 84, 2829–2845.
Rabbi, M.F., Chalivendra, V., 2021. Interfacial fracture characterization of multi-material additively manufactured polymer composites. Compos. Part C: Open Access 5, 100145.
Ramanaiah, S., Karde, V., Venkateswarlu, P., Ghoroi, C., 2015. Effect of temperature on the surface free energy and acid–base properties of gabapentin and pregabalin drugs- a comparative study. RSC Adv. 5, 48712–48719.
Ren, H., Zhuang, X., Anitescu, C., Rabczuk, T., 2019. An explicit phase field method for brittle dynamic fracture. Comput. Struct. 217, 45–56.
Rice, J.R., 1968. A path independent integral and the approximate analysis of strain concentration by notches and cracks. J. Appl. Mech. 35, 379–386.
Rountree, C.L., Kalia, R.K., Lidorikis, E., Nakano, A., Van Brutzel, L., Vashishta, P., 2002. Atomistic aspects of crack propagation in brittle materials: Multimillion atom molecular dynamics simulations. Annu. Rev. Mater. Res. 32, 377–400.
Ryvkin, M., Slepyan, L., 2010. Crack in a 2D beam lattice: analytical solutions for two bending modes. J. Mech. Phys. Solids 58, 902–917.
Sahimi, M., 2003a. Heterogeneous Materials I: Linear Transport and Optical Properties Volume 1. Springer, Heidelberg.
Sahimi, M., 2003b. Heterogeneous Materials II: Nonlinear and Breakdown Properties and Atomistic Modeling Volume 2. Springer, Heidelberg.
Santucci, S., Vanel, L., Guarino, A., Scorretti, R., Ciliberto, S., 2003. Thermal activation of rupture and slow crack growth in a model of homogeneous brittle materials. Europhys. Lett. 62, 320.
Schönecker, S., Li, X., Johansson, B., Kwon, S.K., Vitos, L., 2015. Thermal surface free energy and stress of iron. Sci. Rep. 5, 1–7.
Shih, C.F., 1981. Relationships between the J-integral and the crack opening displacement for stationary and extending cracks. J. Mech. Phys. Solids 29, 305–326.
Shih, C.F., Hutchinson, J.W., 1976. Fully plastic solutions and large scale yielding estimates for plane stress crack problems. J. Eng. Mater. Technol. 98, 289–295.
Shuminov, M., Givli, S., 2024. 2-d multistable structures under shear: equilibrium configurations, transition patterns, and boundary effects. J. Mech. Mater. Struct. 19, 265–302.
Sinclair, J.E., Lawn, B.R., 1972. An atomistic study of cracks in diamond-structure crystals. Proc. R. Soc. A 329, 83–103.
Slepyan, L.I., 1981. Dynamics of a crack in a lattice. Dokl. Akad. Nauk SSSR 258, 561–564.
Slootman, J., Waltz, V., Yeh, C.J., Baumann, C., Göstl, R., Comtet, J., Creton, C., 2020. Quantifying rate-and temperature-dependent molecular damage in elastomer fracture. Phys. Rev. X 10, 041045.
Slootman, J., Yeh, C.J., Millereau, P., Comtet, J., Creton, C., 2022. A molecular interpretation of the toughness of multiple network elastomers at high temperature. Proc. Natl. Acad. Sci. 119, e2116127119.
Stevens, R.N., Guiu, F., 1991. Energy balance concepts in the physics of fracture. Proc. R. Soc. Lond. Ser. A: Math. Phys. Sci. 435, 169–184.
Thomson, R., Hsieh, C., Rana, V., 1971. Lattice trapping of fracture cracks. J. Appl. Phys. 42, 3154–3160.
Tijssens, M., Van der Giessen, E., Sluys, L., 2000. Modeling of crazing using a cohesive surface methodology. Mech. Mater. 32, 19–35.

Truskinovsky, L., 1996. Fracture as a phase transition. In: Batra, R., Beatty, M. (Eds.), Contemporary Research in the Mechanics and Mathematics of Materials, Ericksen's Symposium. CIMNE, Barcelona, pp. 322–332.
Usmani, R., 1994. Inversion of Jacobi's tridiagonal matrix. Comput. Math. Appl. 27, 59–66.
Vincent-Dospital, T., Cochard, A., Santucci, S., Måløy, K.J., Toussaint, R., 2021. Thermally activated intermittent dynamics of creeping crack fronts along disordered interfaces. Sci. Rep. 11, 20418.
Vincent-Dospital, T., Toussaint, R., Cochard, A., Måløy, K.J., Flekkøy, E.G., 2020a. Thermal weakening of cracks and brittle-ductile transition of matter: A phase model. Phys. Rev. Mater. 4, 023604.
Vincent-Dospital, T., Toussaint, R., Santucci, S., Vanel, L., Bonamy, D., Hattali, L., Cochard, A., Flekkøy, E.G., Måløy, K.J., 2020b. How heat controls fracture: The thermodynamics of creeping and avalanching cracks. Soft Matter 16, 9590.
Wang, J., Niu, Y., Shao, H., Xu, J., Pham, V., Park, S., 2020. A comprehensive solution for modeling moisture induced delamination in electronic packaging during solder reflow. Microelectron. Reliab. 112, 113791.
Wang, M., Yan, C., Ma, L., Hu, N., Chen, M., 2012. Effect of defects on fracture strength of graphene sheets. Comput. Mater. Sci. 54, 236–239.
Wang, Z., Zu, X., Yang, L., Gao, F., Weber, W.J., 2007. Atomistic simulations of the size, orientation, and temperature dependence of tensile behavior in GaN nanowires. Phys. Rev. B 76, 045310.
Weiner, J.H., 1983. Statistical Mechanics of Elasticity. Dover Publications, New York.
Wells, A.A., 1961. Unstable crack propagation in metals: Cleavage and fast fracture. In: Proceedings of the Crack Propagation Symposium. College of Aeronautics, Cranfield, pp. 210–230.
Willis, J., 1967. A comparison of the fracture criteria of Griffith and Barenblatt. J. Mech. Phys. Solids 15, 151–162.
Winkler, R., 2010. Equivalence of statistical ensembles in stretching single flexible polymers. Soft Matter 6, 183–6191.
Wu, Z., Zhang, Y.W., Jhon, M.H., Gao, H., Srolovitz, D.J., 2012. Nanowire failure: Long=brittle and short=ductile. Nano Lett. 12, 910–914.
Yan, J., Clifton, K.B., Mecholsky, Jr., J.J., Gower, L.A., 2007. Effect of temperature on the fracture toughness of compact bone. J. Biomech. 40, 1641–1645.
Zapperi, S., Ray, P., Stanley, H.E., Vespignani, A., 1997. First-order transition in the breakdown of disordered media. Phys. Rev. Lett. 78, 1408.
Zhao, H., Aluru, N.R., 2010. Temperature and strain-rate dependent fracture strength of graphene. J. Appl. Phys. 108, 064321.